Magnetic field compatible hybrid circuit quantum electrodynamics

Kroll, James

DOI
10.4233/uuid:d72c0db9-8463-4098-a796-457aaa88eaa3

Publication date
2019

Document Version
Final published version

Important note
To cite this publication, please use the final published version (if applicable).
Please check the document version above.

Magnetic field compatible hybrid circuit quantum electrodynamics

Magnetic field compatible hybrid circuit quantum electrodynamics

Dissertation

for the purpose of obtaining the degree of doctor
at Delft University of Technology
by the authority of the Rector Magnificus Prof. dr. ir. T.H.J.J. van der Hagen,
Chair of the Board for Doctorates
to be defended publicly on Wednesday, 29th May 2019 at 10:00 am

by

James Grant Kroll

Master of Physics
The University of Edinburgh, Edinburgh, Scotland,
born in Reading, England.

This dissertation has been approved by the promoters:

Promotor: Prof. dr. ir. L. P. Kouwenhoven
Copromotor: Prof. dr. L. DiCarlo

Composition of the doctoral committee:

Rector Magnificus	chairperson
Prof. dr. ir. L. P. Kouwenhoven	Delft University of Technology
Prof. dr. L. DiCarlo	Delft University of Technology

Independent members:

Prof. dr. S. D. C. Wehner	Delft University of Technology
Prof. dr. C. W. J. Beenakker	University of Leiden
Prof. dr. Y. Ando	University of Cologne
Dr. A. Kou	Microsoft Quantum Lab Delft
Prof. dr. ir. L. M. K. Vandersypen	Delft University of Technology, reserve

"Whatever you can do, or dream you can, begin it.
Boldness has genius, power, and magic in it."
W. H. Murray

Contents

Summary

Majorana bound states (MBSs) are novel particles predicted to be created when superconductor/semiconductor hybrid structures with strong spin-orbit coupling are subjected to strong magnetic fields. Expected to exhibit non-Abelian exchange statistics, they could form the basis of a new kind of quantum computer that is inherently protected from environmental noise, a common problem that has frustrated other quantum computing platforms. The current techniques used to measure these particles are highly sensitive, having provided the best evidence yet for their existence, but they are intrinsically too slow to form the basis of a useful quantum computer.

To remedy this, this thesis integrates exotic materials into high frequency superconducting circuits that have been engineered to be resilient to strong magnetic fields, creating hybrid devices that potentially allow for fast and precise measurement and control of MBSs and their properties.

Several proposals to demonstrate the novel exchange statistics of MBSs use a specific type of superconducting qubit, the 'transmon', for fast readout of the state of the MBSs. Problematically, the strong magnetic fields required to induce MBSs would destroy the superconductivity traditional transmons rely on, preventing them from operating as intended. To resolve this, the key constituent components of the transmon, the superconducting resonator and the Josephson junction have been engineered separately to become resilient to strong magnetic fields.

Chapter 4 explores how nanofabrication techniques and careful consideration of the properties of thin superconducting films can be used to engineer superconducting co-planar waveguide resonators that remain operational in strong parallel magnetic fields of 6 T and perpendicular magnetic fields of 20 mT, an order of magnitude greater than previously reported. Building on the results of Chapter 4, Chapter 5 utilises a graphene based Josephson junction, where the monoatomic thickness of the graphene provides an inherent protection against parallel magnetic fields, allowing us to demonstrate operation of a transmon circuit at a parallel magnetic field of 1 T.

Advances in nanowire material growth intended to improve the signatures of MBS are used in Chapter 6 to create a low power, highly coherent on-chip microwave source. With broad potential applications in superconducting circuits, it demonstrates a platform well suited for the detection of unique radiation that MBSs are predicted to emit. The thesis is concluded by Chapter 7, which describes the engineering and development of a nanowire based transmon qubit capable of measuring key properties of MBSs in the qubit's energy spectrum.

Samenvatting

Majorana toestanden zijn deeltjes die gerealiseerd kunnen worden in hybride supergeleidende/halfgeleidende systemen met sterke spin-baan koppeling wanneer deze worden onderworpen aan een sterk magnetisch veld. Dankzij hun niet-Abelse verwisselingsstatistiek kunnen deze toestanden de basis vormen voor een nieuw soort kwantumcomputer die ongevoelig is voor ruis uit de omgeving, een belangrijk probleem voor andere kwantumcomputer platforms. De huidige technieken om deze deeltjes te meten hebben het tot dus ver beste bewijs geleverd voor hun bestaan, maar hoewel ze zeer gevoelig zijn zijn ze te langzaam om de basis te vormen voor een kwantumcomputer.

Om dit probleem op te lossen, integreert dit proefschrift exotische materialen en hoog frequente supergeleidende schakelingen, die ontworpen zijn om robuust te zijn in sterke magnetische velden, om zo hybride schakelingen te realiseren die het mogelijk maken snel en precies de Majorana deeltjes en hun eigenschappen te meten en aan te sturen.

Verscheidene voorstellen om de uitwisselingsstatistiek van de Majorana deeltjes aan te tonen gebruiken een bepaald type supergeleidende qubit, de 'transmon', om de toestand van de Majoranas snel uit te kunnen lezen. De sterke magnetische velden die noodzakelijk zijn om de Majorana toestanden te realiseren vernietigen normaal gesproken de supergeleidende eigenschappen van traditionele transmons, worden deze niet gebruikt kunnen worden. Dit probleem is opgelost door de bouwstenen van de transmon, de supergeleidende resonator en de Josephson junctie (JJ), beide aan te passen om ongevoelig te worden voor sterke magnetische velden.

Hoofdstuk 4 onderzoekt hoe nanofabricage technieken en een zorgvuldige beschouwing van de eigenschappen van supergeleidende dunne films gebruikt kunnen worden om een supergeleidende coplanaire golfgeleiders te maken die operationeel blijven in magnetische velden tot 6 T in het vlak en 20 mT uit het vlak, een ordegrootte hoger dan voorheen gepubliceerd. Voortbouwend op de resultaten van hoofdstuk 4 gebruikt hoofdstuk 5 een JJ van grafeen, waar de enkele atoomlaag dikte een intrinsieke bescherming biedt in magneetvelden in het vlak, wat het mogelijkt maakt om een transmon schakeling aan te sturen in een magnetisch veld van 1 T in het vlak.

Vooruitgang in de groei van nanodraad materialen gericht op het verbeteren van de eigenschappen van Majorana toestanden wordt in hoofdstuk 6 gebruikt om een laagvermogen, hoog coherente on-chip microgolfbron te maken. Hiermee wordt een geschikt platform gedemonstreerd om de unieke straling die Majorana deeltjes uitzenden te detecteren, dat daarnaast vele mogelijke applicaties heeft in supergeleidende schakelingen. Het proefschrift besluit met hoofdstuk 7, waar de ontwikkeling van een transmon qubit op basis van een nanodraad wordt beschre-

ven die het mogelijk maakt om belangrijke eigenschappen van Majorana deeltjes
te meten in het spectrum van de qubit.

1

Introduction

1.1. The first quantum revolution

At the beginning of the twentieth century, a confluence of the greatest minds in the history of physics came together to offer us the first quantum revolution: a transformation in our understanding of the universe from one that made sense to our evolved animalistic intuitions to one that stretched our abilities of comprehension. Drawing on unexplained results in several seemingly unconnected branches of physics, their imagination led them to propose a radical idea: that light, despite all its wave-like properties consisted of individual packets or 'quanta' of energy. From this seed grew a complete theory of the electronic structure of atoms; each atom individually inaccessible but when considered as an ensemble successfully describing the anomalous results previously observed in experiments. Initially only applicable to gases - sparse collections of individual atoms - others came to extend this description of reality into a theory able to reproduce the electronic and thermal behaviour of solids. Thus the first quantum revolution gave us its second great gift: solid state physics - the physical theory upon which the electronics of today's information age is based. Information processing technology progressed rapidly from this point, with initial attempts using individual elements the size of a finger (Fig. 1.1a) to produce analog computers the size of rooms. Progress demanded not only a solid understanding of solid state physics, but great advancements in materials synthesis, fabrication and measurement. As society's demand for information processing grew ever greater, it drove a concurrent continual evolution of the fabrication, chemical and materials techniques underlying the production of the electronics; ever faster, ever smaller, ever cheaper, culminating in the modern computer processors of today: 100 million transistors on a chip, 10s of nanometers wide, pulsing at nanosecond timescales without errors for great lengths of time (Fig. 1.1b).

1.2. The second quantum revolution

As well as bringing huge benefits to society, the development of computer technology brought surprising advantages to the field of physics that originated it: quantum mechanics. As the need for faster electronics continually reduced the
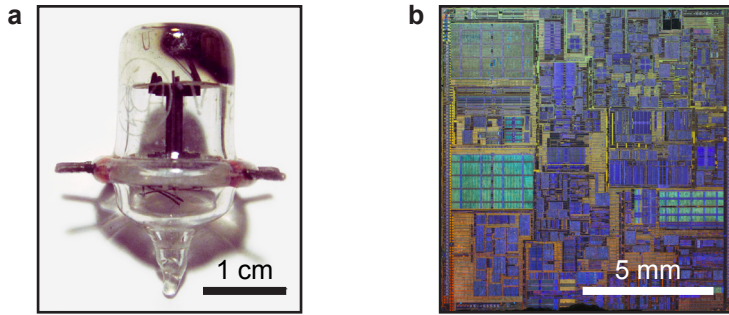
Figure 1.1: **a** RCA 955 'acorn tube'. Available from 1935, these vacuum tube amplifiers are the analog precursor to the digital transistors we rely on today. **b** Optical microscope image of the die of an Intel Pentium 4 Northwood (2002) central processing unit. Although outdated at the time of writing, as a feat of modern engineering it is no less impressive with 55 million transistors in $\sim 1\,cm^2$ fabricated using a 130 nm feature size process.

size, cost and volatility associated with producing microelectronics, scientists used this enhanced computing power to run computer simulations of their physical systems, deepening their understanding. Simultaneously, the field of cavity quantum electrodynamics[1] developed optical techniques to reliably manipulate the states of individual atoms suspended in cavities with a scale and reliability that would have been considered impossible by the originators of quantum mechanics. These experiments explored the limits of quantum mechanics at the interface of two worlds, our 'classical' world and the quantum mechanical world, providing deep insights into the nature of reality and the problem of decoherence: how quantum mechanical systems 'lose' their information and transform into classical objects.

Feynman, ever prescient, predicted in his 1959 lecture 'There's Plenty of Room at the Bottom' that we would one day attain control of individual atoms and electrons, opening up the possibility of atomic scale chemistry, electronics and machines [1]. Following on from this, decades later in 1982 he proposed a new tool with which to analyse the world, a quantum mechanical machine that would allow us to better simulate an inherently quantum mechanical world, the 'quantum computer' [2]. Such a machine would utilise the unintuitive and strange features of quantum mechanics to perform certain calculations faster than any computer built on classics mechanics ever could.

Only three years later experimental labs round the world begun to show that control of individual quantum states in solid state systems was possible [3], although it took more than a decade to demonstrate complete control of a quantum mechanical state in a solid state system [4]. So began the second quantum revolution, where developments in nanotechnology gifted us the ability to control the quantum mechanical nature of atoms and electrons at will [5].

---

[1]*Cavity* quantum electrodynamics is the progenitor of *circuit* quantum electrodynamics. In circuit quantum electrodynamics, the techniques originally used for controlling the quantum states of individual atoms in cavity quantum electrodynamics are applied to superconducting circuits that behave analogously to atoms in a cavity.
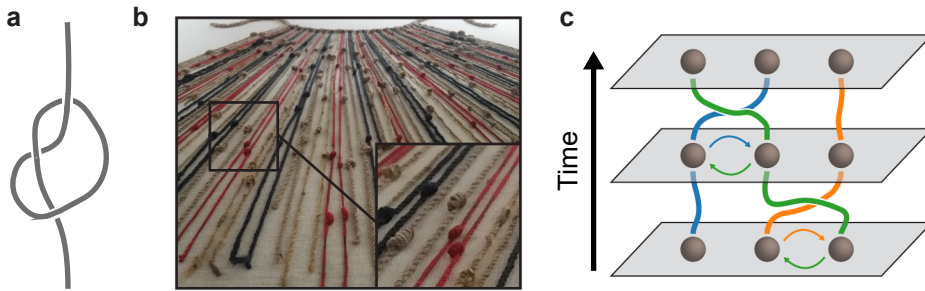
Figure 1.2: **a** A knot tied in a string represents a piece of information that has been stored in the topology or 'shape' of the system. Short of cutting the piece of string, no amount of moving, twisting or stretching the string can destroy the knot. **b** A thousand years ago, the Aztecs used knots tied in a piece of string as an information storage device. 'Quipu in the Machu Picchu museum, Casa Concha, Cusco' by Pi3.124 licensed under CC BY-SA 4.0. **c** Quasiparticles called non-Abelian anyons that are confined to two dimensions exhibit a novel kind of exchange statistics that allows them to remember the order and direction in which they exchanged. This allows information to be stored and processed by braiding their 'worldlines' together, potentially forming the basis of a topological quantum computer.

1.3. The promise of topology

These early pioneers, driven by proposals from theorists about the feats that a quantum computer could achieve drove development of their chosen quantum mechanical systems until accurate preparation and manipulations of a single quantum mechanical state ('qubit') were routine. One qubit in isolation is not very useful though. The power of qubits comes from gathering together and interconnecting many of them, where the richness provided by their collective states can be effectively utilised by the quantum computer. Attempting to do this, they encountered the same problem that has been afflicting quantum computing since its inception: decoherence - the process by which the information stored in qubits leaks into the environment.

Although years of research have successfully reduced the rate of decoherence in these systems by many orders of magnitude [6], they still face fundamentally the same problem: quantum information stored in a local system such as a magnetic spin or a circulating loop of current will always be susceptible to perturbations from the environment. A single photon at the wrong place and the wrong time can corrupt the quantum information, potentially ruining the result of a long computation. Topological quantum computing proposes a radically different paradigm for information storage, where the information is stored not in individual atoms or spins but as a distributed property of a larger quantum system. To understand topology, and how it can be used to stored information in a manner protected from the environment, consider the case of a knot tied in a piece of string (Fig. 1.2a). You can bend and stretch and twist the string, but the knot will always remain. Destroying the information requires a drastic action, such as cutting or snapping the string. This is not a new idea - in fact, ancient cultures in Hawaii, China and South America used knots in string to record information thousands of years ago, using
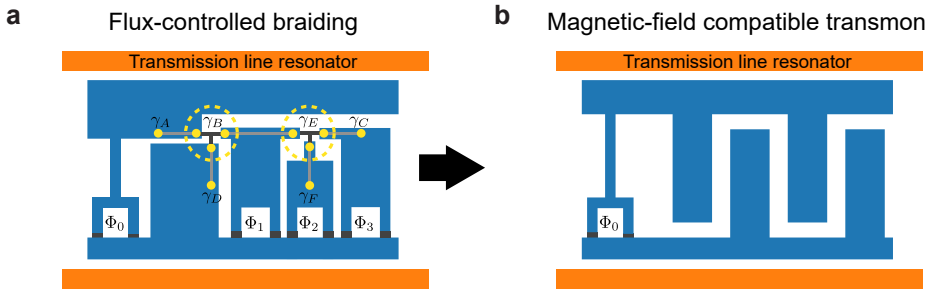
Figure 1.3: **a** Schematic for one of the simplest circuits capable of demonstrating braiding. It consists of multiple superconducting islands separated by superconducting weak links and semiconducting regions capable of hosting MBSs. Pulsing magnetic fluxes through the loops (denoted by Φ_n) effectively exchanges MBSs γ_B and γ_E. Measurement of the resulting state is performed by reading out the charge on the large top island using techniques from the superconducting qubit community. **b** Removing the sections that are responsible for demonstrating braiding leaves the section of the circuit that is responsible for measurement. It is based on a type of superconducting qubit called the transmon, and although the type of measurement required has been demonstrated previously [11] the strong magnetic fields required to create MBSs would have rendered the devices of the time inoperable. Figure adapted from [12].

topology to store information robustly in a manner that ink on a piece of paper is not (Fig. 1.2b).

Topological quantum computing uses a similar technique, except instead of using knots in physical space it utilises knots in time. By creating a special class of quasiparticle called a 'non-Abelian anyon' that is confined to two dimensions, the quasiparticles acquire a novel kind of exchange statistics where in contrast to 'normal' particles they remember the order in which they are exchanged [7]. This can be used to 'braid' the histories of these particles together, creating and manipulating quantum information in a way that is protected from the environment (Fig. 1.2c).

Attempts to realise these particles in an experimental setting proved unsuccessful until a set of theoretical proposals detailed how a specific combination of superconductors, exotic semiconductors and strong magnetic fields could be used to create the simplest of these particles, the Majorana bound state (MBS) [8, 9]. Experimental results soon followed providing strong evidence that these states had been successfully created [10], with the task of experimental groups immediately turning to creating a platform that could use MBS for quantum information processing.

Fig. 1.3a shows a diagram of the first proposed circuit capable of braiding to attract serious experimental attention [12]. It consists of a series of superconducting islands, bridged by semiconducting nanowires that when exposed to a sufficiently strong magnetic field would host MBSs (denoted by γ). By preparing the system in a well-defined state, then pulsing magnetic flux (Φ_{1-3}) through the three loops at the bottom-right in a pre-defined sequence the MBSs would be exchanged in a manner that would braid the two inner MBSs (γ_B, γ_E). To verify that braiding

had occurred, topological protection would then be broken by threading a magnetic flux through Φ_0 and using techniques previously developed for transmons (a specific type of superconducting qubit) to measure the charge on the top superconducting island and thus the result of the braiding operation (Fig. 1.3a) [11].

Although such measurements had been previously demonstrated, the device used to perform them would have become inoperable when subjected to the strong magnetic fields required to produce MBSs. This thesis details the engineering and development of a superconducting qubit capable of surviving these strong magnetic fields. To do so required the development of new fabrication and engineering techniques, and the investigation of novel materials that can be combined to create hybrid superconducting circuits with desirable properties of relevance for the wider quantum computing community in general.

Chapter 2 details the theoretical concepts necessary to design and understand the devices fabricated in this thesis. **Chapter 3** describes the fabrication and measurement techniques necessary to perform experiments with said devices. **Chapter 4** explores how by considering the properties of thin superconducting films we can engineer superconducting devices to become resilient to very strong parallel magnetic fields. **Chapter 5** describes the first integration of graphene Josephson junctions into a microwave frequency superconducting circuit to create a graphene transmon. The aforementioned techniques and novel material properties of graphene are used to demonstrate device operation at magnetic fields strong enough to induce MBSs. **Chapter 6** combines semiconducting nanowires with high quality factor superconducting resonators to demonstrate a device capable of generating highly coherent microwave pulses on-chip, with broad potential applications in the field of quantum computing. **Chapter 7** combines techniques and results from previous chapters to describe the development and measurement of a semiconducting nanowire based transmon qubit able to operate in extremely high parallel magnetic fields. Instead of using the transmon merely as a detector for a larger braiding circuit, this chapter considers the possibility of inducing a topological state in the transmon itself and explores the effects this would have on the measurable parameters of the device. **Chapter 8** concludes the thesis, and suggests possible fruitful avenues of future research.

1

References

[1] Feynman, R. P. There's Plenty of Room at the Bottom. *Engineering and Science* **23**, 22–36 (1960).

[2] Feynman, R. Simulating Physics with Quantum Computers. *International Journal of Theoretical Physics* **21**, 467–488 (1982).

[3] Martinis, J. M., Devoret, M. H. & Clarke, J. Energy-level quantization in the zero-voltage state of a current-biased Josephson junction. *Physical Review Letters* **55**, 1543–1546 (1985).

[4] Nakamura, Y., Pashkin, Y. A. & Tsai, J. S. Coherent control of macroscopic quantum states in a single-Cooper-pair box. *Nature* **398**, 786–788 (1999).

[5] Dowling, J. P. & Milburn, G. J. Quantum technology: The second quantum revolution (2003).

[6] Devoret, M. H. & Schoelkopf, R. J. Superconducting circuits for quantum information: an outlook. (2013).

[7] Kitaev, A. Fault-tolerant quantum computation by anyons. *Annals of Physics* **303**, 2–30 (2003).

[8] Lutchyn, R. M., Sau, J. D. & Das Sarma, S. Majorana fermions and a topological phase transition in semiconductor-superconductor heterostructures. *Physical Review Letters* **105**, 077001 (2010).

[9] Oreg, Y., Refael, G. & Von Oppen, F. Helical liquids and Majorana bound states in quantum wires. *Physical Review Letters* **105**, 177002 (2010).

[10] Mourik, V. *et al.* Signatures of majorana fermions in hybrid superconductor-semiconductor nanowire devices. *Science* **336**, 1003–1007 (2012).

[11] Ristè, D. *et al.* Millisecond charge-parity fluctuations and induced decoherence in a superconducting transmon qubit. *Nature Communications* **4**, 1913 (2013).

[12] Hyart, T. *et al.* Flux-controlled quantum computation with Majorana fermions. *Physical Review B* **88**, 1–17 (2013).

2

Device design and theoretical concepts

This chapter serves to introduce the theoretical concepts necessary to correctly design and model the devices fabricated and measured in this thesis. Initially the physics of superconductivity and superconducting resonators will be introduced, with a particular focus on how to use this knowledge when designing them so that they consistently exhibit the experimental properties required. Secondly, as Josephson junctions are key components for most chapters of this thesis an overview of their physics will be provided. Their use in superconducting qubits to create 'artificial atoms' will then be discussed, closely followed by the processes by which their state is prepared and read out using circuit quantum electrodynamics. In the final section, novel qubit behaviours that result from interesting mesoscopic and topological effects in our Josephson junctions will be discussed.

2.1. Superconductivity

Superconductivity is the property by which some materials, when cooled below their superconducting transition temperature T_C enter a state of zero resistance, allowing current to flow almost indefinitely [1]. The microscopic origin of this is a rich and complex field of physics, almost all of which can be ignored when attempting to understand the principles of modern superconducting quantum circuits. As such, I will focus only on the minimal phenomenology required to understand the work in this thesis.

In the simplest model of electronic conduction in metals, electrons behave like waves, using the crystal lattice as a medium [2]. As fermions, the Pauli exclusion principle prevents them from occupying the same state, causing them to fill up available states one by one up until the Fermi energy E_F. In bulk crystals the large number of electronic states causes their energies to overlap in large regions, resulting in the band structure of solids. The key characteristic about metals is that E_F sits within one of these bands, making it easy for applied fields to create energy gradients that result in a net flow of electrons near E_F: a current (Fig. 2.1a). In normal metals, this current flow is impeded by the electrons scattering from defects or
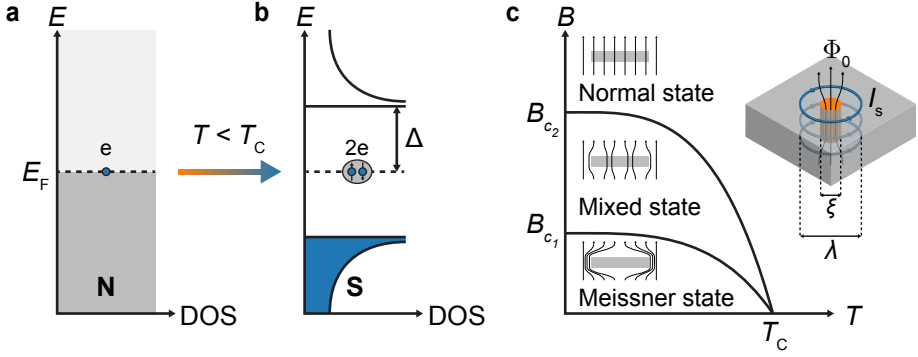
Figure 2.1: Superconductor phenomenology **a** In normal metals, the fermionic nature of electrons results in continuous bands of electronic states that are populated up to E_F. **b** Below T_C an attractive potential mediated by virtual phonon exchange causes electrons of opposite spin to pair up, creating the superconducting Cooper pair condensate with an excitation gap of 2Δ. **c** Phase diagram for a type-II superconductor, with a Meissner state that repels all applied magnetic field up to B_{c_1}, a mixed state that allows some magnetic field to penetrate in the form of Abrikosov vortices up to B_{c_2} and a normal state where the applied magnetic field is enough to kill the superconductivity. Inset is a diagram of an Abrikosov vortex, a normal core surrounded by a circulating supercurrent with an outer extent of λ_s and inner extent of ξ.

vibrations in the lattice, resulting in energy loss and a finite resistance of the metal [3].

In contrast to this, under the right conditions some materials allow fermions of opposite spins to exchange virtual phonons (lattice excitations) creating an attractive potential between then. This causes them to pair up into a particle with bosonic statistics called a 'Cooper pair'. As the Pauli exclusion principle applies only to fermions, the bosons are no longer prohibited from occupying the same state and promptly condense into a many particle condensate wave function $\psi(r)$ with an excitation gap of 2Δ, which maintains phase coherence over macroscopic distances (Fig. 2.1b).

In addition to T_C, two additional parameters that characterise important length scales are used to classify superconductors. The first is the penetration depth λ_s which defines how far into a superconducting material magnetic flux can penetrate before it is repelled by the Meissner effect. The exact form of λ_s depends upon which theory is used to model the superconductor, but in the simplest case of the London equations it takes an upper limit of the form [4]:

$$\lambda_s = \sqrt{\frac{mc^2}{4\pi n e^2}} \tag{2.1}$$

where m is the mass of the charge carrier, c is the speed of light, n is the number density of the charge carriers and e is the electron charge. The second important length scale is the coherence length ξ_0 which defines the spatial extent of the superconducting wave function. Bardeen-Cooper-Schrieffer (BCS) theory is the simplest microscopic theory describing the origin of superconductivity, and it

gives the functional form of ξ_0 to be [4]:

$$\xi_0 = \frac{\hbar v_F}{\pi \Delta} \tag{2.2}$$

with $\hbar$ being the reduced Planck constant and v_F being the Fermi velocity.

The ratio between these two parameters is the Ginzberg-Landau parameter $\kappa_{GL} = \lambda_s/\xi$ and has important implications for the behaviour of the superconductor when it is subjected to magnetic fields. Superconductors such as Al or Pb with $0 < \kappa_{GL} < \frac{1}{\sqrt{2}}$ are type I superconductors that expel applied magnetic flux with the Meissner effect until the critical field B_c is reached, after which the magnetic flux penetrates the material destroying superconductivity [4].

Conversely, when $\kappa_{GL} > \frac{1}{\sqrt{2}}$ the free energy at the superconductor-metal boundary becomes negative, making it energetically favourable to minimise the interface area. In this case the Meissner effect expels the applied magnetic field until B_{c_1}, where it becomes energetically favourable for the magnetic flux to penetrate the superconductor to create regions of normal metal of radius $\sim \xi$ surrounded by supercurrent with an outer extent of $\sim \lambda_s$. Above B_{c_2}, the magnetic field is sufficient to destroy superconductivity entirely (see Fig. 2.1c for the state diagram of a type II superconductor, inset is a diagram of an Abrikosov vortex with important length scales noted.) [4].

As $\psi(r)$ is coherent over macroscopic distances and must be single valued everywhere, the phase difference $\Delta\phi = n2\pi$ that the supercurrent acquires as it circulates the magnetic flux must be an integer of 2π, giving $\Delta\phi = n2\pi$. This has the important effect of quantising the total magnetic flux Φ of the vortex to be integers of the magnetic flux quantum $\Phi = n\Phi_0$ [3, 4].

2.2. Superconducting resonators

2.2.1. Background

Superconducting (SC) coplanar waveguide (CPW) resonators serve as the base platform for every device described in this thesis. Great care must be taken during their design and fabrication to ensure that they operate as expected and attain the high quality factors required for the experiments. SC CPW resonators, key components of SC quantum computing (QC) platforms are now also recognised as important for other QC platforms and superconducting circuits. As they are fabricated from superconductors, their low loss allows them to attain internal quality factors exceeding 10^6, meaning that a photon can resonate $\sim 10^6$ times before being lost. This makes them ideal for transmitting and storing photons over long distances and for long timescales respectively, with photons travelling $\sim$100 km or being stored for $\sim$1 ms before dissipating [5, 6].

Their planar nature allows for easy fabrication using traditional lithography techniques from a single metallic layer. Due to their large size and distributed nature they are highly controllable, with their major characteristics such as impedance, resonant frequency and coupling to the outside world principally being set by their geometry. This tight control of the local electromagnetic environment means that

2
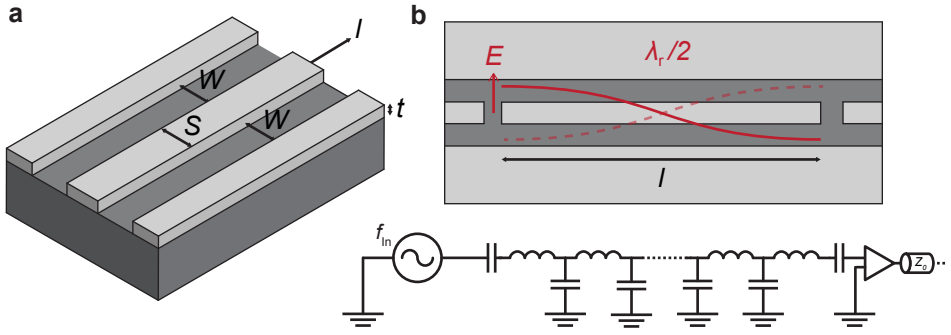
Figure 2.2: CPW geometry **a** Schematic of the key lengthscales to consider in the design of a CPW. **b** Two capacitors at either end of a CPW strip of length l create impedance mismatches that form a $\lambda_r/2$ resonator. This distributed element can be approximated as an infinite series of lumped element LC resonators.

when combined with high quality factors, the resonator also serves as a narrow bandpass filter to protect devices that are embedded within them from the outside electromagnetic environment, resulting in extended coherence times for superconducting qubits. Their planar nature has the additional benefit of greatly reducing the mode volume of the electric field, creating large electric field gradients at the anti-nodes of the resonator increasing the energy density by a factor of 1,000,000 and the dipole coupling by 1,000 when compared to 3D microwave cavities [7].

When designed to operate between 4-12 GHz, they sit at an optimal energy scale: high enough in energy to sit in the ground state at thermal equilibrium ($hf_r \gg k_bT$) with easily accessible dilution refrigerator temperatures ($T \simeq 20$ mK) yet low enough in energy to operate in the C and X radio-frequency bands used by the telecommunication and satellite industries. This enables experiments to leverage the significant capital invested to develop high performance and low cost equipment that operates in this frequency range, such as high electron mobility amplifiers, low loss circulators and fast, sensitive measurement electronics [8].

2.2.2. Coplanar waveguide resonators

CPWs are a form of planar transmission line that are suitable for transmitting signals in the radio frequency and microwave regime. The fundamental properties of CPWs are described extensively in the literature [9–11], and so we summarize only their main characteristics here. A coplanar waveguide propagates the (quasi) transverse electromagnetic (TEM) mode where the electric and magnetic fields lie in the plane perpendicular to the direction of propagation. The currents flow at the edges of the central line and ground planes. The central line current is equal and antiparallel to the current in the ground plane, and the return current in both sides of the groundplane is in phase (even mode). They are formed from a planar sheet of metal with thickness t deposited on a substrate with a dielectric constant of ϵ_s (see Fig. 2.2a). The gap between the ground plane W and the central conductor

of width S set the geometric inductance L and capacitance C of the distributed device:

$$L_g = \frac{\mu_0 K(k')}{4K(k)} \tag{2.3}$$

$$C = 4\epsilon_0\epsilon_{\text{eff}}\frac{K(k)}{K(k')} \tag{2.4}$$

where μ_0 and ϵ_0 are the permeability and permittivity of free space respectively, $\epsilon_{\text{eff}} \simeq (1 + \epsilon_s)/2$ is the effective dielectric constant experienced by the CPW, K is the complete elliptic integral of the first kind, $k = S/(S + 2W)$ and $k^2 + k'^2 = 1$.

Kinetic inductance

In thin superconducting films that result in a sufficiently low electron density, an additional series contribution to the inductance called the kinetic inductance L_k becomes important. The kinetic inductance is set by $L_k = L_s g$ [10], with $g = g_c + g_g$ being a geometric factor defined by:

$$g_c = \frac{1}{4S(1 - k^2)K^2(k)}\left[\pi + \ln\left(\frac{4\pi S}{t}\right) - k\ln\left(\frac{1+k}{1-k}\right)\right] \tag{2.5}$$

$$g_g = \frac{k}{4S(1 - k^2)K^2(k)}\left[\pi + \ln\left(\frac{4\pi(S+2W)}{t}\right) - \frac{1}{k}\ln\left(\frac{1+k}{1-k}\right)\right] \tag{2.6}$$

for values of $t < 0.05S$ and $k < 0.8$.

This analysis must be modified when t becomes less than half the penetration depth of the superconductor $t < \lambda_s/2$ however. In this case, the length scale over which the self-field of the current flow penetrates the conductors is no longer set by λ_s but instead by the Pearl length $\Lambda = 2\lambda_s^2/d$. This results in corrections to both the geometric and kinetic inductance of the CPW. For geometries that approach the limit of $W \to 0$ Clem provides exact solutions for the corrected inductances [12]. Approximate solutions are also provided for the case of finite W, with L_g easily corrected by replacing k with an effective parameter:

$$k_{\text{eff}} = k\frac{1}{1 + \frac{2c\Lambda}{S}} \tag{2.7}$$

where c is a slowly varying function of $2\Lambda/S$ of order unity. The modification of L_k is more complicated however, taking the form:

$$L_k = \frac{\mu_0\Delta}{2S}g_{\text{kp}} \tag{2.8}$$

where

$$g_{\text{kp}} = \frac{(k + p^2)\operatorname{arctanh}(p) - (1 + kp^2)\operatorname{arctanh}(kp)}{p(1 - k^2)[\operatorname{arctanh}(p)]^2} \tag{2.9}$$

and where p is a numerically calculated parameter well approximated as:

$$p \approx \begin{cases} 0.63/\sqrt{2\Lambda/S} & \text{if } 2\Lambda/S \gg 1 \\ 1 - 0.67(2\Lambda/S) & \text{if } 2\Lambda/S \ll 1 \end{cases} \tag{2.10}$$

Impedance and frequency targeting

The impedance $Z = \sqrt{L/C}$ of CPWs are typically chosen to match a characteristic impedance of $Z_0 = 50\,\Omega$ such that the device can interface correctly with commercially available hardware, with minimal reflections or signal distortions. To form a resonator, impedance mismatches are defined at the ends of a CPW strip of length l. An open end (as seen in Fig. 2.2b) defines an electric anti-node, creating a resonator with a fundamental mode of wavelength $\lambda_r/2$, and a resonant frequency of:

$$\omega = \frac{2\pi}{2l\sqrt{(L_g + L_k)C}} \tag{2.11}$$

Alternatively, an end can be terminated by a metallic short to ground, defining an electric node and instead creating a $\lambda_r/4$ resonator with half the above frequency (as used in Chap. 4,5).

As the contribution to the total inductance L from L_k can be significant in our experiments, it should be accurately estimated in order to ensure that the resonators operate in the frequency range available to our experimental hardware (4-8 GHz). This can be done through analytical analysis using the above formula. In cases where the above formula does not apply, simulations or experimental measurements of the inductive contribution in identical geometries can allow for appropriate estimation and frequency targeting.

2.2.3. Loss mechanisms

As resonators are common tools with which to monitor, control, protect or amplify other scientific systems of interest, properties other than their resonant frequency are important to understand and control if they are to be used effectively. Within the context of this thesis, the second most important property to consider is the resonator quality factor Q. The quality factor describes the photon lifetime in the resonator, and can be understood as the energy lost per unit cycle:

$$Q = \frac{\omega E}{P} \tag{2.12}$$

Q is non-descript in that it does not consider the causes of energy loss in the system. When attempting to optimise the coupled system it makes sense to separate the loss channels, so that each may be better understood. In the simplest case of a resonator connected to a readout circuit, the resonator is described as 'loaded' by the impedance of the readout and the quality factor becomes:

$$\frac{1}{Q_l} = \frac{1}{Q_c} + \frac{1}{Q_i} \tag{2.13}$$

where Q_i is the intrinsic quality factor describing internal losses in the resonator and Q_c is the coupling quality factor which accounts for photons that leak from the resonator to the coupled circuit. In general, intrinsic losses should be minimised

as much as possible as they can limit relaxation times via the Purcell effect in transmon qubits (Chap. 5,7) or reduce the coherence in microwave frequency lasers (Chap. 6). Several common contributions to the intrinsic losses in $\lambda_r/4$ resonators are as follows [5, 13]:

$$Q_{\text{Res}} = \frac{n\pi Z}{2R_{l,n}l} \tag{2.14}$$

$$Q_{\text{Diel}} = \frac{\omega_r C}{G} = \frac{1}{\tan\delta} \tag{2.15}$$

$$Q_{\text{Rad}} = \frac{\pi(1+\epsilon_s)^2}{2\epsilon_s^{5/2}} \frac{\eta_0}{Z} \frac{1}{I'(\epsilon_s, n)} \frac{1}{n-\frac{1}{2}} \left(\frac{L}{S}\right)^2 \tag{2.16}$$

Q_{Res} are losses due to sheet metal resistance (low but not necessarily negligible, even in superconductors) where $R_{l,n}$ is the resistance per unit length of the CPW. Q_{Diel} are losses at the dielectric interface where δ is the dielectric loss tangent. Q_{Rad} describes radiative loss of the cavity photons into the vacuum where $\eta_0 = 377\,\Omega$ is the impedance of free space, n is the mode number and $I'(\epsilon_s, n)$ must be numerically calculated as in [13].

Depending on the exact system and use case, a multitude of loss mechanisms such as two level systems [14, 15] or superconducting vortices [16] (see also Chap. 4) are possible, with the Q formalism serving well to understand their behaviour and subsequently mitigate their effects.

2.2.4. Coupling

The ratio of Q_i to Q_c is defined by Pozar to be the coupling ratio $g_Q = Q_i/Q_c$ with 3 separate regimes [11]:

$$g_Q < 1, \text{Undercoupled} \tag{2.17}$$

$$g_Q = 1, \text{Critically coupled} \tag{2.18}$$

$$g_Q > 1, \text{Overcoupled} \tag{2.19}$$

The low Q_i of our resonators mean that they typically operate in the 'overcoupled' where the lifetime of a photon in the cavity and thus the measured linewidth of the resonance is set principally by Q_c. Again, the optimal value for Q_c depends on the application - when considering qubit readout, the ideal Q_c is a multivariate optimisation problem depending not only on the resonator linewidth κ but also the qubit frequency, the qubit-resonator coupling rate and qubit relaxation times, a full discussion of which is left to other texts [5]. When studying loss mechanisms in the resonators themselves however (as in Chap. 4) accurate extraction of Q_i intrinsic losses can only occur when $g_Q < 10$ [15], necessitating precise and reliable control of Q_c.

For $\lambda_r/4$ resonators capacitively coupled to a feedline (Fig. 2.3a), the system can be modelled using S parameters that describe the how signal input at one port will propagate through the system and exit from the other ports. In the simplest two
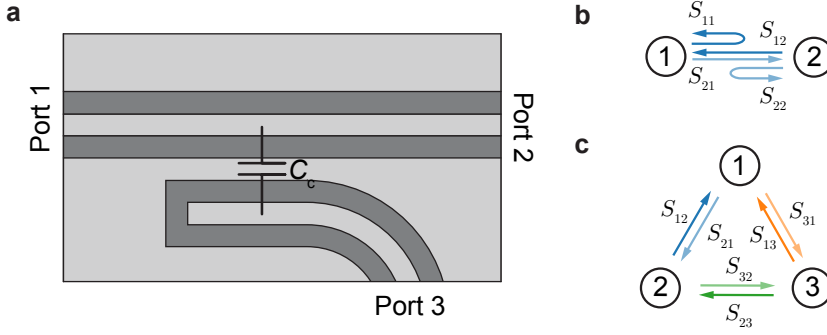
Figure 2.3: Coupling capacitors and S parameters **a** Schematic showing how a $\lambda_r/4$ resonator capacitively coupled to a feedline can be modelled as a system with 3 ports. **b** In the simplest case with 2 ports, S parameters describe the scattering probabilities for transmission (S_{21}, S_{12}) and reflection (S_{11}, S_{22}) at each port. **c** In the 3 port case, to calculate capacitive coupling between the feedline and the resonator we are interested in S_{31}.

port case (Fig. 2.3b) S_{21} describes the probability that signal input at port 1 will be emitted at port 2. This be extended to consider the reverse case, and indeed even the case where signal input at port 1 is reflected (S_{11}).

Using analytical models or computer simulations, C can be estimated or S_{31} extracted directly, allowing Q_c to be esimated [13]:

$$Q_c = \frac{n\pi}{2|S_{31}|} = \frac{n\pi}{2Z_0 Z(\omega_r C_C)^2} \tag{2.20}$$

where n is the mode number, Z is the resonator impedance and the feedline impedance is assumed to be Z_0.

Photon number estimation
Once Q_i and Q_c have been measured, the photon number in the cavity $\langle n_{ph} \rangle$ for a given input power P_{in} can be estimated using the following relation [15]:

$$\langle n_{ph} \rangle = \frac{2}{\hbar \omega_r^2} \frac{Q_l^2}{Q_c} P_{in} \tag{2.21}$$

note that this formula provides an upper limit on $\langle n_{ph} \rangle$ as it assumes a perfectly impedance matched transmission line with no reflections.

2.3. Josephson junctions
Josephson junctions (JJs) are superconducting devices consisting of two superconductors separated by a weak link. The unique properties of the Josephson effect (JE) that describes their operation makes them technologically important in superconducting circuits [4], quantum computing [17], non-dissipative digital electronics [18] and fundamental metrology [19].
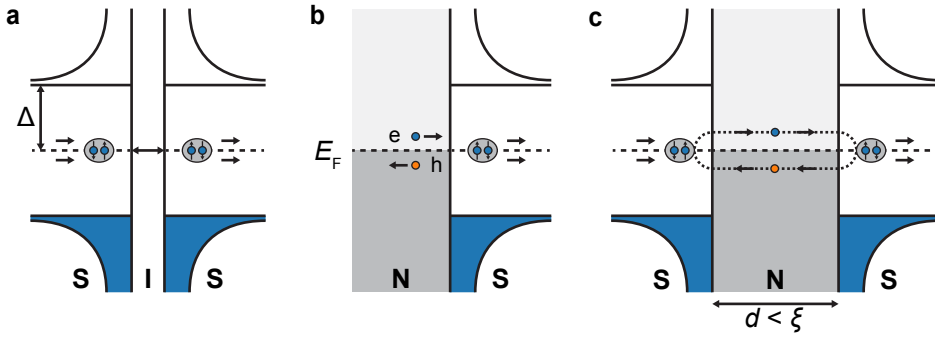
Figure 2.4: Josephson junctions **a** Two superconducting condensates separated by a thin insulating barrier. Correlated electron tunneling enables a supercurrent to flow when the superconductors are phase biased. **b** Andreev reflection describes the process by which an electron retroreflects as a hole from the interface, transferring a Cooper pair into the superconductor. **c** In the short junction limit ($d < \xi$), repeated phase coherent Andreev reflection at the two SN interfaces creates a local bound state called an Andreev bound state that transfers supercurrent when phase biased, as in a.

2.3.1. Tunnel junctions

Weak links between superconductors can come in many forms, but the original and in many ways simplest JJ is a superconductor-insulator-superconductor tunnel junction (see Fig. 2.4a) where two superconductors are separated by an insulating layer thinner than the mean free path of electrons (typically$\sim$ nm). Originally expected to act as a barrier to Cooper pairs, it was predicted and then experimentally verified that a finite supercurrent may pass the barrier via correlated tunneling of electrons to form Cooper pairs [20].

The Josephson effect describing this process depends on the phase difference ϕ between the two macroscopic superconducting condensates of phase Φ_1, Φ_2 :

$$\phi = \Phi_2 - \Phi_1 \tag{2.22}$$

In the simplest classical case the relationship between the supercurrent I_s and the phase ϕ is:

$$I_s = I_c \sin(\phi) \tag{2.23}$$

where I_c is the critical current of the JJ, with the voltage V across the junction then related to ϕ by [4, 21]:

$$\frac{\mathrm{d}\phi}{\mathrm{d}t} = \frac{2eV}{\hbar} \tag{2.24}$$

The Josephson energy E_J is the energy stored in a junction with a current of I_c flowing through it, and is an important parameter to control in the design of superconducting circuits, being defined as:

$$E_J = \frac{\Phi_0 I_c}{2\pi} \tag{2.25}$$

2.3.2. Andreev bound states

Although the most common, SIS tunnel junctions are only one type of JJ. Another type used extensively in this thesis is the superconductor-normal-superconductor (SNS) JJ where the two superconductors are separated by between 0.1 - 10 µm of a 'normal' material such as a metal or a semiconductor. Here the physical process by which supercurrent is transferred between the superconductors differs significantly from the SIS case. First, consider the interface between a superconductor and normal region (see Fig. 2.4b). Andreev reflection describes the process by which an electron retroreflects off the superconducting interface as a hole, transferring a Cooper pair into the superconductor in the process [22].

If the normal region is sandwiched between two superconductors, the retroreflected hole can be reflected from the other interface as an electron, allowing the process to repeat continuously resulting in a supercurrent (see Fig. 2.4c). As long as the transfer processes are phase coherent, this results in the creation of a pair of localised bound state called an Andreev bound state with energies $\pm E_A$.

Considering only the 1D case where the section of normal metal is smaller than the superconducting coherence length $d < \xi$, the JJ can be described by a number of conduction channels with transmission τ. The E_A of the two states then depends on ϕ and τ as [23]:

$$\pm E_A = \pm\Delta\sqrt{1 - \tau\sin^2(\phi/2)} \qquad (2.26)$$

Plotting Eq. 2.26 in Fig. 2.5a shows that E_A is highly dependent on ϕ, particularly at high τ. The dotted black line corresponds to the $\tau = 1$ case, which reduces down to the 4π periodic $E_A \pm \Delta\cos(\phi/2)$. The fact that generally $\tau < 1$ means that specular reflection as well as Andreev reflection can couple the two states, resulting in an energy gap $2\Delta\sqrt{1-\tau}$ at $\phi = \pi$ [23]. In thermal equilibrium at the temperatures of dilution refrigerators $T = 20\,\mathrm{mK} \ll 2\Delta\sqrt{1-\tau}$ only the ground state of the ABS is occupied, although this assumption must be reconsidered if $\tau \to 1$ or ϕ is varied non adiabatically. To calculate the total E_J of the JJ it is then sufficient to sum over the total number of ABSs, with each occupied subband of the JJ contributing exactly one ABS [23]:

$$E_J = \sum_i E_{A,i} = \Delta\sum_i\sqrt{1 - \tau_i\sin^2(\phi/2)} \qquad (2.27)$$

To find the total supercurrent of the junction and the phase dependence, one can follow the procedure described in [23] Appendix A to derive:

$$I_A = \frac{e\Delta}{2\hbar}\sum_i \frac{\tau_i\sin(\phi)}{\sqrt{1 - \tau_i\sin^2(\phi/2)}} \qquad (2.28)$$

recovering a supercurrent that is driven by a ϕ difference across the JJ. It should be noted here that one can recover the result for the SIS junction by considering many channels ($N \gg 1$) with low τ, causing the ABSs to be stuck to the superconducting gap Δ allowing Eq. 2.28 to be reduced to Eq. 2.23. In the case of our JJs
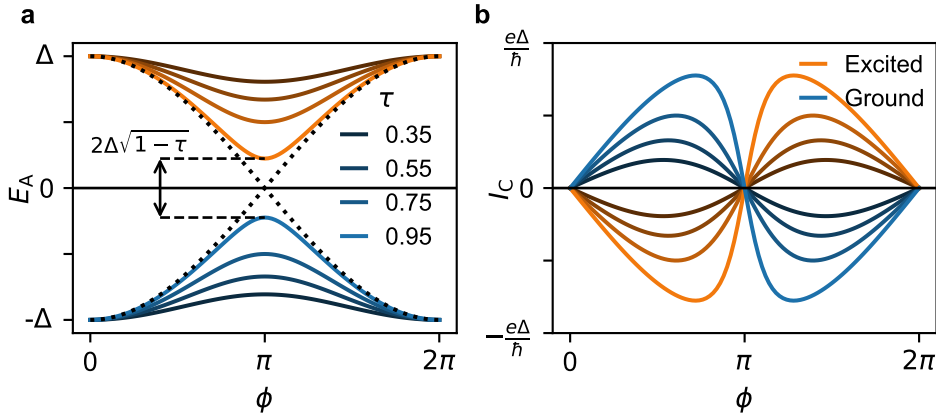
Figure 2.5: Andreev bound states **a** E_A plotted as a function of ϕ for varying τ. The ground state and excited state are coupled at finite τ by specular reflection, opening up an energy gap $2\Delta\sqrt{1-\tau}$ and making the spectrum 2π periodic. **b** Current phase relation for one ABS of varying τ. The ground (excited) state contributes a positive (negative) supercurrent, with higher τ producing more highly skewed current phase relationships.

with few channels and high τ it can be seen that the current phase relation (CPR) no longer has a sinusoidal character, but instead becomes highly skewed at high τ (see Fig. 2.5b).

2.4. Artificial atoms

Ever since the initial demonstration of the quantisation of energy levels on a Josephson junction [24], they have become the central component of solid state superconducting quantum information processing. In combination with superconducting islands they can produce a myriad of different 'artificial atoms', solid state superconducting circuits characterised by their anharmonic energy level structure. Their solid state state nature makes them easy to couple to readout and control circuits, whilst careful design of the level structures allows individual quantum levels to be addressed as qubits.

2.4.1. The Cooper pair box

The first and simplest macroscopic superconducting qubit to receive serious experimental attention is the Cooper pair box, the qubit that the transmon qubit is based on. It consists of a superconducting island that is connected to ground by a Josephson junction with a Josephson coupling E_J and capacitance C_J. An applied voltage V_g can then be applied via capacitively coupled gate (C_G) and used to tune the total charge on the island (see Fig. 2.6 for a circuit diagram). -

This is the simplest non-linear quantum oscillator, and can be analysed using
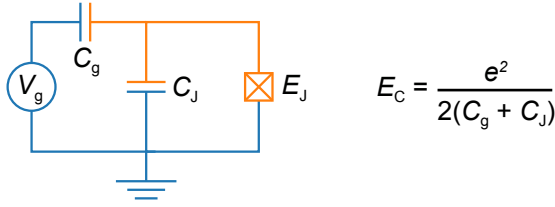
Figure 2.6: Circuit diagram of the Cooper pair box.

quantum circuit theory [25] to obtain the following Hamiltonian:

$$\hat{H} = 4E_C(\hat{n} - n_g)^2 - E_J \cos\hat{\phi} \tag{2.29}$$

This Hamiltonian is analagous to that of the hydrogen atom, with the charge that has tunnelled onto the island $Q = 2eN$ corresponding to momentum and the superconducting phase difference across the junction ϕ corresponding to the position [17]. Here $E_C = e^2/2(C_J + C_g)$ corresponds to the Coulomb charging energy required to move a charge on to the island with a residual offset charge on the capacitor of n_g caused by V_g.

Solving to find the eigenstates of Hamiltonian for varying E_J/E_C values, Fig. 2.7 shows the energy level structure of the first four eigenstates as a function of n_g normalised to the fundamental transition frequency $\omega_{01} \simeq (E_1 - E_0)/\hbar$. Fig. 2.7a shows the Cooper pair box regime where $E_J/E_C \sim 1$. At $n_g = 0.5$, the fundamental transition is $\omega_{01} \simeq E_J/\hbar$ with the energy spectrum being strongly anharmonic, allowing the ground and first excited state to be effectively treated as a two level system: a qubit.

2.4.2. The transmon

Although successful in demonstrating coherent control of a quantum degree of freedom in a macroscopic solid state circuit [27], the inherent sensitivity to gate charge noise proved to be a limiting factor for performance of the qubit. A derivative of the Cooper box called the transmon allows this sensitivity to be reduced by adding a large shunt capacitor (as in Fig. 2.8a, $C_{34} \gg C_J$) in parallel with the JJ. This suppresses E_C, increasing the ratio of E_J/E_C [26] which results in the charge dispersion flattening out (Fig. 2.7a-c). At $E_J/E_C > 50$ the charge dispersion is so flat that the qubit becomes insensitive to charge noise in n_g, with the fundamental transition $\omega_{01} \simeq \sqrt{8E_J E_C}/\hbar$ gaining a dependence on E_C in addition to E_J.

The large size of the capacitor now means capacitive couplings to other elements in the circuit become important when estimating E_C. In this case it is necessary to a full capacitance network as in Fig. 2.8b and use the process described in [26] to transform the network into an equivalent circuit of the same form as Fig. 2.6.

It should be noted that approximations for important device parameters derived from the Hamiltonian (such as ω_{01}) in this and further sections rely on being specifically in the Cooper pair box ($E_J/E_C \sim 1$) or the transmon regimes ($E_J/E_C >$
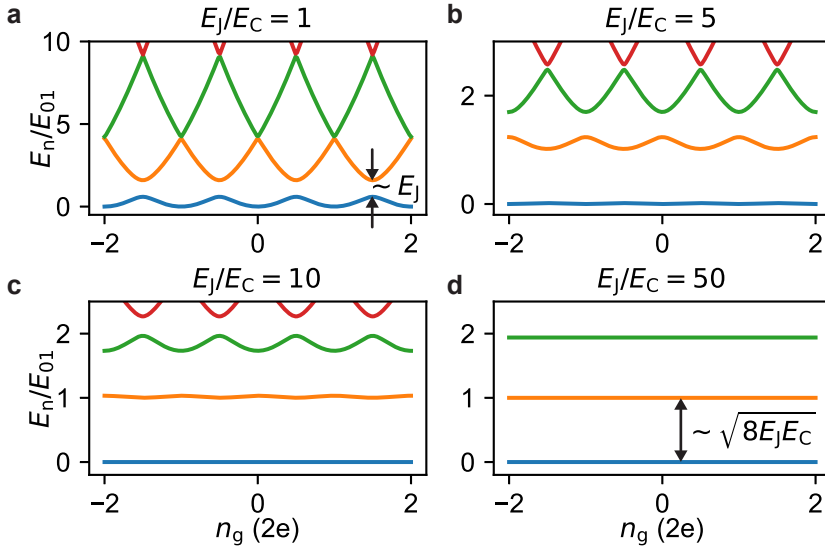
Figure 2.7: Energy level diagram of the Cooper pair box with varying values of E_J/E_C **a** With an $E_J/E_C = 1$ the spectrum is in the Cooper pair box regime, possessing an energy spectrum at $n_g = 0.5$ with a fundamental transition frequency of $\omega_{01} \simeq E_J/\hbar$ that is sufficiently anharmonic to be operated as a two level system. **b** As $E_J/E_C = 5$ is increased, the charge dispersion as a function of n_g starts to flatten, rendering the device less sensitive to charge fluctuations. **c** As $E_J/E_C = 10$ increases the dispersion flattens further. **d** At $E_J/E_C = 50$ the charge dispersion is so flat that the system is insensitive to charge noise, whilst still being sufficiently anharmonic that the fundamental transition $\omega_{01} \simeq \sqrt{8E_J E_C}/\hbar$ can be used as a qubit. Reproduced from [26].
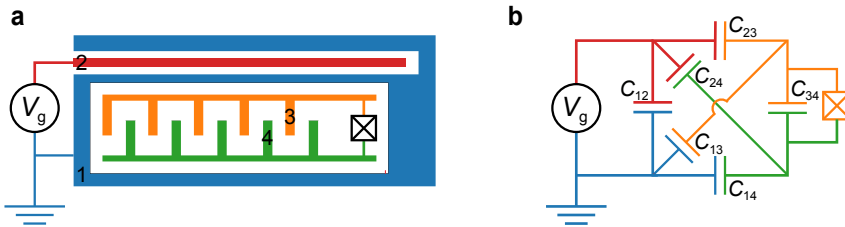
Figure 2.8: Circuit diagram of the transmon **a** Diagram demonstrating one possible design for a transmon, as used in Chap. 5. **b** Due to the large additional shunt capacitor C_{34}, a full capacitance matrix must solved in order to properly estimate E_C. Adapted from [26].

50). In the event that E_J/E_C is in the intermediary regime as in Chap. 7 the system must be modelled and studied with the full Hamiltonian, or approximations for that specific regime derived.

2.5. Circuit quantum electrodynamics

The field of circuit quantum electrodynamics is the study of the interaction between light and matter. By placing individual atoms inside highly reflective cavities filled with a photonic field, the quantum nature of light and matter can be manipulated. *Circuit* quantum electrodynamics is the extension of this field to solid state systems, where artificial atoms can be embedded in cavities and manipulated, making them an ideal platform for a solid state quantum computer.

In our systems, the artificial atom we use is the transmon qubit which we embed inside our superconducting resonators. Then, using circuit quantisation [25, 28] we generate a Hamiltonian for coupled system:

$$\hat{H} = 4E_C(\hat{n} - n_g)^2 - E_J \cos\hat{\phi} + \hbar\omega_r\hat{a}^\dagger\hat{a} + 2\beta e V_{rms}^0 \hat{n}(\hat{a} + \hat{a}^\dagger) \tag{2.30}$$

where $\hat{a}$ ($\hat{a}^\dagger$) are the creation (annihilation) operators for the harmonic cavity of the superconducting resonator of frequency $\omega_r = 1/\sqrt{L_r C_r}$, $V_{rms}^0 = \sqrt{\hbar\omega_r/2C_r}$ is the root means square voltage of the local oscillator and $\beta = C_g/C_\Sigma$ is the ratio of the capacitance of the gate and the total capacitance to ground [26].

The Hamiltonian can then be transformed to a basis of uncoupled transmon states $|i\rangle$ to obtain the generalised Jaynes-Cummings Hamiltonian that commonly used in cavity quantum electrodynamics:

$$\hat{H} = \hbar\sum_j \omega_j |j\rangle\langle j| + \hbar\omega_r\hat{a}^\dagger\hat{a} + \hbar\sum_{i,j} g_{ij} |i\rangle\langle j| (\hat{a} + \hat{a}^\dagger) \tag{2.31}$$

with couplings of $\hbar g_{ij} = 2\beta e V_{rms}^0 \langle i|\hat{n}|j\rangle$. In the transmon limit of large E_J/E_C this expression can be simplified further by using the fact that only adjacent transmon levels couple ($\langle j+k|\hat{n}|j\rangle \to 0$ for $k \neq 0$) and applying the rotating wave approximation to eliminate terms that describe simultaneous excitation (deexcitation) of the transmon and coupled harmonic oscillator to give the effective generalised Jaymes-Cummings Hamiltonian [26]:

$$\hat{H} = \hbar\sum_j \omega_j |j\rangle\langle j| + \hbar\omega_r\hat{a}^\dagger\hat{a} + \left(\hbar\sum_i g_{i,i+1} |i\rangle\langle i+1|\hat{a}^\dagger + H.C.\right) \tag{2.32}$$

2.5.1. Dispersive regime

In the case of transmon qubits, it is beneficial to operate them in the dispersive limit where their resonant frequencies are detuned strongly from the harmonic oscillator modes to maximise coherence and relaxation times. In this situation the detunings Δ_i are much greater than the transmon-resonator couplings $\Delta_i = (\omega_{i,i+1} - \omega_r) \gg g$, allowing us to eliminate the cavity-qubit interaction to the lowest order leading to

the effective Hamiltonian:

$$\hat{H}_{\text{eff}} = \frac{\hbar\omega'_{01}}{2}\hat{\sigma}_z + (\hbar\omega'_r + \hbar\chi\hat{\sigma}_z)\hat{a}^\dagger\hat{a} \tag{2.33}$$

Here the transmon is approximated to be a two level system of frequency ω_{01}, with the resonator ω_r acquiring a frequency shift of χ that is dependent upon the state of the qubit, allowing us to perform dispersive qubit readout by measuring the response of the resonator.

This Hamiltonian is the same as that for the Cooper pair box, except that low anharmonicity of the system means that virtual transitions through excited transmon states must be considered, resulting in some parameters (marked by primed symbols) such as $\omega'_r = \omega_r - \chi_{12}/2$ and $\omega'_{01} = \omega_{01} + \chi_{01}$ being renormalised. The form of χ is also modified to be an effective dispersive shift defined by:

$$\chi = \chi_{01} - \frac{\chi_{12}}{2} \simeq \frac{\alpha g^2}{\Delta(\Delta + \alpha)} \tag{2.34}$$

$$\chi_{ij} \equiv \frac{g_{ij}}{\omega_{ij} - \omega_r} \tag{2.35}$$

with $\omega_{ij} = \omega_i - \omega_j$ and the anharmonicity $\alpha = \hbar(\omega_{12} - \omega_{01})$.

2.6. Current phase relations in nanowire transmons

As the workhorse of the superconducting qubit community [29–32], one of the most important things about transmon qubits other than the long coherence times and ease of fabrication is that their physics is well understood, making it easy to model and predict the behaviour of large quantum circuits. Although nanowire based transmon qubits [33, 34] have a number of attractive features such as all electrical control and low power dissipation, the introduction of a JJ that can exhibit complex mesoscopic effects can have consequences that are interesting for us as physicists but possibly problematic for their integration into scaleable computing platforms, at least so long as the physics is not entirely understood.

Here we will summarise some of the effects that can be observed in nanowire based transmon qubits when the current phase relations of their JJs are modified by mesoscopic effects.

2.6.1. Coulomb blockade suppression

One of the more interesting effects observed to date in few channel nanowire transmons is the suppression of α in superconducting device as τ of the channels approaches 1 [35]. As the superconducting island becomes more strongly coupled to the reservoir, charge quantisation start to breakdowns due to quantum fluctuations, resulting in a modification of the Josephson potential and a suppression of Coulomb blockade in the device [35–37]. As material and fabrication improvements allow reliable fabrication of high quality JJs with $\tau \approx 1$ [38, 39], it is important to fully understand the effects this has on the mesoscopic devices under study.

Anharmonicity suppression

To understand the observed suppression of α in multiple InAs nanowire transmons, [35] describes a model that examines how a modification of the Josephson potential due to highly transmitting ABS channels results in corrections to the level structure that reduce the anharmonicity of the system, which we will summarise here.

First, consider again the CPB Hamiltonian described in Eq. 2.29 with the Josephson potential term $V(\hat{\phi})$ which in typical SIS transmons takes the form $V(\hat{\phi}) \propto \sin \phi$:

$$\hat{H} = 4E_C(\hat{n} - n_g)^2 - V(\hat{\phi}) \tag{2.36}$$

Instead for our SNS devices we must replace it with the ground state terms of the Andreev bound state potential described in Eq. 2.26:

$$V(\hat{\phi}) = -\Delta\sqrt{1 - \tau \sin^2(\hat{\phi}/2)} \tag{2.37}$$

By expanding $V(\hat{\phi})$ to the fourth order in $\hat{\phi}$:

$$V(\hat{\phi}) \approx \frac{\Delta}{4} \sum_i \left[\frac{\tau_i}{2}\hat{\phi}^2 - \frac{\tau_i}{24}\left(1 - \frac{3}{4}\tau_i\right)\hat{\phi}^4 \right] \tag{2.38}$$

And using the relation $E_J = \frac{\Delta}{4}\sum_i \tau_i$ we can derive $V(\hat{\phi})$:

$$V(\hat{\phi}) = E_J\frac{\hat{\phi}^2}{2} - E_J\left(1 - \frac{3\sum_i \tau_i^2}{4\sum_i \tau_i}\right)\frac{\hat{\phi}^4}{24} \tag{2.39}$$

Where we can see that the leading term corresponds to that of a harmonic oscillator $V_0(\hat{\phi}) = E_J\frac{\hat{\phi}^2}{2}$ with a perturbation $V'(\hat{\phi})$:

$$V(\hat{\phi}) = V_0(\hat{\phi}) + V'(\hat{\phi}) \tag{2.40}$$

Treating $V'(\hat{\phi})$ as a perturbation to the harmonic oscillator Hamiltonian $\hat{H}_0$ allows the correction to the energies to be calculated. Examining the matrix elements $\langle i | V'(\hat{\phi}) | i \rangle$ for $i = 0 - 2$ then gives:

$$\alpha \approx -E_C\left(1 - \frac{3\sum_i \tau_i^2}{4\sum_i \tau_i}\right) \tag{2.41}$$

Which gives $\alpha \simeq -E_C$ when $\tau_i \sim 0$ and a maximal suppression of $\alpha \simeq -E_C/4$ when $\tau_i = 1$. Intuitively this can be understood by comparing the case of $\tau = 0.75$ and $\tau = 1$ as depicted in Fig. 2.9a. In the case of $\tau = 0.75$, as ϕ is wound the finite transmission of the junction allows specular reflection to couple the ballistic ABS states, opening up a gap and allowing the system to relax to the ground state (as described in Sec. 2.3.2). At $\tau = 1$ this relaxation channel is suppressed, causing the state to continually raise in energy as ϕ is wound. This renders the effective $V(\hat{\phi})$ almost harmonic, strongly reducing the anharmonicity in the resulting level structure.
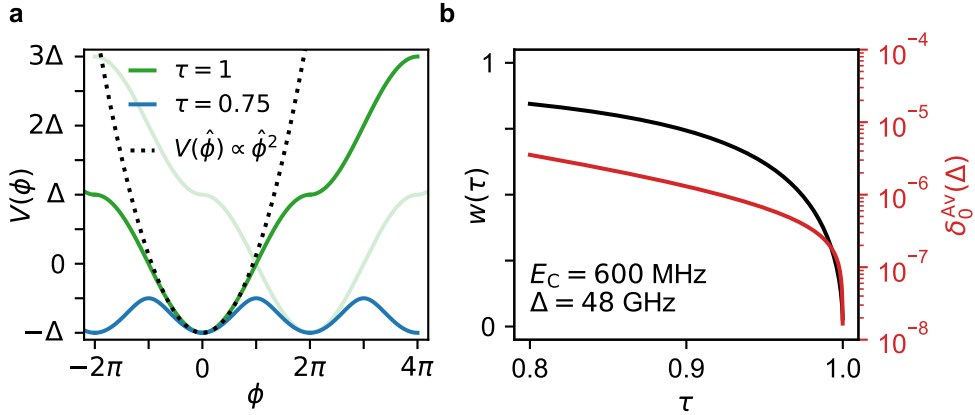
Figure 2.9: The effects of modified Josephson potentials **a** At $\tau = 1$ the specular reflection that would ordinarily open a gap and allow the system to relax to the ground state is suppressed, resulting in a strongly modified $V(\hat{\phi})$ that is more closely approximated by a harmonic potential that reduces the anharmonicity of the system eigenenergies. Light green represents another state of different occupation that crosses but does not couple with the dark green. **b** The Averin model is used to calculate the charge dispersion of ground state in a CPB with $E_C = 600\,\mathrm{MHz}$, $\Delta = 48\,\mathrm{GHz}$ (plotted in red). As with traditional SIS transmons, the charge dispersion decreases exponentially until $\tau \to 1$ where the additional prefactor w (plotted in black) causes to vanish completely to 0. Partially adapted from [37].

2.6.2. Charge dispersion suppression

In addition to the suppression of α, when $\tau = 1$ the inability to relax to the ground state of the ABS potential also acts to completely suppress Coulomb oscillations. This can be seen in Fig. 2.9a, as a continual increase in ϕ results in a continual increase in E. With no specular reflection, the levels cross but are not coupled, preventing charge tunnelling between adjacent charge states. To understand the effect this has on the expected charge dispersion, Averin [37] considers a model with a single mode junction and a continuum of modes to represent the superconducting contacts. In the regime with $\Delta \gg E_C, k_B T$ he calculates the probability w that an ABS will remain in the excited state as ϕ is wound for a given τ:

$$w = \frac{1}{\Gamma(\lambda)} \sqrt{\frac{2\pi}{\lambda}} \left(\frac{\lambda}{e}\right)^\lambda, \quad \lambda \equiv \frac{R}{2} \sqrt{\frac{\Delta}{4E_C}} \qquad (2.42)$$

where Γ is the Gamma function, λ is defined above and $R = 1 - \tau$. Note that the equation is slightly modified from [37] as the E_C in our case is the single electron charging energy. For τ varying between 0.8 and 1, w is plotted in Fig. 2.9b demonstrating that as $\tau \to 1$ the probability of relaxing to the low energy ABS branch is strongly suppressed.

As the amplitude of Coulomb blockade oscillations is proportional to w the charge dispersion of the levels becomes similarly suppressed, which for $R = 1 - \tau < E_C/\Delta$ results in a dispersion of the ground state δ_0^{Aver} given by:

$$\delta_0^{\text{Aver}} = 2\Delta b\tau w \left(\frac{4E_C}{2\pi^2\Delta\tau}\right)e^{-a\sqrt{\Delta\tau/E_C}} \tag{2.43}$$

where $a = 8(\sqrt{2} - 1) + R\ln R$ and $b = 8(\sqrt{2} - 1)$ for $\tau \to 1$. For a device with $E_C = 600\,\text{MHz}, \Delta = 48\,\text{GHz}, \delta_0^{\text{Aver}}$ is plotted as $\tau \to 1$. The charge dispersion can be seen to drop exponentially until very close to $\tau \to 1$ where it decreases at a much faster rate, where the additional prefactor w causes δ_0^{Aver} to vanish completely at $\tau \to 1$. This should be contrasted for the case of SIS transmons, which although specifically designed to reduce the effects of charge noise gives a dispersion δ_0^{Koch} that decreases 'only' exponentially [26]:

$$\delta_0^{\text{Koch}} = 2^5 E_C \sqrt{2/\pi}\left(\frac{E_J}{2E_C}\right)^{3/4} e^{-\sqrt{8E_J/E_C}} \tag{2.44}$$

As this model is valid only in the single channel limit, Chap. 7 uses a qualitatively similar model that is extended to two channels to produce preliminary analysis of suppressed charge dispersions.

2.6.3. Majorana bound states

Majorana bound states (MBSs) are quasiparticle excitations predicted to exist at the edges of superconductor-semiconductor heterostructures that have entered a 'topological phase'. A unique feature of these topological phases is the ability to classify them according to their 'topological invariant', a property of their wave-function immune to local perturbations that might allow for the storage of quantum information in a degree of freedom that is protected from the environment. This inherent protection, alongside their unique non-Abelian exchange statistics that would allow for the execution of protected quantum gates make them attractive building blocks for a possible topological quantum computer. This is a broad topic that this thesis only touches lightly on, so more thorough reading on the theory [40, 41], specific experimental implementations [42, 43] and initial signatures of Majorana bound states [44–46] are left as an exercise for the reader. The background and theory sections of [47] are also recommended as introductions to the physics of Kitaev chains and topological Josephson junctions.

The InAs-Al nanowires used in the nanowire transmons of Chap. 7 are predicted to host MBSs when the chemical potential μ has been tuned into a topological gap that has been opened via the application of a strong magnetic field perpendicular to the direction of spin-orbit interaction [42, 43]. It is worth considering whether such a transition to a topological phase would produce a set of unique signatures in the spectrum of the transmon qubit that could serve as the additional evidence for MBSs, possibly even allowing for initial steps towards topological quantum computation.

In this regime, MBS represented by the operator γ_i form at the two ends of the nanowire and at the interface between the superconductor and semiconductor sections that form the SNS JJ (see Fig. 2.10a). Here the wire is assumed to be sufficiently long that γ_1 does not couple to γ_2, similarly to γ_3 and γ_4, leaving only
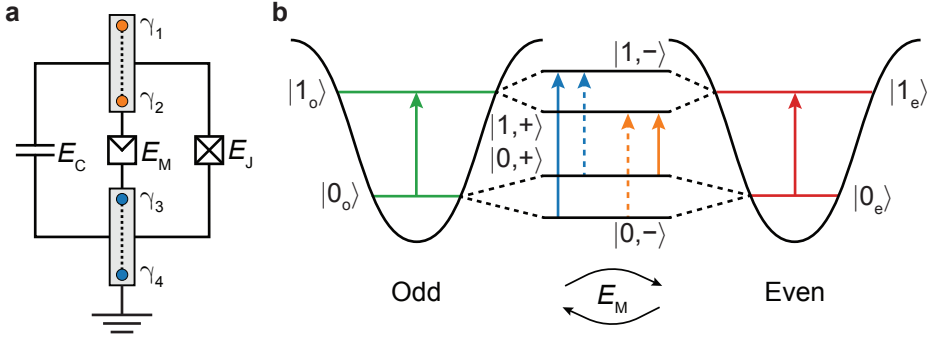
Figure 2.10: Majorana transmon qubits **a** Circuit diagram of a nanowire transmon qubit with E_C set by C, E_J by the SNS JJ and E_M by the coupling of γ_2 and γ_3. **b** Energy level diagram showing how the coherent coupling between the eigenstates of a transmon qubit and Majorana parity qubit create four separate transitions. Parity conserving transitions are denoted with solid lines. Adapted from [50]. Also used as Fig. 7.1.

the inner MBSs γ_2 and γ_3 to fuse to form a joint fermionic state that is described by the joint fermionic creation ($c^\dagger$) and annihilation (c) operators. Extending the Kitaev model to take the phase ϕ between the two superconductors into account, the operators γ_i can be constructed as [48, 49]:

$$\gamma_2 = (c^\dagger e^{\imath \Phi_2/2} + c e^{-\imath \Phi_2/2}) \tag{2.45}$$

$$\gamma_3 = \imath (c^\dagger e^{\imath \Phi_2/2} + c e^{-\imath \Phi_2/2}) \tag{2.46}$$

Where Φ_2 and Φ_3 are the phase of the superconductors hosting γ_2 and γ_3. The occupation n of the state is then defined as:

$$n = c^\dagger c = \frac{1}{2}(1 + \imath \gamma_2 \gamma_3) = \frac{1}{2}(1 - e^{\imath \delta/2}) + c^\dagger c \cos\left(\frac{\delta}{2}\right) \tag{2.47}$$

where we have redefined $\Phi_2 = -\phi/2$ and $\Phi_3 = \phi/2$ in terms of the phase difference ϕ. This is interesting as n is now 4π periodic, with a rotation of $\delta = 2\pi$ loading a fermion into the state and another rotation of $\delta = 2\pi$ loading it out. The energy of this bound state is now given by [48, 49]:

$$E_{\mathrm{MBS}} = \pm \Delta_{\mathrm{T}} \sqrt{\tau} \cos(\phi/2) \tag{2.48}$$

with Δ_{T} being the size of the topological gap. Interestingly this is not dissimilar to the case of a ballistic ABS where setting $\tau = 1$ in Eq. 2.26 gives:

$$E_{\mathrm{A}} = \pm \Delta \sqrt{1 - \sin^2(\phi/2)} = \pm \Delta \sqrt{\cos^2(\phi/2)} = \pm \Delta \cos(\phi/2) \tag{2.49}$$

Reiterating the importance of proximate measures that would allow one to distinguish between an ABS and an MBS. To understand the effect these modified Josephson potentials would have on the eigenstates of our transmon qubit, we

modify the Hamiltonian described in Eq. 2.7 by adding a term that describes the 4π effect that allows for coherent single electron transfer between the islands [50–52]:

$$\hat{H} = 4E_C(\hat{n} - n_g)^2 - E_J \cos(\hat{\phi}) + 2E_M \imath \hat{\gamma}_2 \hat{\gamma}_3 \cos(\hat{\phi}/2) \tag{2.50}$$

Making the substitution that $E_M = \Delta_T \sqrt{\tau}$. To understand the effect of this, it should be noted that the eigenstates of the CPB have even and odd branches that depend on the parity of the superconducting island. Ordinarily these eigenstate branches are completely decoupled, but with the addition of a coherent single electron transfer term E_M they start to couple, allowing for microwave induced transitions between eigenstates of different parity, a process that would previously have been forbidden. Fig. 2.10b shows how the coherent $1e$ transfer couples the previously separated parity subspaces, resulting in four total transitions instead of two. To illustrate the possible effects, we set E_J, E_C to values closely matching our device ($E_J = 4\,\text{GHz}, E_C = 0.8\,\text{GHz}$), vary E_M through three separate regimes and find the eigenstates of the Hamiltonian as in Sec. 2.4.2 to study the expected level structure and spectroscopic features. Setting $E_M = 10\,\text{MHz}$ to be less than the ground state dispersion δ_0 seems to give a level structure that does not deviate significantly from that of a transmon (Fig. 2.11a), with the excited state remaining a good parity eigenstate due to the small value of E_M (Fig. 2.11b). It can be seen in the ground E_M is small it starts to open up a comparably sizeable gap, flattening the charge dispersion of these levels and strongly mixing the parity states. As expected, the two tone spectroscopy of such a system (Fig. 2.11d) looks almost identical to the parity conserving transitions (solid lines) of the $E_M = 0\,\text{MHz}$ transmon case, with only slight additional features appearing at $n_g = 0.5$. Increasing $E_M = 0.2\,\text{GHz}$ causes visible splittings to open up in the level structure (Fig. 2.11e-h). E_M is now stronger than δ_0 and comparable to δ_1 making parity no longer a well defined eigenstate over a broad range of n_g allowing for additional non-parity preserving transitions (dotted lines) to be observed in the two-tone spectroscopy. Finally at $E_M = 1\,\text{GHz}$ the parity mixing transition is so strong that it dominates, strongly flattening the charge dispersions (Fig. 2.11i-k) and opening up a large gap of size E_M in the ground state that can be driven directly, with the parity conserving transitions almost entirely suppressed in spectroscopy (Fig. 2.11l).
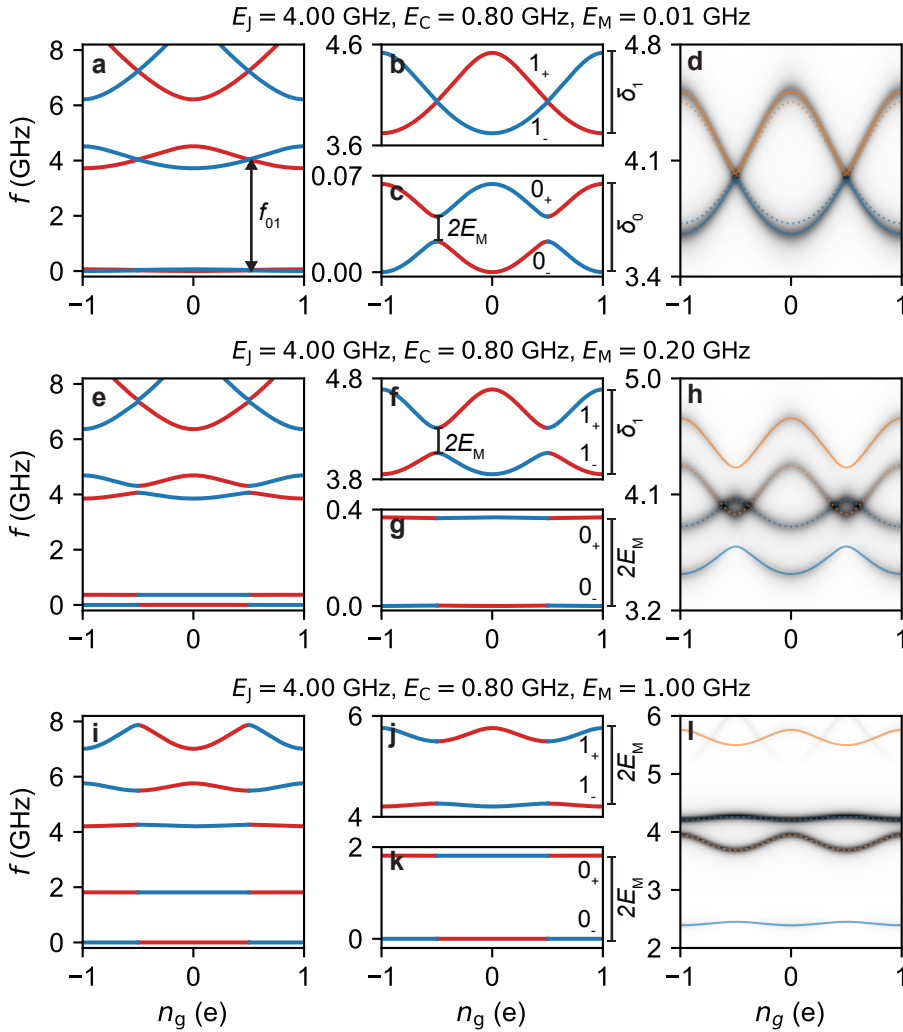
Figure 2.11: Energy level structure and spectroscopy of a Majorana transmon **a** With $E_M = 10\,\text{MHz}$ the level structure of the excited **b** and ground states **c** are not significantly affected, allowing parity conserving transitions(solid lines) to dominate, producing spectroscopy similar to that of a normal transmon **d**. Increasing $E_M = 0.2\,\text{GHz}$ opens up visible gaps in the structure **e**, causing the excited state to become strongly mixed **f** and flattening the charge dispersion of the ground level **g**, leading to additional features in spectroscopy from non-parity conserving transitions (dotted lines) **h**. At $E_M = 1\,\text{GHz}$ the parity mixing is so strong that the low level eigenstates **i-k** have their charge dispersion strongly suppressed, making the non-parity conserving transitions by far the most visible in spectroscopy **l**.

References

[1] File, J. & Mills, R. G. Observation of Persistent Current in a Superconducting Solenoid. *Physical Review Letters* **10**, 93–96 (1963).

[2] Kittel, C. *Introduction to solid state physics* (Wiley, 2005).

[3] Langford, N. K. Circuit QED - Lecture Notes (2013). `1310.1897`.

[4] Tinkham, M. *Introduction to Superconductivity* (Dover Publications Inc., 2004), second edn.

[5] Schuster, D. I. *Circuit Quantum Electrodynamics.* Ph.D. thesis, Yale University (2007).

[6] Megrant, A. *et al.* Planar superconducting resonators with internal quality factors above one million. *Applied Physics Letters* **100**, 113510 (2012).

[7] Wallraff, A. *et al.* Strong coupling of a single photon to a superconducting qubit using circuit quantum electrodynamics. *Nature* **431**, 162–167 (2004).

[8] Frunzio, L., Wallraff, A., Schuster, D., Majer, J. & Schoelkopf, R. Fabrication and characterization of superconducting circuit QED devices for quantum computation. In *IEEE Transactions on Applied Superconductivity*, vol. 15, 860–863 (2005).

[9] Collin, R. E. *Foundations for Microwave Engineering* (McGraw-Hill, New York, USA, 1992).

[10] Barends, R. *Photon-detecting superconducting resonators* (R. Barends, 2009).

[11] Pozar, D. M. *Microwave engineering* (Wiley, 2012).

[12] Clem, J. R. Inductances and attenuation constant for a thin-film superconducting coplanar waveguide resonator. *Journal of Applied Physics* **113**, 013910 (2013).

[13] Mazin, B. A. & A., B. Microwave kinetic inductance detectors. *Ph.D dissertation, 2005. 163 pages; United States – California: California Institute of Technology; 2005. Publication Number: AAT 3161146. DAI-B 66/01, p. 316, Jul 2005* (2005).

[14] Gao, J. *et al.* Experimental evidence for a surface distribution of two-level systems in superconducting lithographed microwave resonators. *Applied Physics Letters* **92**, 152505 (2008).

[15] Bruno, A. *et al.* Reducing intrinsic loss in superconducting resonators by surface treatment and deep etching of silicon substrates. *Applied Physics Letters* **106**, 182601 (2015).

[16] Song, C. Microwave Properties of Vortices in Superconducting Resonators (2011).

[17] Devoret, M. H., Wallraff, A. & Martinis, J. M. Superconducting Qubits: A Short Review (2004). 0411174.

[18] Likharev, K. & Semenov, V. RSFQ logic/memory family: a new Josephson-junction technology for sub-terahertz-clock-frequency digital systems. *IEEE Transactions on Appiled Superconductivity* **1**, 3–28 (1991).

[19] Jeanneret, B. & Benz, S. P. THE EUROPEAN PHYSICAL JOURNAL SPECIAL TOPICS Application of the Josephson effect in electrical metrology. *Eur. Phys. J. Special Topics* **172**, 181–206 (2009).

[20] Josephson, B. Possible new effects in superconductive tunnelling. *Physics Letters* **1**, 251–253 (1962).

[21] Likharev, K. K. Superconducting weak links. *Reviews of Modern Physics* **51**, 101–159 (1979).

[22] Andreev, A. F. Thermal Conductivity of the Intermediate State of Superconductors. Tech. Rep. 6 (1965).

[23] Bretheau, L. Localized Excitations in Superconducting Atomic Contacts: Probing the Andreev Doublet (2013).

[24] Martinis, J. M., Devoret, M. H. & Clarke, J. Energy-level quantization in the zero-voltage state of a current-biased Josephson junction. *Physical Review Letters* **55**, 1543–1546 (1985).

[25] Vool, U. & Devoret, M. Introduction to quantum electromagnetic circuits. *International Journal of Circuit Theory and Applications* **45**, 897–934 (2017).

[26] Koch, J. *et al.* Charge-insensitive qubit design derived from the Cooper pair box. *Physical Review A* **76**, 042319 (2007).

[27] Nakamura, Y., Pashkin, Y. A. & Tsai, J. S. Coherent control of macroscopic quantum states in a single-Cooper-pair box. *Nature* **398**, 786–788 (1999).

[28] Blais, A., Huang, R.-S., Wallraff, A., Girvin, S. M. & Schoelkopf, R. J. Cavity quantum electrodynamics for superconducting electrical circuits: An architecture for quantum computation. *Physical Review A* **69**, 062320 (2004).

[29] O'Malley, P. J. J. *et al.* Scalable Quantum Simulation of Molecular Energies. *Physical Review X* **6**, 031007 (2016).

[30] Colless, J. I. *et al.* Computation of Molecular Spectra on a Quantum Processor with an Error-Resilient Algorithm. *Physical Review X* **8**, 011021 (2018).

[31] Kandala, A. *et al.* Extending the computational reach of a noisy superconducting quantum processor (2018). 1805.04492.

[32] Sagastizabal, R. *et al.* Error Mitigation by Symmetry Verification on a Variational Quantum Eigensolver (2019). 1902.11258.

2

[33] De Lange, G. *et al.* Realization of microwave quantum circuits using hybrid superconducting-semiconducting nanowire Josephson elements. *Physical Review Letters* **115**, 127002 (2015).

[34] Larsen, T. W. *et al.* Semiconductor-nanowire-based superconducting qubit. *Physical Review Letters* **115**, 127001 (2015).

[35] Kringhøj, A. *et al.* Anharmonicity of a superconducting qubit with a few-mode Josephson junction. *Physical Review B* **97**, 060508 (2018).

[36] Jezouin, S. *et al.* Controlling charge quantization with quantum fluctuations. *Nature* **536**, 58–62 (2016).

[37] Averin, D. V. Coulomb Blockade in Superconducting Quantum Point Contacts. *Physical Review Letters* **82**, 3685–3688 (1999).

[38] Hays, M. *et al.* Direct Microwave Measurement of Andreev-Bound-State Dynamics in a Semiconductor-Nanowire Josephson Junction. *Physical Review Letters* **121**, 047001 (2018).

[39] Hart, S. *et al.* Current-phase relations of InAs nanowire Josephson junctions: from interacting to multi-mode regimes (2019). `1902.07804`.

[40] Nayak, C., Simon, S. H., Stern, A., Freedman, M. & Das Sarma, S. Non-Abelian anyons and topological quantum computation. *Reviews of Modern Physics* **80**, 1083–1159 (2008).

[41] Beenakker, C. Search for Majorana Fermions in Superconductors. *Annual Review of Condensed Matter Physics* **4**, 113–136 (2013).

[42] Lutchyn, R. M., Sau, J. D. & Das Sarma, S. Majorana fermions and a topological phase transition in semiconductor-superconductor heterostructures. *Physical Review Letters* **105**, 077001 (2010).

[43] Oreg, Y., Refael, G. & Von Oppen, F. Helical liquids and Majorana bound states in quantum wires. *Physical Review Letters* **105**, 177002 (2010).

[44] Mourik, V. *et al.* Signatures of majorana fermions in hybrid superconductor-semiconductor nanowire devices. *Science* **336**, 1003–1007 (2012).

[45] Deng, M. T. *et al.* Observation of Majorana Fermions in a Nb-InSb Nanowire-Nb Hybrid Quantum Device. *Nano Letters* **12**, 6414–6419 (2012).

[46] Deng, M. T. *et al.* Majorana bound state in a coupled quantum-dot hybrid-nanowire system. *Science* **354**, 1557–1562 (2016).

[47] van Woerkom, D. Semiconductor Nanowire Josephson Junctions: In the search for the Majorana (2017).

[48] Fu, L. & Kane, C. L. Josephson current and noise at a superconductor-quantum-spin-Hall-insulator-superconductor junction. *Physical Review B* **79**, 161408 (2009).

[49] Badiane, D. M., Glazman, L. I., Houzet, M. & Meyer, J. S. Ac Josephson effect in topological Josephson junctions. *Comptes Rendus Physique* **14**, 840–856 (2013).

[50] Ginossar, E. & Grosfeld, E. Microwave transitions as a signature of coherent parity mixing effects in the Majorana-transmon qubit. *Nature Communications* **5**, 4772 (2014).

[51] Hassler, F., Akhmerov, A. R. & Beenakker, C. W. J. The top-transmon: a hybrid superconducting qubit for parity-protected quantum computation. *New Journal of Physics* **13**, 095004 (2011).

[52] Yavilberg, K., Ginossar, E. & Grosfeld, E. Fermion parity measurement and control in Majorana circuit quantum electrodynamics. *Physical Review B* **92**, 075143 (2015).

2

3

Fabrication and experimental methods

"Highly organized research is guaranteed to produce nothing new."

Frank Herbert

This chapter serves as an overview for the fabrication and measurement of the devices used throughout this thesis.

This chapter serves to describe techniques necessary to create hybrid circuit quantum electrodynamics (cQED) devices. Initially, the fabrication of superconducting resonators will be described, followed by the fabrication recipes used to create the various Josephson junctions used in this thesis. Finally, the equipment and techniques necessary to measure hybrid cQED devices will be summarised.

3.1. Fabrication

3.1.1. Superconducting coplanar waveguide resonators

The superconducting resonators used in every chapter of this thesis are fabricated from sputtered NbTiN films. NbTiN is an ideal material for the fabrication of high Q superconducting resonators due to its hardness, large superconducting gap Δ, low microwave phase noise [1], low loss [2] and resistance to oxidation. Initially the wafers are cleaned to remove any organic residue, preventing losses that might occur at the substrate film interface. Three separate types of wafer are used in this thesis, single crystal sapphire Al_2O_3 (Chap. 4,6), intrinsic Si (Chap. 5) and an intrinsic Si/SiN$_x$ stack (Chap. 7), with the preparation required for each wafer described in Table. 3.1.

After wafer preparation, the wafers are then loaded into an AJA sputtering system with a base pressure $P \simeq 10^{-9}$ mTorr. NbTiN is then sputtered for the desired length of time in an Ar/N atmosphere while rotating the wafer to ensure even coverage. If necessary, a voltage bias can be applied to the wafer using a voltage source and a heater used to increase the temperature of the wafer during deposition. Markers which are used to align subsequent layers of lithography are fabricated by defining a regular array of square 20 μmx 20 μm in PMMA resist using electron beam lithography (EBL). After exposure, the PMMA is developed, 5/80 nm Ti/Au evaporated and the PMMA layer dissolved in hot acetone. Following from this, the wafer can be protected using a thick layer of photoresist (AZ9260) and diced into 1 cmx1.5 cm squares for smaller batch processing of devices. Our devices can then be defined in these NbTiN chips by using EBL to expose a high resolution etch-resistant resist layer (such as ZEP520A or CSAR 6200) that has been spun on top of the chip, developed and then etched in a reactive ion etcher (RIE) in an SF_6/O_2 plasma.

Wafer Composition	Processing
Al_2O_3	Nitric acid clean (in ultrasound)
	Deionised water wash
	IPA wash
	Compressed nitrogen drying
Si	Native oxide strip in HF
	Deionised water wash
	Compressed nitrogen drying
Si/SiN_x	Native oxide strip in HF
	Deionised water wash
	Marangoni drying
	Low stress LPCVD SiNx deposition (100nm)
	Nitric acid clean (in ultrasound)
	Deionised water wash
	IPA wash
	Compressed nitrogen drying

Table 3.1: Processing steps for each wafer before NbTiN deposition.

3.1.2. Encapsulated graphene Josephson junctions

The encapsulated graphene Josephson junctions used in this thesis were created using deterministic transfer techniques [3] that entirely encapsulate few-layer graphene sheets between sheets of hexagonal boron nitride (hBN) dielectric [4] to create high quality hBN-graphene-hBN stacks. We follow the fabrication process detailed more fully in [5], with the notable exceptions that we use PMMA instead of an MMA/MAA copolymer and have an additional step before stack transfer that allows for complete removal of unwanted hBN/graphene flakes that might adversely affect the microwave performance of our devices. The bottom graphene and hBN flakes are mechanically exfoliated from natural graphite and hBN single crystals using blue Nitto tape onto Si substrates with thermally grown SiO top layers (see Fig. 3.1a). The top hBN flake is prepared directly on polymer coated transparent substrates. The substrates consist of a microscope glass slide with a 1x1 cm^2 PDMS film, on top of which we spin a layer of PMMA resist.

The glass plate is mounted on to an XYZ stage, where a microscope is used to align the flakes so that the stack can be assembled (see Fig. 3.2). The heater is used to to modify the van der Waals forces between the flake, substrate and PMMA during the graphene pickup process (see Fig. 3.1b), allowing it to be deterministically picked up and placed on top of a bottom hBN flake. Unwanted flakes of graphene and hBN that are deposited during the transfer process are removed by using EBL to define an etch mask in HSQ that has been spun on the substrate. The substrate is then cleaned using using an SF_6/He/O RIE etch. Finally, the HSQ is removed using a 25 s 1:7 buffered HF wet etch, before the stack is deterministically picked up and transferred to the sample substrate using the process described previously.
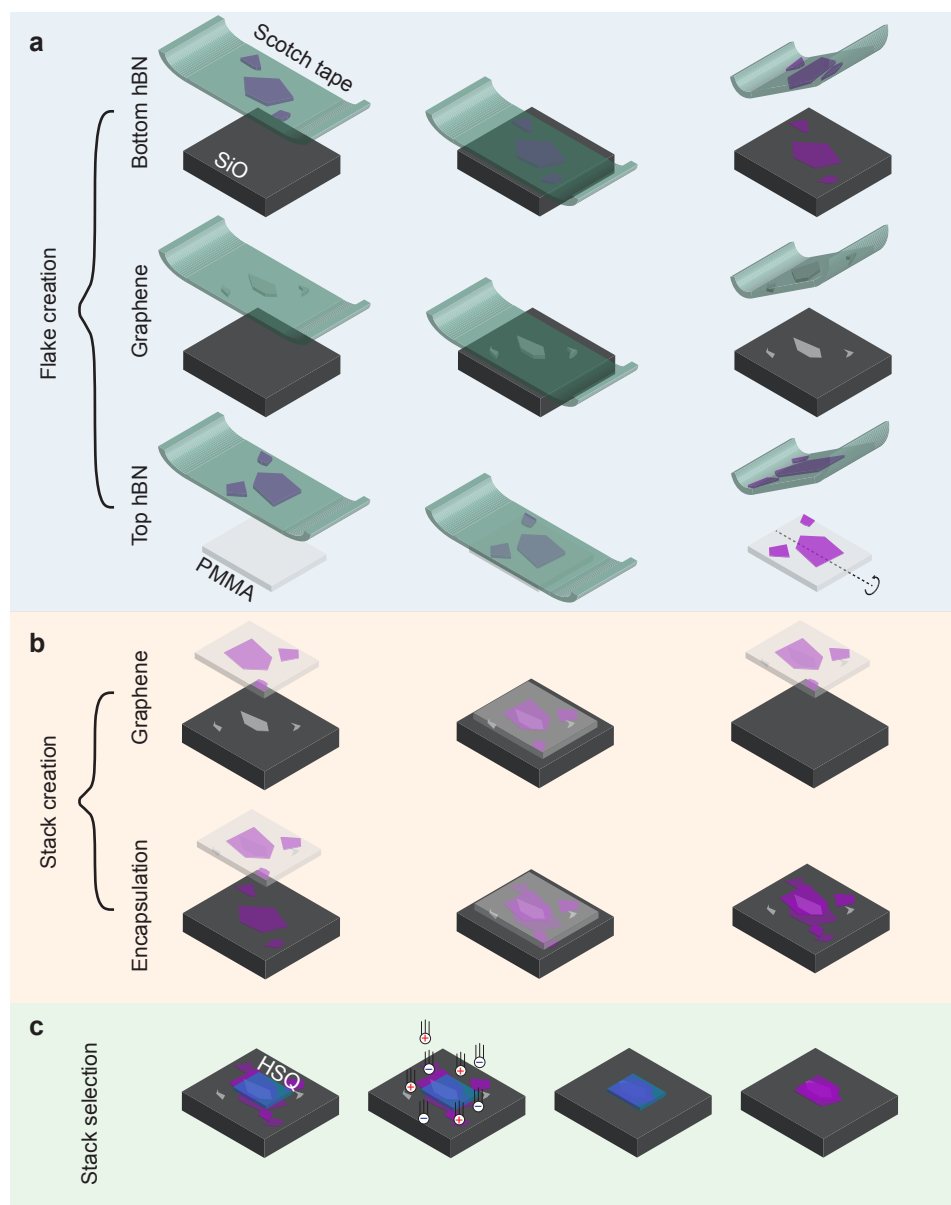
Figure 3.1: Flake creation process **a** Nitto tape is used to repeatedly cleave graphene/hBN single crystals into few layer crystals which are then pressed onto SiO or PMMA substrates, where van der Waals forces cause few-layer crystals to adhere. **b** The PMMA substrate is flipped, then placed in the the XYZ stage. The camera setup is then used to pickup a graphene monolayer using the van der Waals attraction to the top hBN layer. Modifying the substrate temperature using the hotplate helps separate the flake from the SiO. The stack is then fully encapsulated by repeating the process to deposit the top hBN + graphene on the bottom hBN. **c** The stack is then selected by using EBL to define an HSQ mask which protects the stack during an RIE process. After etching, the HSQ is removed using a HF dip. The stack can then be picked up and deterministically placed as in b.
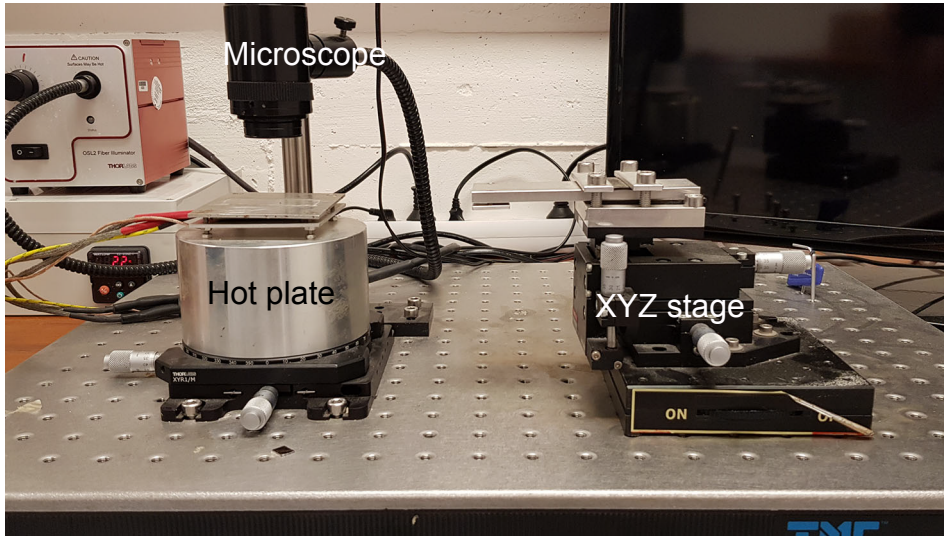
Figure 3.2: Stack transfer stage. A microscope and XYZ movement stage are used to align, pick up and deposit hBN and graphene flakes during the encapsulation process. A hot plate is used to control the substrate temperatures, helping individual flakes to adhere or separate from the substrate as necessary.

3.1.3. Semiconducting nanowire Josephson junctions

The Josephson junctions used in Chap. 6,7 were created from InAs semiconducting nanowires with epitaxial layers of Al on two of the nanowire facets. The InAs nanowires are grown in the wurzite direction [0001] using molecular beam epitaxy (MBE) and the vapour-liquid-solid (VLS) method on InAs substrates (Fig. 3.3a). After the nanowires have reached a sufficient length, the Al shell is deposited on two facets via an angled deposition at low temperature *in situ* (Fig. 3.3b) [6]. Careful control of the growth conditions allows for epitaxial lattice matching, greatly improving the quality of the superconductor-semiconductor interface (Fig. 3.3c).

After growth, a deposition stage similar to [8] is used to deterministically transfer wires as described in [9]. As this transfer method allows for both the position and orientation of the wire to be precisely controlled, the wire can be pre-aligned with the axis of the magnet and simultaneously aligned with the fine gate structure that allows for optimal gate tuning.

3.2. Experimental methods

3.2.1. Cryogenics

Unless otherwise stated, all experiments in this thesis were conducted in a Oxford Triton dry dilution refrigerator (Fig. 3.4a), which is capable of reaching a base temperature of $T \simeq 15\,\mathrm{mK}$. The cooling liquid consists of a mixture of ^{3}He and ^{4}He isotopes which when forced through an impedance and cooled by the outgoing He mix via the heat exchangers, condenses onto the mixing chamber filling the system up to the still (see Fig. 3.4b). At sufficiently low temperatures, the He mixture sep-

3

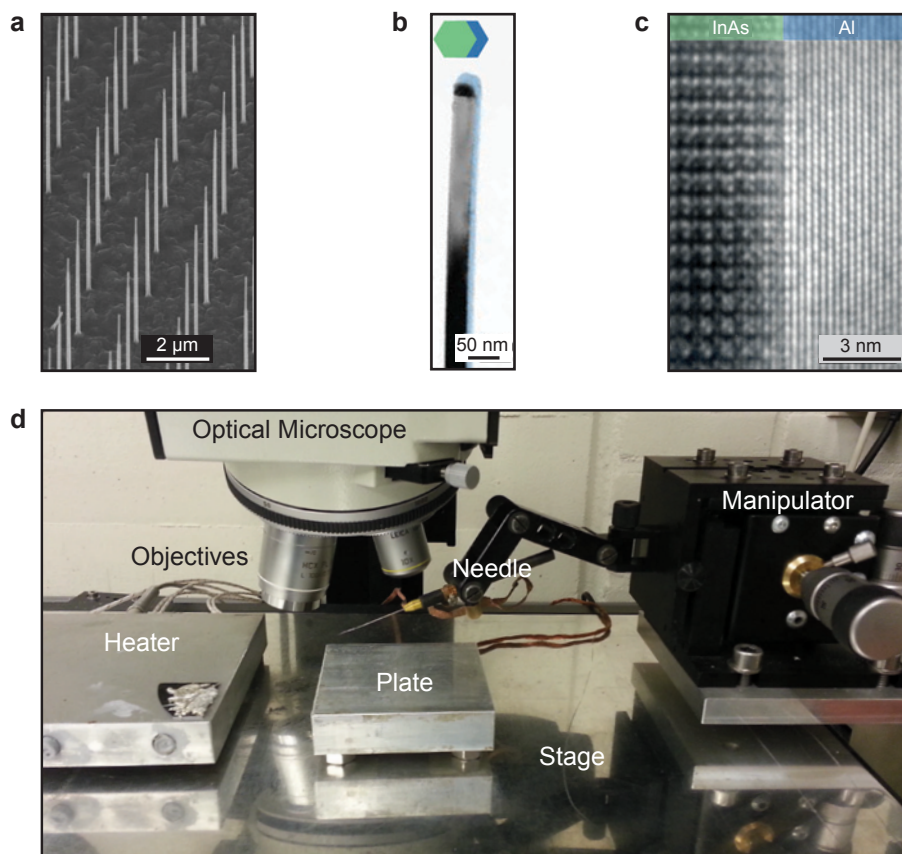Figure 3.3: Wire growth and transfer **a** InAs nanowires are grown via MBE using the VLS method on InAs substrates. **b** After growth, Al is deposited on two facets using low temperature angled deposition. **c** The Al layer is a grown epitaxially as a single crystal with ideal lattice matching. Figures a-c adapted from [6]. Figure d adapted from [7]
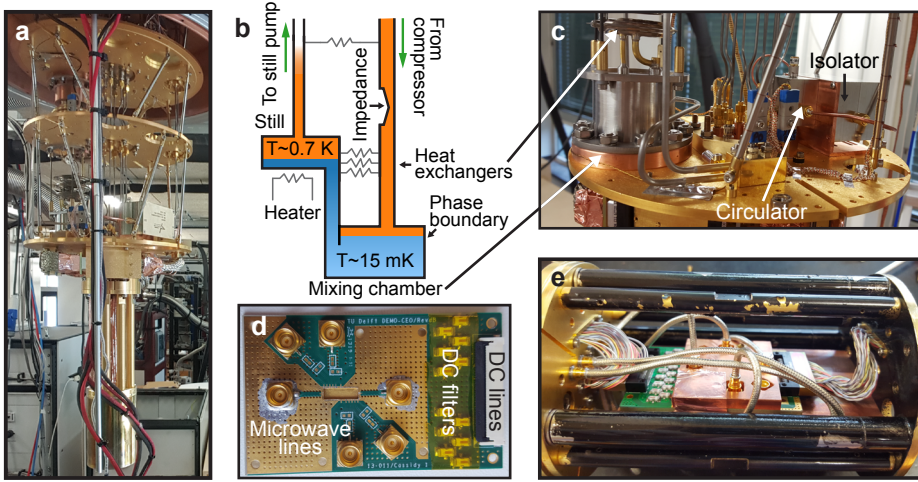
Figure 3.4: Cryogenics and sample mounting **a** Optical image showing an Oxford Triton refrigerator with the vacuum and shielding canisters removed. **b** Schematic diagram of the internal components in a dry dilution refrigerator. Adapted from [10]. **c** Optical image of the mixing chamber, showing the mixing chamber and heat exchangers, as well as the high frequency wiring and circulator/isolators used during microwave measurements. **d** Optical image of the printed circuit boards used for experiments requiring DC and RF measurements. **e** Optical image of a DC/RF PCB mounted inside a fast sample exchange puck.

arates into a pure ^{3}He phase and a dilute mixed phase consisting of ^{3}He and ^{4}He. As the ^{3}He vapour is pumped from the still and removed from the dilute phase, the concentration inside the liquid phase decreases, resulting in an osmotic pressure that draws ^{3}He from the mixing chamber to the still. The reduced ^{3}He density in the dilute phase at the mixing chamber causes the ^{3}He to be drawn through the phase boundary, where energy is absorbed via the enthalpy of mixing, cooling the mixing chamber. This cooling can be carried out continuously by circulating the ^{3}He through the system with a compressor [10].

3.2.2. Fridge wiring and sample mounting

The experiments described in this thesis are unique in that both DC transport and microwave frequency RF measurements can be performed simultaneously. 'Dry' dilution refrigerators enable this by significantly increasing the area in which to place DC and microwave lines, as well as the filters, circulators and isolators necessary to ensure the electrons thermalise with the temperature of the fridge at each cooling stage (see Fig. 3.4c and Sec. 5.1.2 for a more in depth explanation).

The fast sample exchange system so crucial for experiments on mesoscopic devices with low yield and ESD sensitivity does have a significant drawback showever - it severely complicates the shielding required by the sensitive superconducting devices in this thesis. A more detailed discussion of the methods used to shield samples from their electromagnetic environment is described in Sec. 7.7.3.

Fig. 3.4d shows custom printed circuit boards (PCBs) that were designed to

accept standard 2x7 mm samples and interface them to the DC and microwave lines in the sample exchange pucks. Low pass filters help reduce noise on the DC lines, with several of the DC lines being routed to bonding pads that allow either an RF, DC or bias tee to be constructed on each sample board as necessary for the experiment (Fig. 3.4d). In this image, the samples are shielded from radiation using a copper enclosure (Fig. 3.4e).

References

[1] Barends, R. *et al.* Reduced frequency noise in superconducting resonators. *Applied Physics Letters* **97**, 033507 (2010).

[2] Bruno, A. *et al.* Reducing intrinsic loss in superconducting resonators by surface treatment and deep etching of silicon substrates. *Applied Physics Letters* **106**, 182601 (2015).

[3] Castellanos-Gomez, A. *et al.* Deterministic transfer of two-dimensional materials by all-dry viscoelastic stamping. *2D Materials* **1**, 011002 (2014).

[4] Dean, C. R. *et al.* Boron nitride substrates for high-quality graphene electronics. *Nature Nanotechnology* **5**, 722–726 (2010).

[5] Calado, V. E. *et al.* Ballistic Josephson junctions in edge-contacted graphene. *Nature Nanotechnology* **10**, 761–764 (2015).

[6] Krogstrup, P. *et al.* Epitaxy of semiconductor–superconductor nanowires. *Nature Materials* **14**, 400–406 (2015).

[7] van Woerkom, D. Semiconductor Nanowire Josephson Junctions: In the search for the Majorana (2017).

[8] Flöhr, K. *et al.* Manipulating InAs nanowires with submicrometer precision. *Review of Scientific Instruments* **82**, 113705 (2011).

[9] Van Woerkom, D. Majorana fermions in well aligned InSb-nanowires with superconducting and normal contacts (2012).

[10] Graham Batey & Gustav Teleberg. Principles of dilution refrigeration - A brief technology guide. Tech. Rep., Oxford Instruments (2015).

4

Magnetic field resilient superconducting coplanar waveguide resonators for hybrid cQED experiments

J. G. Kroll, F. Borsoi, K. L. van der Enden, W. Uilhoorn, D. de Jong, M. Quintero-Peréz, D. J. van Woerkom, A. Bruno, S. R. Plissard, D. Car, E. P. A. M. Bakkers, M. C. Cassidy, L. P. Kouwenhoven

Superconducting coplanar waveguide resonators that can operate in strong magnetic fields are important tools for a variety of high frequency superconducting devices. Magnetic fields degrade resonator performance by creating Abrikosov vortices that cause resistive losses and frequency fluctuations, or suppressing superconductivity entirely. To mitigate these effects we investigate lithographically defined artificial defects in resonators fabricated from NbTiN superconducting films. We show that by controlling the vortex dynamics the quality factor of resonators in perpendicular magnetic fields can be greatly enhanced. Coupled with the restriction of the device geometry to enhance the superconductors critical field, we demonstrate stable resonances that retain quality factors $\simeq 10^5$ at the single photon power level in perpendicular magnetic fields up to $B_\perp \simeq 20\,\text{mT}$ and parallel magnetic fields up to $B_\parallel \simeq 6\,\text{T}$. We demonstrate the effectiveness of this technique for hybrid systems by integrating an InSb nanowire into a field resilient superconducting resonator, and use it to perform fast charge readout of a gate defined double quantum dot at $B_\parallel = 1\,\text{T}$.

4.1. Introduction

Superconducting (SC) coplanar waveguide (CPW) resonators are invaluable tools for parametric amplifiers [1, 2], photon detectors that operate from the infra-red to X-ray frequencies [3–5] and hybrid systems that couple superconducting circuits to cold atoms [6], solid state spins ensembles [7–9], nanomechanical resonators [10, 11] and semiconducting devices [12–18]. They are also a key component in a variety of quantum computing (QC) platforms, where they are used for readout, control and long-range interconnection of superconducting [19–22], semiconducting [23–26] and topological [27, 28] qubits.

A common requirement among these schemes is that the SC resonators be low loss in order to minimize unwanted relaxation via the Purcell effect [29] and maximize two qubit gates fidelities [30]. Significant progress has been made in identifying the major loss mechanisms involved. Abundant defects in amorphous materials that couple dissipatively to the electric field of SC CPW resonators and act as effective two level systems (TLSs) were the first to be identified [31]. Their detrimental effects can be mitigated by minimizing the interface area and improving the quality of interfaces. Subsequently, stray infrared radiation was shown to generate quasiparticles in the SC, significantly increasing losses and necessitating multi-stage radiative shielding to isolate the resonators from their environment [32]. In addition, when fabricated from type II superconductors, even small magnetic fields ($B_{c_1} \simeq 1\,\mu T$) result in the creation of Abrikosov vortices: regions of supercurrent that circulate a non-superconducting core. When exposed to high frequency radiation the Lorentz force causes them to oscillate, generating quasiparticles and increasing losses [33]. Encasing the resonators in multiple layers of magnetic shielding strongly suppresses the number of vortices generated by local magnetic fields, while the use of a type I SC such as Al allows for complete expulsion of magnetic flux via the Meissner effect. Through a combination of these techniques, internal quality factors (Q_i) in excess of 10^6 have been demonstrated at the single photon power levels [34, 35].

Many semiconducting and topological QC schemes are accompanied by an additional requirement: strong magnetic fields that approach and sometimes exceed $B = 1\,T$. This renders traditional magnetic shielding methods useless and destroys the superconductivity of the Al commonly used to fabricate SC CPW resonators ($B_c \simeq 10\,mT$ for bulk Al). One possible solution utilizes type II superconductors with high upper critical magnetic fields such as MoRe, TiN or NbTiN, allowing the superconductivity to persist in very strong magnetic fields ($B_{c_2}^{MoRe} > 8\,T$ [36], $B_{c_2}^{NbTiN} > 9\,T$ [37]) while possessing a low enough density of TLSs to allow high Q_i resonators at zero field [38, 39]. In order to create high Q_i SC resonators that can survive in strong magnetic fields, controlling the creation and dynamics of Abrikosov vortices is key. Previous studies have utilized the intrinsic disorder in NbTiN [40] and YBCO [41] films, or lithographically defined artificial defect sites [42] to pin the vortices, preventing dissipation and demonstrating moderate quality factors up to 10^4 in parallel magnetic fields. In other studies, the resonator geometry has been restricted below the superconducting penetration depth to prevent the formation of vortices entirely [43–46]. Impressively, nanowire resonators have achieved Q_i of

10^5 at $B_\parallel \simeq 6\,\text{T}$ and $Q_i = 10^4$ at $B_\perp = 350\,\text{mT}$, however this non-standard geometry may hinder their implementation into complex systems due to the challenging lithography, the required removal of the ground plane and the strong sensitivity of the resonator frequency to variations in the film's kinetic inductance. When considering reliability and scalability, devices based on CPW resonators that have been rendered field compatible may be preferable.

In this work we demonstrate that thin film NbTiN SC CPW resonators with lithographically defined artificial defect sites (hereafter referred to as 'holes') can retain a high Q_i in strong magnetic fields. We first study how the SC film thickness affects the response and Q_i of resonators in parallel magnetic fields in order to optimize field resilience. We then determine how the hole density affects the dynamics of Abrikosov vortices, enabling $Q_i \simeq 10^5$ to be retained in perpendicular magnetic fields up to $B_\perp \simeq 20\,\text{mT}$. Combining these results, we reduce the number of vortices that are generated by restricting the film thickness and utilize holes to control the vortices that do occur. This allows $Q_i \simeq 10^5$ at single photon power levels to be retained up to $B_\parallel \simeq 6\,\text{T}$. Finally, we use these patterned resonators to perform fast charge readout of a hybrid InSb nanowire double quantum dot device at $B_\parallel = 1\,\text{T}$.

4.2. Methods

The superconducting CPW resonators are fabricated from NbTiN films sputtered from a 99.99% purity NbTi target in an Ar/N atmosphere onto 2 inch 430 μm thick sapphire (0001) orientation wafers. A typical 100 nm film has a T_c of 14 K, a resistivity of 123 μΩ cm and stress of -400 MPa. The resonators are defined using electron beam lithography (EBL) and a subsequent reactive ion etch (RIE) in an SF_6/O_2 atmosphere and if desired, holes can be patterned and etched in the same step. After fabrication, the samples are mounted in a light tight copper box and thermally anchored to a dilution refrigerator with a base temperature of 15 mK. The complex microwave transmission S_{21} through the sample is measured using standard heterodyne demodulation techniques (Fig. 4.1a) which allow the complex transmission S_{21} to be measured as the probe frequency f is varied. The input line to the sample is heavily attenuated, which suppresses thermal noise and allows the cavity photon occupancy to reach below a single photon. An external magnetic field is applied to the sample with a 3-axis 6-1-1 T vector magnet. The circulators used in this study are magnetically shielded to prevent stray fields from interfering with their operation. Two different types of samples are used in this study. The first, used for characterization experiments, contains several $\lambda/4$ resonators multiplexed to a single feedline (Fig. 4.1b-d). This allows for the coupling quality factor Q_c and internal quality factor Q_i to be accurately determined by fitting the transmission spectra. In the second geometry, we use a $\lambda/2$ resonator geometry that is integrated with a nanowire double quantum dot. In this case, we only fit the loaded quality factor Q_l. All internal quality factors reported in this manuscript correspond to single photon power levels. See Supplementary Information for detailed notes on fitting procedures and device parameters.
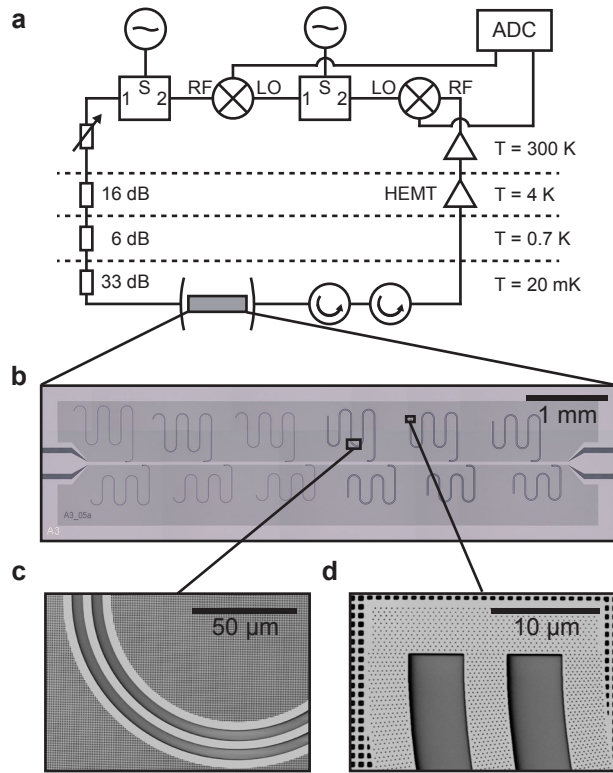
4

Figure 4.1: **a** Circuit diagram of the heterodyne detection circuit, allowing the complex transmission S_{21} to be measured. **b** A cropped optical image showing a typical device with multiple $\lambda/4$ resonators frequency multiplexed to a common feedline and surrounded by a patterned ground plane. SEM micrographs of a SC CPW resonator without **c** and with holes **d**.

4.3. Film thickness dependence

We first utilize the critical field enhancement observed in thin strips of type II super-conductors [43]. Application of a magnetic field along an axis where the thickness t is significantly smaller than the penetration depth λ results in complete expulsion of vortices below an enhanced critical field. This enhanced field takes the form: $B_{c_1} = 1.65\Phi_0/t^2$, where Φ_0 is the magnetic flux quantum and t is the film thickness [43, 44]. Calculating B_{c_1} for a 22 nm film suggests that the first vortex nucleates at $B_{c_1} = 7.05$ T for a perfectly aligned field, an improvement of many orders of magnitude compared to a bulk film.

To investigate this effect a series of SC CPW resonators without holes were fabricated on 4 different NbTiN films of thicknesses 8 nm, 22 nm, 100 nm and 300 nm (Fig. 4.2 a). λ can be estimated in extremely dirty type II superconductors for $T \to 0$ K as $\lambda = \sqrt{\hbar\rho/\pi\mu_0\Delta_0}$ [47] with $\hbar$ being the reduced Planck constant, ρ the film resistivity, μ_0 the permeability of free space and Δ_0 the superconducting gap at $T = 0$ K. For our films λ is estimated to vary between 350 to 480 nm depending on the film thickness and measured material parameters.

In thin films, the reduction in Cooper pair density causes the inertial mass of the charge carriers to become important at microwave frequencies, which results in an additional series inductance, or kinetic inductance L_k. We estimate the kinetic inductance fraction $\alpha = L_k/(L_g+L_k)$ for each film by comparing the measured resonator frequency to one predicted by an analytical model, where L_g is the inductance due to the resonator geometry. Thinner films showed an increased kinetic inductance fraction as expected for a strongly disordered superconductor such as NbTiN (Fig. 4.2 b). While thinner films should increase the magnetic field compatibility, as α approaches 1 the increase in inductance adds additional challenges for impedance matching and frequency targeting. At the same time, frequency targeting of the resonators becomes increasingly difficult due to the sensitivity of L_k with respect to material parameters that become less consistent in thinner films [47].

At B = 0 T, the transmission spectra of each sample shows a series of resonances, each corresponding to a frequency multiplexed resonator. All films display stable resonances with Q_i varying between 10^4 and 10^5. Example resonances for t = 300 nm and 22 nm films are shown in Fig. 4.2 c and e respectively.

A magnetic field $B_\parallel$ is then applied parallel to the film using the vector magnet, using the response of the resonator itself to align the magnetic field (see Supplementary Information for alignment details). This results in the different films displaying markedly different behavior. Measurements at $B_\parallel > 100$ mT on devices with film thicknesses of $t = 100$ nm and 300 nm (for $t = 300$ nm see Fig. 4.2 d) show a homogeneous broadening of their resonances, a reduction in their resonance frequency and reduction in Q_i. This is consistent with increased intrinsic losses and increased inductance due to a high density of Abrikosov vortices. At fields above 125 mT, the reduction in Q_i and broadening are so extreme that we are unable to resolve the resonances.

In contrast, resonators with film thickness of $t = 8$ nm and 22 nm show inhomogenous broadening (for $t = 22$ nm see Fig. 4.2 f), with fluctuations of a high

4
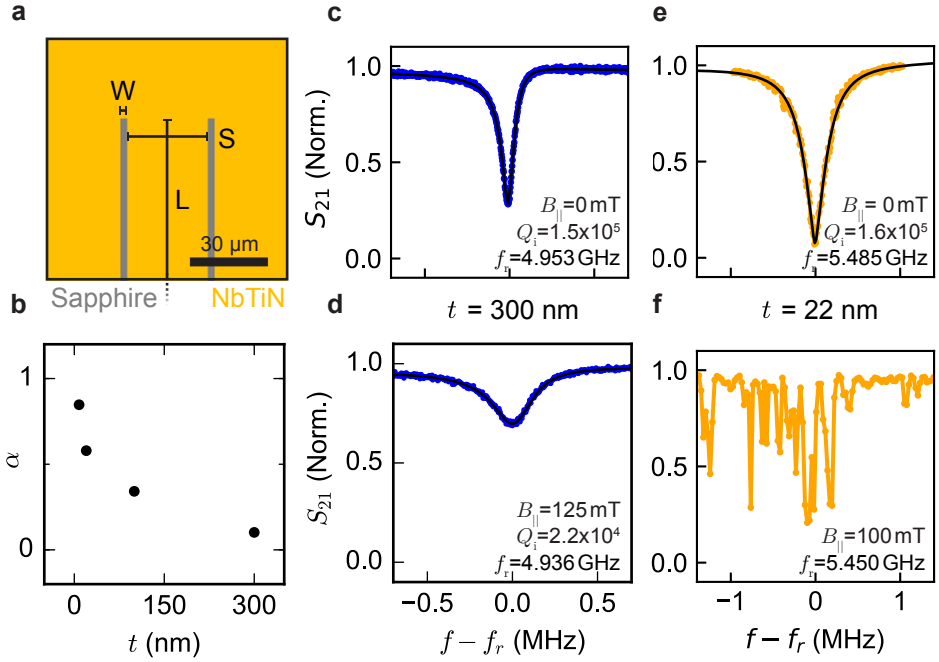
Figure 4.2: **a** Diagram showing the shorted end of a $\lambda/4$ resonator of length L with a central conductor of width S and gap W and no holes. **b** Extracted value of α for each t, showing a sharp increase in α for $t \ll \lambda$. **c,e** S_{21} versus f for resonators with $t = 300$ nm and 22 nm, showing high Q_i, stable resonances at $B = 0$ mT. **d,f** S_{21} versus f for $t = 300$ nm and 22 nm at $B_\parallel \geq 100$ mT.

Q resonance on the timescale of seconds. We attribute this behavior to a smaller number of vortices being pinned in the superconductor, with vortex depinning events occurring on the same timescale as the measurement. These depinning events may also occur more often in thinner films due to a reduced superconducting order parameter Δ_{SC} (see Supplementary Information) and increased variability in t. While the reduced vortex number is consistent with an enhancement of the critical field, we note that it is still far below the expected theoretical field enhancement of B_{c_1} for these films. We attribute this to small misalignments and local deviations in the magnetic field that suppress the critical field enhancement, resulting in a higher than expected vortex density. If resonator performance is to be protected in strong magnetic fields, the detrimental effects of these vortices must be mitigated.

4.4. Holes

4.4.1. Perpendicular field dependence

Defects in the film locally reduce Δ_{SC} in the superconductor, creating a potential well in which the energy cost required to break the superconductivity in that region is reduced, providing an additional mechanism for controlling Abrikosov vortices. As it is energetically favourable for the vortex to sit in the defect, it experiences a corresponding restoring force pinning it into the defect, minimising losses [33, 42, 48, 49]. The defects used in this experiment are holes in the superconducting film that are defined by EBL and RIE. This allows them to be patterned in the same step as the resonators and have a diameter smaller than the vortices ($\lambda > d > \xi$), allowing high hole densities ρ_h to be achieved.

We fabricated a sample from a $t = 22\,\text{nm}$ film with resonators of different ρ_h varying from 0 to $28.8\,\mu\text{m}^{-2}$ to determine the effect of holes on resonator performance. The resonators retain a constant CPW geometry and the ground plane is patterned with large square holes that trap residual local magnetic fluxes in the environment (see Supplementary Information). The holes have diameters $d = 100\,\text{nm}$ and are patterned into hexagonal arrays on the central conductor and edges of the adjacent ground planes. Unlike previous experiments with holes at the edge of the resonator [42], we leave a gap of at least $1\,\mu\text{m}$ to the film edge to avoid interfering with the bulk of the current that flows at the edges of the CPW [50]. The hole densities can be converted to a threshold 'critical field' B_{Th} (ranging between 0 and $59.69\,\text{mT}$) that when applied perpendicular to the plane of the film fills each hole with a single Abrikosov vortex. Above B_{Th} additional vortices are no longer strongly pinned by the holes but instead only weakly pinned by film defects and interstitial pinning effects.

Field-cooled measurements are performed by applying a perpendicular magnetic field $B_\perp$ to the sample above $T_c \sim 14\,\text{K}$ of the NbTiN, then cooling the sample to base temperature before performing transmission measurements to characterize the resonators. At $B = 0\,\text{T}$, all resonators are measured with $Q_i > 10^5$ (Fig. 4.3 a). Resonators with a non-zero ρ_h trap the few vortices that form due to the local magnetic environment near the CPW, enhancing Q_i. At higher ρ_h, Q_i reduces, possibly
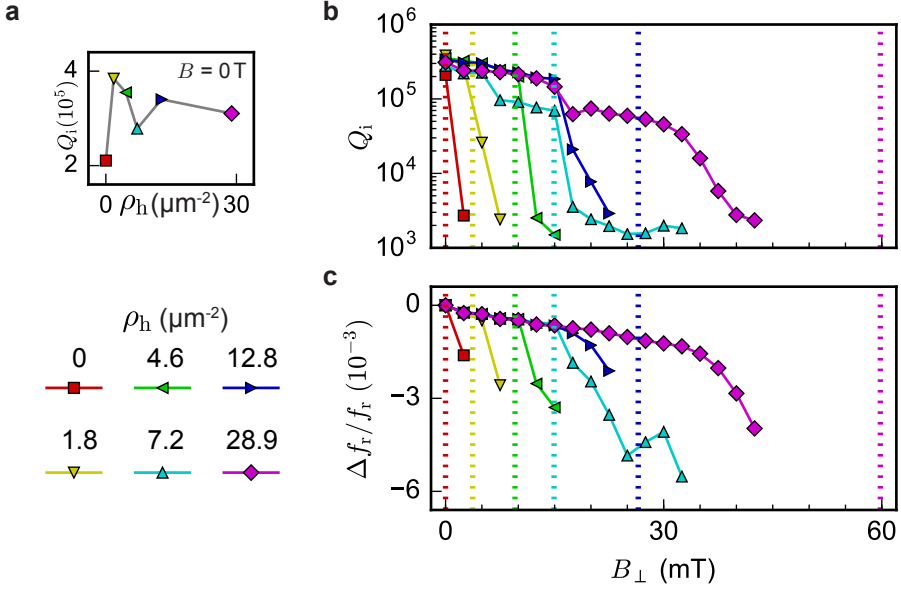
Figure 4.3: **a** Q_i versus ρ_h for field-cooled resonators at $B_\perp = 0\,$T. **b** Q_i versus $B_\perp$ for varying ρ_h. B_{Th} for each resonator is plotted with a colour matched vertical line. **c** $\Delta f_r/f_r$ versus $B_\perp$ for varying ρ_h with B_{Th} plotted as in b.

due to increased losses occurring in the larger metal-vacuum interface area [51].

The behavior of Q_i versus $B_\perp$ field is plotted in Fig. 4.3 b together with the calculated B_{Th} for each hole density. For $B < B_{Th}$, each resonator retains a high Q_i as all vortices can be trapped in holes. Once every hole is full ($B > B_{Th}$) Q_i sharply decreases, as additional vortices are then only weakly pinned and can become itinerant in the SC film, resulting in resistive losses. The same response is observed in the fractional frequency $\Delta f_r/f_r = (f_r - f_r^{B=0})/f_r$ of the resonators (Fig. 4.3 c). For $B < B_{Th}$, the magnetic field increases the rate of Cooper pair breaking, increasing L_k and resulting in a gradual reduction of f_r [46]. Once $B > B_{Th}$ the vortices are no longer pinned by the hole lattice and become itinerant, significantly increasing the inductive load on the resonator resulting in a comparatively large frequency shift.

At larger ρ_h ($\geq 12.8\,\mu m^{-2}$) the results start to deviate from the expected response. We attribute this to the vortex density approaching a regime where the vortices start to overlap, meaning that the superconductivity can no longer assumed to be homogeneous, increasing losses. Unusually, the resonator with highest ρ_h (i.e. the 'hole-iest' resonator) experiences a reduction in Q_i at $\sim 15\,$mT along with the other resonators, but retains a relatively high $Q_i \simeq 10^5$ and flat $\Delta f_r/f_r$ response until $B_\perp \simeq 35\,$mT. This behavior is consistent with a fraction of the vortices penetrating the SC film, but not being itinerant. This would result in the observed Q_i reduction while protecting the resonators f_r from the sharp reduction observed in the other resonators. This is suggestive of interstitial pinning effects that have been extensively studied previously and could be used to further increase the per-
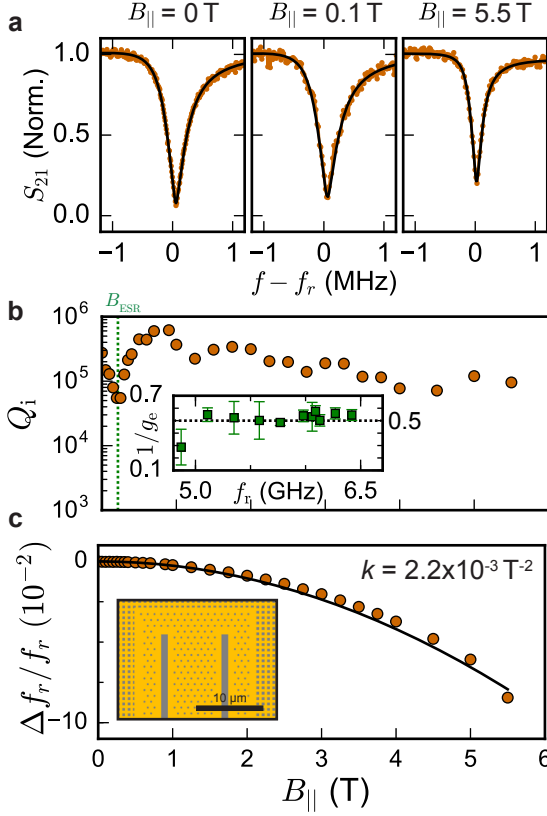
Figure 4.4: **a** S_{21} versus $f - f_r$ for a typical $t = 22$ nm resonator with holes at $B_{||} = 0$ T, 0.1 T and 5.5 T. **b** Extracted Q_i versus $B_{||}$. Inset shows the inverse of the extracted g_e-factor from Q_i minima of each resonator as a function of $B_{||}$. **c** Extracted $\Delta f_r / f_r$ versus $B_{||}$. A fit of the data with $\Delta f_r / f_r = -kB_{||}^2$ gives $k = 2.2 \times 10^{-3}$ T^{-2}. Inset is a diagram showing the distribution of holes around the CPW.

pendicular field compatibility of these resonators [52–54].

4.4.2. Parallel field dependence

To demonstrate that thin films and a low density of holes can be used to increase the resilience of resonators to strong parallel magnetic fields, a sample with 12 resonators of varying CPW dimensions but constant hole density were fabricated from $t = 22$ nm films. The holes are 300 nm in diameter and arranged in hexagonal lattice around the CPW with a density of $\rho_h = 1.2$ µm^{-2} (Fig. 4.4 c inset). The device is then cooled at $B = 0$ T and S_{21} measurements performed to determine the Q_i of all 12 resonators as a function of $B_{||}$, with $B_{||}$ applied as in Sec. 4.3 using the response of the resonator for field alignment.

S_{21} versus $f - f_r$ for an example resonance at $B_{||} = 0$ T, 0.1 T and 5.5 T (Fig. 4.4 a) shows a stable, high Q_i peak at all fields, a key requirement for their effective use

Figure 4.5: **a** Optical microscope image **b** scanning electron microscope image and **c** 3D diagram of the hybrid device. At each end of the cavity, a sin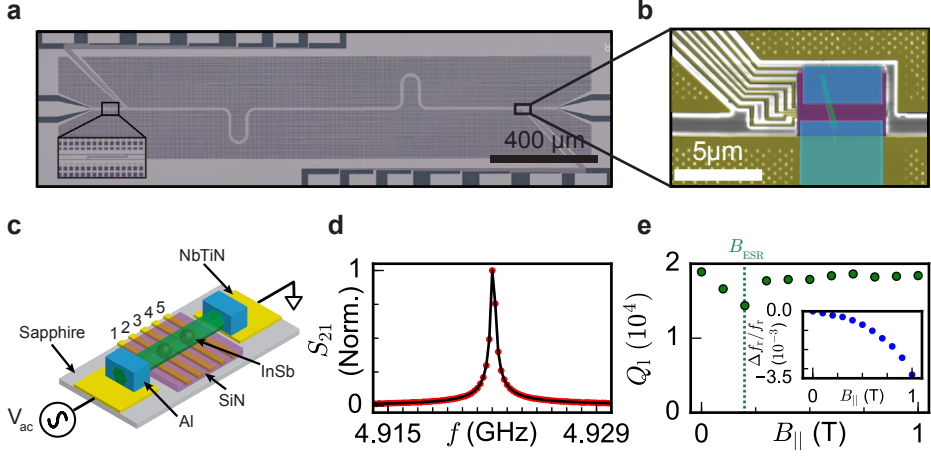gle InSb nanowire is deposited on local fine gates. Ti/Al is used to contact the nanowire to the resonator's central conductor and ground. Local fine gates (1-5) are used to electrostatically define the DQD. Coupling capacitors control the photon lifetime in the cavity. **d** S_{21} versus f shows a single resonance at $f = 4.922$ GHz with $Q_l = 1.8 \times 10^4$. **e** Q_l as a function of $B_\parallel$ demonstrates the resonator is unaffected by strong magnetic fields. Inset is $\Delta f_r / f_r$ versus $B_\parallel$ displaying a small parabolic frequency shift.

in superconducting circuits. Fitting the resonator response to extract Q_i versus $B_\parallel$ (Fig. 4.4 b) reveals that $Q_i \sim 10^5$ can be retained up to $B_\parallel = 5.5$ T. A dip in Q_i is observed at $B_{ESR} \sim 200$ mT and is attributed to coupling to an electron spin resonance that increases losses in the cavity. This feature is observed in all resonators, with the frequency dependence corresponding to paramagnetic impurities with a Landé g-factor of ~ 2 (Fig. 4.4 b inset) as observed in [46].

As $B_\parallel$ is increased, the resonator f_r reduces (Fig. 4.4 c) due to the increased rate of Cooper pair breaking from the applied $B_\parallel$. It can be modelled as a parabolic decrease in $B_\parallel$ as $\Delta f_r / f_r = -k B_\parallel^2$, with $k = \frac{\pi}{48} [t^2 e^2 D / \hbar k_B T_c]$ dependent on t, T_c and D the electron diffusion constant in NbTiN. With all other parameters known, we determine $D = 0.79$ cm^2 s^{-1}, consistent with previous results [46]. The field resilience up to $B_\parallel \simeq 6$ T is observed in all resonators, implying that this is a generic recipe by which field resilient SC CPW resonators can be fabricated (see the Supplementary Information for measurements of all 12 resonators).

4.5. Charge readout of a hybrid InSb nanowire device at 1 T

Double quantum dots (DQDs) and high quality factor SC CPW resonators in combination form a superconductor-semiconductor 'hybrid' system allowing for the high bandwidth sensing of DQD charge configurations in a variety of material systems using techniques from circuit quantum electrodynamics (cQED) [14, 55–57].

More exotic hybrid systems such as spin qubits [13, 25], Majorana box qubits [28] and spin-transmon hybrids also require the application of strong parallel magnetic fields, a condition that to date has proven challenging for traditional SC CPW resonators. To demonstrate the importance of our field resilient patterned SC CPW for hybrid systems we integrate a pair of InSb nanowires into a $\lambda/2$ resonator and perform fast charge readout of DQDs at a magnetic field of $B_\parallel = 1$ T.

The $\lambda/2$ resonator, holes and the electrostatic gates required for forming the DQDs are formed in a single lithography step followed by SF_6/O_2 reactive ion etch of a 20 nm NbTiN film (see Fig. 4.5 a). The holes ($d = 150$ nm) are arranged in a hexagonal lattice with a density of $\rho_h = 3.2\,\mu m^{-2}$. At each end of the resonator at the electric field maxima, we deposit a single nanowire on top of a set of 5 fine gates (Fig. 4.5 (a-c)). A 30 nm layer of sputtered SiN_x electrically isolates the nanowire from the underlying gates. Following sulfur etching to remove the surface oxide from the InSb nanowire [58], 150 nm Ti/Al contacts are evaporated on each end of the nanowire to define the electrical potential in the nanowire. One contact is connected directly to the central conductor of the resonator, and the other end directly to the ground plane to enhance the coupling between the DQD and the cavity's electric field [13]. By applying voltages to the electrostatic gates, we can control the electron occupation in the nanowire, either turning the device off, or tuning it into a single or double quantum dot configuration.

Transmission measurements of the resonator with each nanowire depleted show a single resonance at frequency $f_r = 4.922$ GHz with loaded quality factor $Q_l \simeq 1.8 \times 10^5$ (Fig. 4.5 d). The resonator is in the over-coupled regime, with the coupling capacitances of the input and output ports controlling the photon lifetime in the cavity.

The magnetic field $B_\parallel$ is applied parallel to the plane of the resonator (Fig. 4.5 e), using the response of the resonator itself to align the field (as described in Sec. 4.3). Similarly to the $\lambda/4$ resonators, f_r reduces parabolically in $B_\parallel$ due to the increased L_k and Q_l experiences a decrease at $B_{ESR} \simeq 200$ mT, corresponding to paramagnetic impurities coupling to the cavity via electron spin resonance (Fig. 4.5 e and inset).

Once the external magnetic field is aligned and has reached $B_\parallel = 1$ T, the resonator can be used for tuning the charge occupancy in each of the nanowire DQDs without DC transport. The DQDs are formed by monitoring the microwave response of the resonator and using an applied voltage on outer gates 1 and 5 (Fig. 4.5 c) to define a single QD, then using the middle gate 3 to form a DQD. Electron transitions between the dot and lead are a dissipative process that cause a reduction in Q_l, which can be observed as a reduction in the S_{21} peak amplitude. Additionally, as the inter-dot tunnel coupling rate of the electrons t_c approaches f_r, the transition coherently couples to the electric field in the cavity via a Jaynes-Cummings type interaction. This results in a repulsion of the resonator, shifting the resonator frequency and changing the measured phase ϕ [55].

Monitoring the amplitude and phase fluctuations as the plunger gates are varied allows the dot-lead and inter-dot transitions to be identified and the charge stability diagrams for each of the DQDs to be measured at $B_\parallel = 1$ T (Fig. 4.6). For
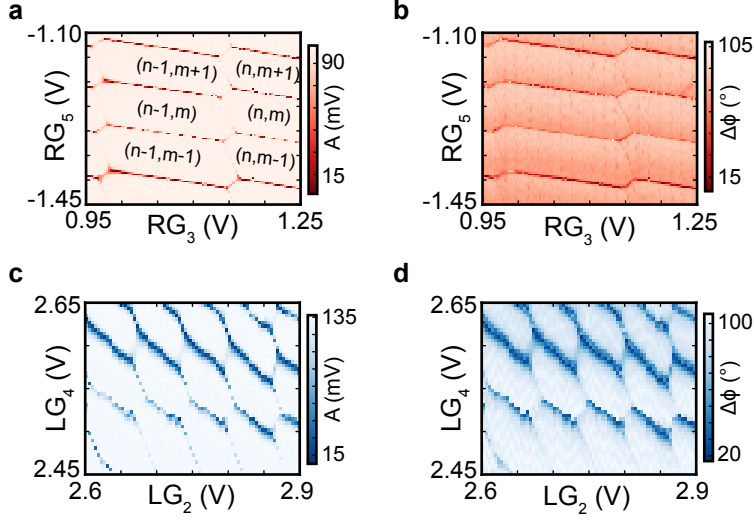
Figure 4.6: Measuring S_{21} at f_r at $B = 1\,T$ as V on the fine gates is varied generates charge stability diagrams of the right **a,b** and left **c,d** nanowire DQDs. The electron occupation n (m) of the left (right) QD can be modified by tuning the gate voltages.

the right DQD, gates 2, 4 and 5 are used to define the dots while 3 and 5 control the electron occupancy (Fig. 4.6 (a,b)). In the left DQD the electrical confinement is defined by 1, 3, 5, and the charge occupancy controlled by 2 and 4 (Fig. 4.6 (c,d)). For each DQD, the charge occupancy in the left (right) dot is denoted with n (m).

The measurements were performed at $B_\parallel = 1\,T$, an order of magnitude improvement over previous studies [13, 26], and a magnetic field of relevance for numerous topological quantum computing proposals [27, 28] and the investigation of mesoscopic phenomena in hybrid systems under strong magnetic fields [18].

4.6. Conclusion

These results indicate that by controlling vortex dynamics in SC CPW resonators a $Q_i \simeq 10^5$ can be retained in a perpendicular magnetic field of $B_\perp \simeq 20\,mT$. When combined with film thickness reduction to enhance B_{c_1}, we establish a reliable fabrication recipe to create SC CPW resonators that can retain a high $Q_i \sim 10^5$ in strong parallel magnetic fields up to $B_\parallel \simeq 6\,T$. We demonstrate the importance of these techniques for hybrid systems by coupling a superconducting resonator to DQDs electrostatically defined in InSb nanowires. Using high frequency measurement techniques we demonstrate device operation and determine the charge stability diagrams of two DQDs at $B_\parallel = 1\,T$, a magnetic field of relevance for mesoscopic physics studies and semiconducting, topological and hybrid quantum computing schemes.

4.7. Supplementary material

4.7.1. Device parameters

A large number of devices were fabricated and measured in the creation of this manuscript. Fig. 4.7 contains the important physical parameters for all resonators used in this paper.

4.7.2. Fitting Procedure

To accurately extract the Q_i of our $\lambda/4$ resonators at single photon levels we follow the fitting procedure detailed in [35, 59]. The complex transmission parameter S_{21} is fitted with the following formula:

$$S_{21} = A\left(1 + \alpha \frac{f - f_r}{f_r}\right)\left(1 - \frac{\frac{Q_l}{|Q_e|}e^{i\theta}}{1 + 2iQ_l\frac{f-f_r}{f_r}}\right)e^{i\phi_e f + \phi_0} \tag{4.1}$$

Where A is the amplitude of the bare feedline transmission in the absence of a resonance, α is a background slope parameter to account for non-uniform background transmission, f is the probe frequency, f_r is the resonance frequency, Q_l is the loaded quality factor, Q_e is a complex-valued external quality factor related to Q_c via $1/Q_c = Re(1/Q_e)$ and ϕ_0 and ϕ_e compensate for signal propagation delays to and from the sample.

For the $\lambda/2$ resonators without a calibration of the baseline transmission Q_i cannot be accurately extracted. In this case we extract only Q_l by fitting S_{21} using:

$$S_{21} = A\frac{\delta f}{(f - f_r)^2 + (\delta f^2/4)} \tag{4.2}$$

Where A is the amplitude of the Lorentzian, δf is the full width half maximum of the resonance, f is the probe frequency and f_r is the resonance frequency. The quality factor is defined to be $Q_l = f_r/\delta f$.

4.7.3. Calculation of kinetic inductance fraction

The kinetic inductance fraction α is used to represent how strongly the kinetic inductance L_k contributes to the total waveguide inductance L_t, given by $\alpha = L_k/L_t$. To determine α we first consider how the resonance frequency f_r is set in a distributed element LC resonator model:

$$f_r = \frac{1}{4l\sqrt{LC}} \tag{4.3}$$

Where f_r is the resonance frequency, l is the resonator length, C is the capacitance per unit length and L is the inductance per unit length of the resonator. The total inductance L_t consists of a contribution from the kinetic inductance L_k and a contribution from the geometry L_g summing to give $L_t = L_k + L_g$. We use geometric models to estimate C and L_g of the CPW resonator [60]:

$$L_g = \frac{\mu_0}{4}\frac{K(k')}{K(k)}l \tag{4.4}$$

4

Film	t (nm)	Device	Resonator	Type	S (μm)	W (μm)	L (μm)	f_r (GHz)	ρ_h (μm⁻¹)	B_Th (mT)
1	8	1	1	$\lambda/4$	42	0.4	2124	6.037	0	0
2	22	2	1	$\lambda/4$	32	2.5	3780	5.485	0	0
3	100	3	1	$\lambda/4$	15	4	4443	5.927	0	0
4	300	4	1	$\lambda/4$	11.5	4	5935	4.953	0	0
2	22	5	1	$\lambda/4$	4	10	1969	7.994	0	0
2	22	5	2	$\lambda/4$	4	10	2652	5.854	1.8	3.7
2	22	5	3	$\lambda/4$	4	10	2542	5.995	4.6	9.6
2	22	5	4	$\lambda/4$	4	10	2441	6.109	7.2	14.9
2	22	5	5	$\lambda/4$	4	10	2104	6.786	12.8	26.5
2	22	5	6	$\lambda/4$	4	10	2034	5.971	28.9	59.7
2	22	6	1	$\lambda/4$	8	1	2760	4.873	1.2	2.5
2	22	6	2	$\lambda/4$	8	5	3180	5.106	1.2	2.5
2	22	6	3	$\lambda/4$	8	10	3277	5.347	1.2	2.5
2	22	6	4	$\lambda/4$	4	1	2038	5.587	1.2	2.5
2	22	6	5	$\lambda/4$	4	5	2411	5.773	1.2	2.5
2	22	6	6	$\lambda/4$	4	10	2503	5.98	1.2	2.5
2	22	6	7	$\lambda/4$	2	1	1832	5.984	1.2	2.5
2	22	6	8	$\lambda/4$	2	5	1904	6.063	1.2	2.5
2	22	6	9	$\lambda/4$	2	10	1534	6.091	1.2	2.5
2	22	6	10	$\lambda/4$	1	1	1172	6.133	1.2	2.5
2	22	6	11	$\lambda/4$	1	5	1391	6.271	1.2	2.5
2	22	6	12	$\lambda/4$	1	10	1443	6.427	1.2	2.5
5	20	7	1	$\lambda/2$	10	1.5	6650	4.992	3.6	6.6
2	22	8	1	$\lambda/4$	16	0.4	3335	3.529	0	0
2	22	8	2	$\lambda/4$	8	0.4	2914	3.956	0	0
2	22	8	3	$\lambda/4$	4	0.4	2685	3.974	0	0
2	22	8	4	$\lambda/4$	2	0.4	2453	4.419	0	0
2	22	8	5	$\lambda/4$	16	0.4	2732	4.498	0	0
2	22	8	6	$\lambda/4$	8	0.4	2553	4.534	0	0
2	22	8	7	$\lambda/4$	4	0.4	2373	4.534	0	0
2	22	8	8	$\lambda/4$	4	0.4	2373	5.054	0	0
2	22	8	9	$\lambda/4$	2	0.4	2188	5.567	0	0

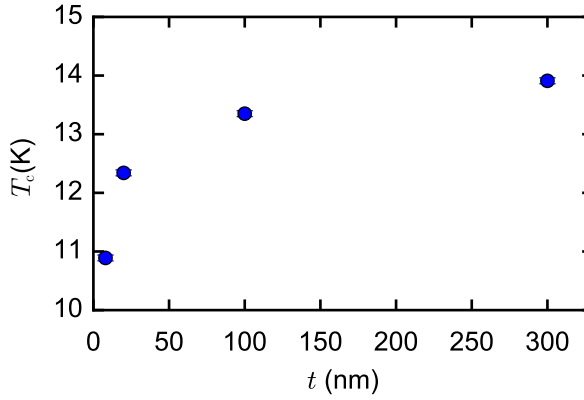Figure 4.7: Table of important physical parameters for all devices.

Figure 4.8: Critical temperature T_c of NbTiN films as a function of t.

$$C = 4\epsilon_0\epsilon_{\text{eff}}\frac{K(k)}{K(k')}l \tag{4.5}$$

Where μ_0 is the permeability of free space, ϵ_0 is the permittivity of free space, ϵ_{eff} is the effective dielectric constant of the CPW, K is the complete elliptic integral of the first kind and k is the fraction of the central conductor to the total CPW width. $k = S/(S + 2W)$ where S is the width of the central conductor and W is the width of the gap between the central conductor and the ground plane.

Rearranging to extract L_k:

$$L_k = \frac{1}{16f_r^2l^2C} - L_g \tag{4.6}$$

Allowing α to be defined as:

$$\alpha = \frac{1 - 16f_r^2l^2CL_g}{1} \tag{4.7}$$

4.7.4. Superconducting critical temperature of NbTiN films

Prior to fabricating devices, the superconducting critical temperature (T_c) of each film was measured. Thicknesses t ranged from 8 nm to 300 nm. We found T_c to monotonically increase as a function of the thickness reaching a maximum for $t = 300$ nm (Fig. 4.8). As t approaches the superconducting coherence length ξ of the material, T_c is strongly reduced. From this we infer that the superconducting gap Δ is also reduced.

4.8. Holey ground plane

In addition to an array of small holes that pin vortices around the CPW of resonators in devices 5, 6 and 7, the ground plane of these devices were also covered in large
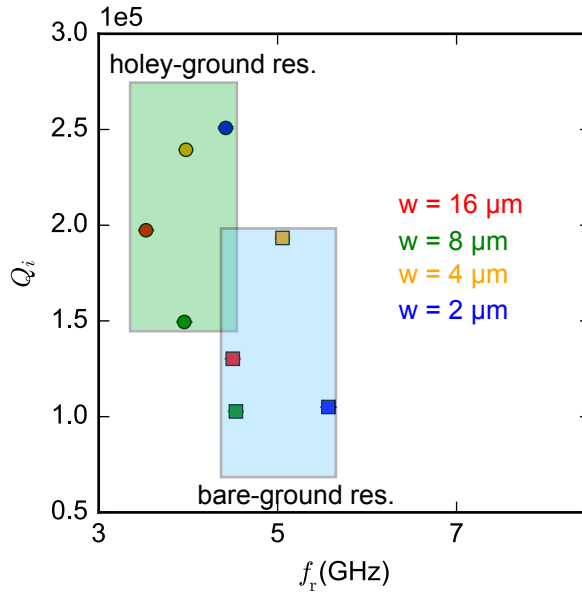
4

Figure 4.9: Role of the holey ground at $B = 0\,\text{T}$: Q_i as a function of resonant frequency with different colors for varying central conductor widths (S) in device 8. The gap (W) of all resonators is $0.4\,\mu\text{m}$. Scatter points in the transparent green (blue) box are for holey-ground (bare-ground) resonators.
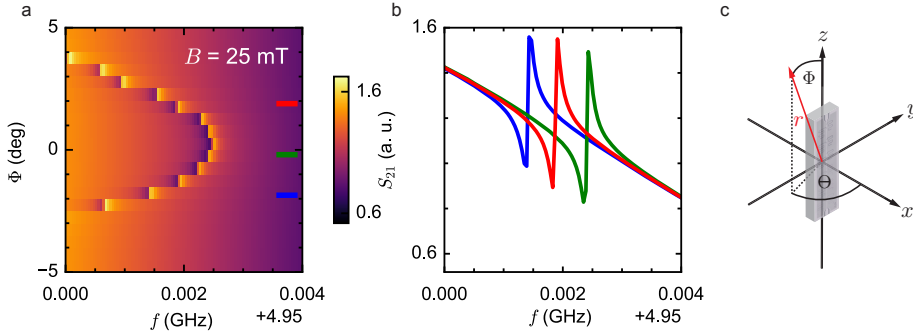
Figure 4.10: Field alignment procedure at $B = 25$ mT: a shift of the f_r as a function of Φ for resonator 1 in device 4 ($t = 300$ nm), where Φ is the spherical angle with respect to the plane of the film. b Three representative linecuts. In this case, the optimal Φ is -0.3 deg. c Coordinate system used throughout the paper for each device. At $\Theta = 0$ the angle Φ is only relative to the plane of the film.

holes that were designed to trap residual magnetic fluxes that occur in the laboratory environment when (nominally) at $B = 0$ T. To test what effect, if any, this had on the Q_i of resonators, we fabricated a device ($t = 22$ nm) hosting 8 resonators multiplexed to a common feedline. Half of these resonators were patterned with a holey ground plane and half with a bare ground plane with no holes. In this device the holey ground consists of etched squares 1 μm × 1 μm separated by superconducting strips 1 μm wide. The resonator geometries were varied by modifying the width of the central conductor (Table 4.7, device 8, resonators 1 to 8), and contained no holes around the CPW.

The device was cooled down to base temperature 3 times. Resonators on holy ground were stable, whereas those on bare ground exhibited small fluctuations in f_r, giving distorted line shapes. Upon application of a small parallel magnetic field $B_\parallel \simeq 0.1$ mT all resonators were found to become unstable, demonstrating the importance of holes around the CPW for preserving the resonator's performance in parallel magnetic fields. The Q_is of resonators with the same W at $B = 0$ T are higher if they are surrounded by holey ground (see Fig. 4.9). To fully validate this observation a more detailed study is required. Additionally the f_r of each resonator without holey ground was found to vary significantly on each cool down, providing evidence that a small number of vortices were trapped around the CPW of each resonator.

4.8.1. Field Alignment Procedure

An accurate alignment of the magnetic field direction with respect to the plane of the film was required to minimise the nucleation of vortices in the superconductor. After setting the field magnitude to the required value, the spherical angle

ϕ was fine tuned and the response of the resonant frequency monitored. As the perpendicular component of the magnetic field causes the frequency to decrease faster than the parallel one, we optimised the angle for in-plane measurements to maximise the frequency and minimise the number of vortices present in the device (Fig. 4.10).

4.8.2. Resonators with holes in parallel magnetic field

Here we report the response of the 11 other resonators on device 6 (See Tab. 4.7) with holes studied in parallel magnetic field. These are patterned on a $t = 22$ nm thick film with a hole density of $\rho_h = 1.2\,\mu m^{-2}$. Each hole has a diameter of 300 nm. The 12 resonators were designed to have different geometries; in particular, we varied the width of the central conductor (S) and the gap (W) between the central conductor and the ground plane. In the main text (see Fig. 4) we report the response of resonator 1. Our measurements did not indicate that the geometry plays an important role in protecting the resonators from nucleation of vortices. In fact we found that - with holes - both the frequency shift and the internal quality factor of all resonators have similar trend in parallel magnetic field (Fig. 4.11).
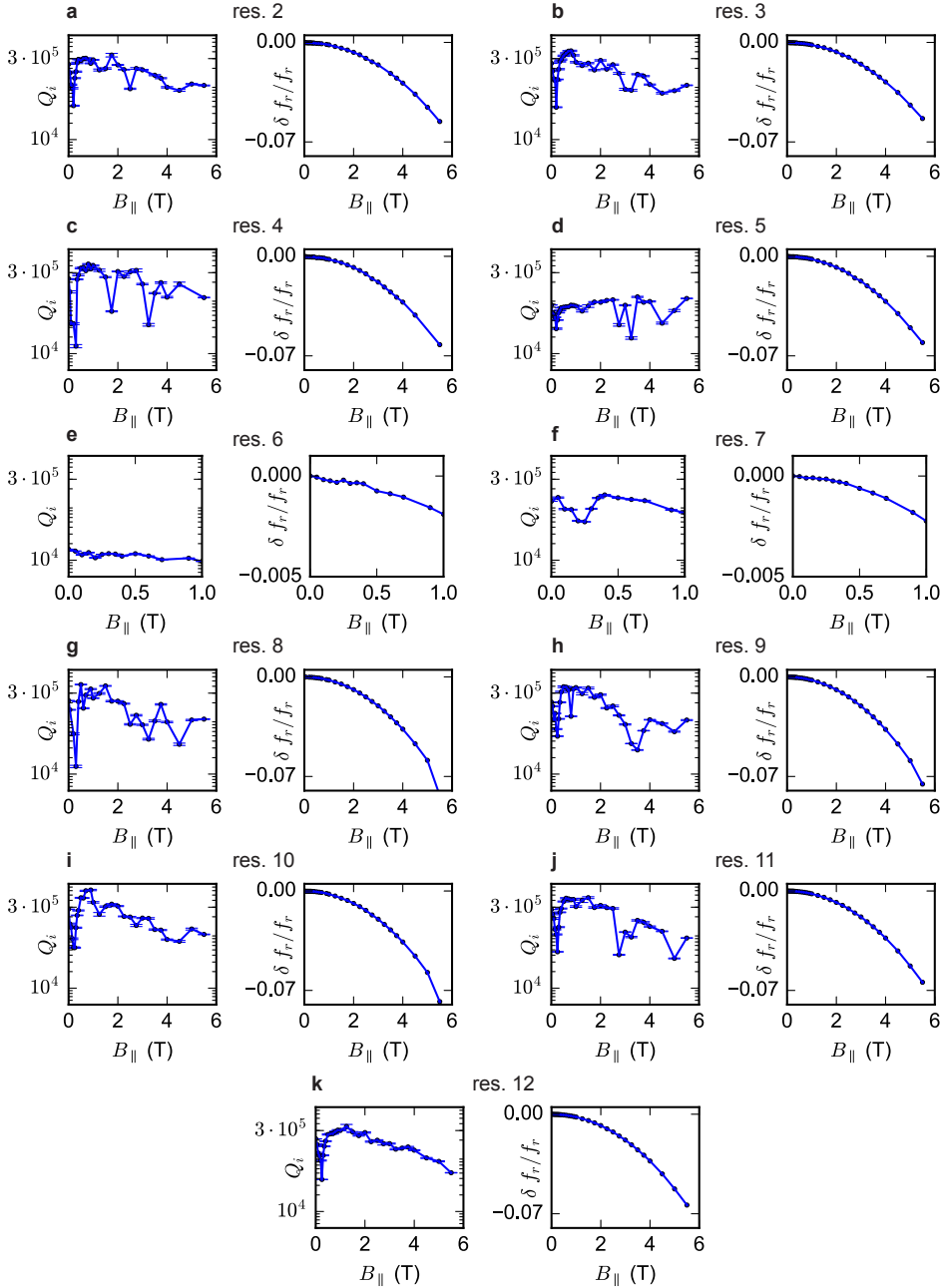
Figure 4.11: Resonators with holes in parallel magnetic field: from a to (k) the relative frequency shift $(\delta f_r/f_r(B))$ and $Q_i(B)$ for resonators 2 to 12 in device 6. Resonators 6 and 7 could not be investigated above $B = 1$ T as their f_r overlapped.

References

[1] Castellanos-Beltran, M. A. & Lehnert, K. W. Widely tunable parametric amplifier based on a superconducting quantum interference device array resonator. *Applied Physics Letters* **91**, 083509 (2007).

[2] Tholén, E. A. *et al.* Nonlinearities and parametric amplification in superconducting coplanar waveguide resonators. *Applied Physics Letters* **90**, 253509 (2007).

[3] Mazin, B. A., Day, P. K., LeDuc, H. G., Vayonakis, A. & Zmuidzinas, J. Superconducting kinetic inductance photon detectors. vol. 4849, 283 (International Society for Optics and Photonics, 2002).

[4] Day, P. K., LeDuc, H. G., Mazin, B. A., Vayonakis, A. & Zmuidzinas, J. A broadband superconducting detector suitable for use in large arrays. *Nature* **425**, 817–821 (2003).

[5] Vardulakis, G., Withington, S., Goldie, D. J. & Glowacka, D. M. Superconducting kinetic inductance detectors for astrophysics. *Measurement Science and Technology* **19**, 015509 (2008).

[6] Hattermann, H. *et al.* Coupling ultracold atoms to a superconducting coplanar waveguide resonator. *Nature Communications* **8**, 2254 (2017).

[7] Kubo, Y. *et al.* Strong coupling of a spin ensemble to a superconducting resonator. *Physical Review Letters* **105**, 140502 (2010).

[8] Amsüss, R. *et al.* Cavity QED with magnetically coupled collective spin states. *Physical Review Letters* **107**, 060502 (2011).

[9] Ranjan, V. *et al.* Probing dynamics of an electron-spin ensemble via a superconducting resonator. *Physical Review Letters* **110**, 067004 (2013).

[10] Regal, C. A., Teufel, J. D. & Lehnert, K. W. Measuring nanomechanical motion with a microwave cavity interferometer. *Nature Physics* **4**, 555–560 (2008).

[11] Teufel, J. D., Regal, C. A. & Lehnert, K. W. Prospects for cooling nanomechanical motion by coupling to a superconducting microwave resonator. *New Journal of Physics* **10**, 095002 (2008).

[12] Burkard, G. & Imamoglu, A. Ultra-long-distance interaction between spin qubits. *Physical Review B* **74**, 041307 (2006).

[13] Petersson, K. D. *et al.* Circuit quantum electrodynamics with a spin qubit. *Nature* **490**, 380–383 (2012).

[14] Viennot, J. J., Dartiailh, M. C., Cottet, A. & Kontos, T. Coherent coupling of a single spin to microwave cavity photons. *Science* **349**, 408–411 (2015).

4

[15] Liu, Y. Y. *et al.* Semiconductor double quantum dot micromaser. *Science* **347**, 285–287 (2015).

[16] De Lange, G. *et al.* Realization of microwave quantum circuits using hybrid superconducting-semiconducting nanowire Josephson elements. *Physical Review Letters* **115**, 127002 (2015).

[17] Larsen, T. W. *et al.* Semiconductor-nanowire-based superconducting qubit. *Physical Review Letters* **115**, 127001 (2015).

[18] Kroll, J. G. *et al.* Magnetic field compatible circuit quantum electrodynamics with graphene Josephson junctions. *Nature Communications* **9**, 4615 (2018).

[19] Blais, A., Huang, R. S., Wallraff, A., Girvin, S. M. & Schoelkopf, R. J. Cavity quantum electrodynamics for superconducting electrical circuits: An architecture for quantum computation. *Physical Review A* **69**, 062320 (2004).

[20] Wallraff, A. *et al.* Strong coupling of a single photon to a superconducting qubit using circuit quantum electrodynamics. *Nature* **431**, 162–167 (2004).

[21] Wallraff, A. *et al.* Approaching unit visibility for control of a superconducting qubit with dispersive readout. *Physical Review Letters* **95**, 060501 (2005).

[22] Majer, J. *et al.* Coupling superconducting qubits via a cavity bus. *Nature* **449**, 443–447 (2007).

[23] Stockklauser, A. *et al.* Strong coupling cavity QED with gate-defined double quantum dots enabled by a high impedance resonator. *Physical Review X* **7**, 011030 (2017).

[24] Landig, A. J. *et al.* Coherent spin-qubit photon coupling. *Nature* **560**, 179–184 (2017).

[25] Mi, X. *et al.* A coherent spin-photon interface in silicon. *Nature* **555**, 599–603 (2018).

[26] Samkharadze, N. *et al.* Strong spin-photon coupling in silicon. *Science* **359**, 1123–1127 (2018).

[27] Hyart, T. *et al.* Flux-controlled quantum computation with Majorana fermions. *Physical Review B* **88**, 035121 (2013).

[28] Plugge, S., Rasmussen, A., Egger, R. & Flensberg, K. Majorana box qubits. *New Journal of Physics* **19**, 012001 (2017).

[29] Koch, J. *et al.* Charge-insensitive qubit design derived from the Cooper pair box. *Physical Review A* **76**, 042319 (2007).

[30] Harvey, S. P. *et al.* Coupling two spin qubits with a high-impedance resonator. *Physical Review B* **97**, 235409 (2018).

4

[31] Gao, J. *et al.* Experimental evidence for a surface distribution of two-level systems in superconducting lithographed microwave resonators. *Applied Physics Letters* **92**, 152505 (2008).

[32] Barends, R. *et al.* Minimizing quasiparticle generation from stray infrared light in superconducting quantum circuits. *Applied Physics Letters* **99**, 113507 (2011).

[33] Song, C. *Microwave Properties of Vortices in Superconducting Resonators*. Ph.D. thesis (2011).

[34] Megrant, A. *et al.* Planar superconducting resonators with internal quality factors above one million. *Applied Physics Letters* **100**, 113510 (2012).

[35] Bruno, A. *et al.* Reducing intrinsic loss in superconducting resonators by surface treatment and deep etching of silicon substrates. *Applied Physics Letters* **106**, 182601 (2015).

[36] Calado, V. E. *et al.* Ballistic Josephson junctions in edge-contacted graphene. *Nature Nanotechnology* **10**, 761–764 (2015). 1501.06817.

[37] Van Woerkom, D. J., Geresdi, A. & Kouwenhoven, L. P. One minute parity lifetime of a NbTiN Cooper-pair transistor: Supplementary Information. *Nature Physics* **11**, 547–550 (2015).

[38] Vissers, M. R. *et al.* Low loss superconducting titanium nitride coplanar waveguide resonators. *Applied Physics Letters* **97**, 232509 (2010).

[39] Singh, V., Schneider, B. H., Bosman, S. J., Merkx, E. P. J. & Steele, G. A. Molybdenum-rhenium alloy based high- Q superconducting microwave resonators. *Applied Physics Letters* **105**, 222601 (2014).

[40] Kwon, S. *et al.* Magnetic field dependent microwave losses in superconducting niobium microstrip resonators. *Journal of Applied Physics* **124** (2018).

[41] Ghirri, A. *et al.* YBa2Cu3O7 microwave resonators for strong collective coupling with spin ensembles. *Applied Physics Letters* **106**, 184101 (2015).

[42] Bothner, D., Gaber, T., Kemmler, M., Koelle, D. & Kleiner, R. Improving the performance of superconducting microwave resonators in magnetic fields. *Applied Physics Letters* **98**, 102504 (2011).

[43] Stan, G., Field, S. B. & Martinis, J. M. Critical Field for Complete Vortex Expulsion from Narrow Superconducting Strips. *Physical Review Letters* **92**, 097003 (2004). URL https://link.aps.org/doi/10.1103/PhysRevLett.92.097003.

[44] Kuit, K. H. *et al.* Vortex trapping and expulsion in thin-film YBa2Cu3O7δ strips. *Physical Review B* **77**, 134504 (2008).

[45] de Graaf, S. E., Danilov, A. V., Adamyan, A. & Kubatkin, S. E. A near-field scanning microwave microscope based on a superconducting resonator for low power measurements. *Review of Scientific Instruments* **84**, 023706 (2013).

[46] Samkharadze, N. *et al.* High-Kinetic-Inductance Superconducting Nanowire Resonators for Circuit QED in a Magnetic Field. *Physical Review Applied* **5**, 044004 (2016).

[47] Thoen, D. J. *et al.* Superconducting NbTin Thin Films With Highly Uniform Properties Over a 100 mm Wafer. *IEEE Transactions on Applied Superconductivity* **27**, 1–5 (2017).

[48] Nsanzineza, I. & Plourde, B. L. T. Trapping a Single Vortex and Reducing Quasiparticles in a Superconducting Resonator. *Physical Review Letters* **113**, 117002 (2014).

[49] Lee, C. S., Janko, B., Derenyi, I. & Barabasi, A. L. Reducing vortex density in superconductors using the /'ratchet effect/'. *Nature* **400**, 337–340 (1999).

[50] Bothner, D. *et al.* Magnetic hysteresis effects in superconducting coplanar microwave resonators. *Physical Review B* **86**, 014517 (2012).

[51] Woods, W. *et al.* Determining interface dielectric losses in superconducting coplanar waveguide resonators (2018). `1808.10347v1`.

[52] Latimer, M. L., Berdiyorov, G. R., Xiao, Z. L., Kwok, W. K. & Peeters, F. M. Vortex interaction enhanced saturation number and caging effect in a superconducting film with a honeycomb array of nanoscale holes. *Physical Review B* **85**, 12505 (2012).

[53] Velez, M. *et al.* Vortex lattice channeling effects in Nb films induced by anisotropic arrays of mesoscopic pinning centers. *Physical Review B* **65**, 104511 (2002).

[54] Moshchalkov, V. V. *et al.* Pinning by an antidot lattice: The problem of the optimum antidot size. *Physical Review B* **57**, 3615–3622 (1998).

[55] Frey, T. *et al.* Dipole coupling of a double quantum dot to a microwave eesonator. *Physical Review Letters* **108** (2012).

[56] Ranjan, V. *et al.* Clean carbon nanotubes coupled to superconducting impedance-matching circuits. *Nature Communications* **6**, 7165 (2015).

[57] Wang, R., Deacon, R. S., Car, D., Bakkers, E. P. A. M. & Ishibashi, K. InSb nanowire double quantum dots coupled to a superconducting microwave cavity. *Applied Physics Letters* **108**, 203502 (2016).

[58] Gül, Ö. *et al.* Hard Superconducting Gap in InSb Nanowires. *Nano Letters* **17**, 2690–2696 (2017).

4

[59] Khalil, M. S., Stoutimore, M. J., Wellstood, F. C. & Osborn, K. D. An analysis
     method for asymmetric resonator transmission applied to superconducting
     devices. *Journal of Applied Physics* **111** (2012).

[60] Barends, R. *Photon-detecting superconducting resonators* (R. Barends, 2009).

4

5

Magnetic field compatible circuit quantum electrodynamics with graphene Josephson junctions

J. G. Kroll, W. Uilhoorn, K.L. van der Enden, D. de Jong, K. Watanabe, T. Taniguchi, S. Goswami, M. C. Cassidy, L. P. Kouwenhoven

Circuit quantum electrodynamics has proven to be a powerful tool to probe meso-scopic effects in hybrid systems and is used in several quantum computing (QC) proposals that require a transmon qubit able to operate in strong magnetic fields. To address this we integrate monolayer graphene Josephson junctions into microwave frequency superconducting circuits to create graphene based transmons. Using dispersive microwave spectroscopy we resolve graphene's characteristic band dispersion and observe coherent electronic interference effects confirming the ballistic nature of our graphene Josephson junctions. We show that the monoatomic thickness of graphene renders the device insensitive to an applied magnetic field, allowing us to perform energy level spectroscopy of the circuit in a parallel magnetic field of 1 T, an order of magnitude higher than previous studies. These results establish graphene based superconducting circuits as a promising platform for QC and the study of mesoscopic quantum effects that appear in strong magnetic fields.

A superconducting transmon qubit [1] resilient to strong magnetic fields is an important component for proposed topological [2–4] and hybrid quantum computing (QC) schemes [5, 6]. A transmon qubit consists of a Josephson junction (JJ) shunted by a large capacitance, coupled to a high quality factor superconducting resonator. In conventional transmon devices, the resonator is fabricated from Al and the JJ is fabricated from an Al/AlO$_x$/Al tunnel junction [1], both of which cease operation above the critical magnetic field of bulk Al, $\sim$10 mT. Even when considering alternative type II superconductors such as NbTiN or MoRe that can sustain superconductivity beyond $B = 8$ T [7], when subjected to a strong magnetic field the superconductor will experience detrimental effects such as reduction of the superconducting gap, increased quasiparticle generation [8] and the formation of Abrikosov vortices that cause resistive losses in a microwave field. In addition to disrupting the superconductivity, magnetic flux penetrating the JJ produces electron interference effects that reduce the Josephson energy E_J and strongly suppress the transmon energy spectrum. If the transmon is to be used for fast quantum gates, fast charge-parity detection and long range quantum state transfer in QC schemes [3, 9, 10] we are compelled to consider alternatives to conventional Al based JJs. Proximitised semiconducting nanowires, acting as gate-tuneable superconductor-normal-superconductor JJs [11] have been used successfully in a variety of microwave frequency superconducting circuits, allowing for studies of Andreev bound states [12, 13], electrically tuneable transmon qubits [14, 15] and transmons that exhibit substantial field compatibility [16]. Graphene JJs are an attractive alternative as they exhibit ballistic transport, high critical currents [7, 17, 18] and the atomic thickness of the graphene junction greatly reduces flux penetration, protecting the JJ from orbital interference effects that would suppress E_J in high parallel fields. When combined with geometric techniques that protect the superconducting film, such as critical field enhancement [19] and lithographically defined vortex pinning sites [20, 21], the transmon circuit can be protected at magnetic fields relevant to these proposals, which approach and in some cases exceed 1 T [22–24].

In this work we report the integration of ballistic graphene JJs into microwave frequency superconducting circuits to create graphene based transmons. Using dispersive microwave spectroscopy we resolve the characteristic band dispersion of graphene, and observe coherent electronic interference effects that confirm the ballistic nature of our graphene JJs. We perform energy level spectroscopy at $B_\parallel = 0$ T to resolve a linewidth of $\simeq 400$ MHz. Although the large linewidths prevent coherent qubit control, we demonstrate the device is insensitive to the applied magnetic field up to $B_\parallel = 1$ T.

5.1. Methods

5.1.1. Fabrication

Two separate devices, device A and device B were used throughout the manuscript. For device fabrication, the type II superconductors NbTiN and MoRe were chosen for their high upper critical fields ($B_{c_2} > 8$ T) and their compatibility with mi-
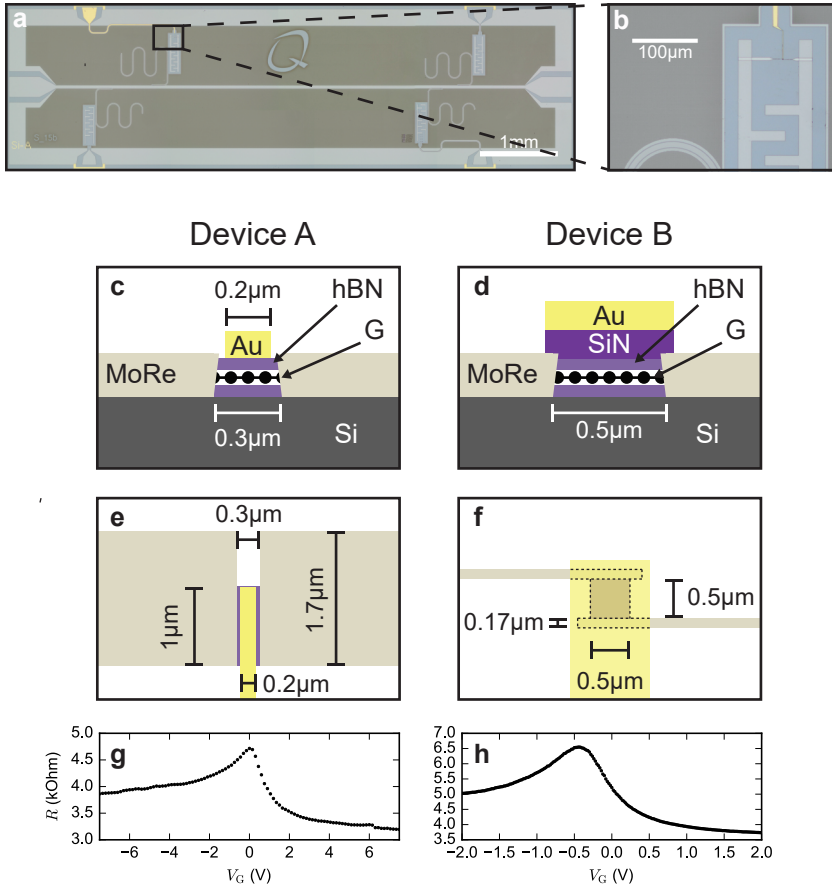
Figure 5.1: Device structure **a** Optical image showing multiple CPW resonators frequency multiplexed to a common feedline (device B). **b** Zoomed optical image of the capacitor plates that shunt the Josephson junction, with the gate, junction and contacts visible. **c** Cross sectional diagram showing the geometry of the junction in device A. It is 300 nm in length, with a gate designed to be 200 nm in width. **d** Cross sectional diagram of device B, with the SiN_x/Ti/Au gate giving full coverage of the 500 nm long junction. **e** The junction in device A is 1000 nm wide and contacted by 1700 nm wide MoRe contacts. The 200 nm wide gate can be seen to cover most, but not all of the graphene stack. **f** Device B has a 500 x 500 nm^2 junction that is contacted by thin 170 nm MoRe leads to prevent vortices from forming near the junction. The SiN_x/Ti/Au gate stack is sputtered and designed to give full coverage of the graphene junction. **g** Measurement of the two point resistance R of the contacts and junction for device A at room temperature as the gate voltage V_G is varied. The charge neutrality point can be observed at $V_G = 0$ V. **h** R measurements for device B at room temperature again showing the charge neutrality point, this time offset slightly to $V_G \simeq -0.5$ V. Upon cooling to $T = 15$ mK, the charge neutrality points were observed to shift in both devices.
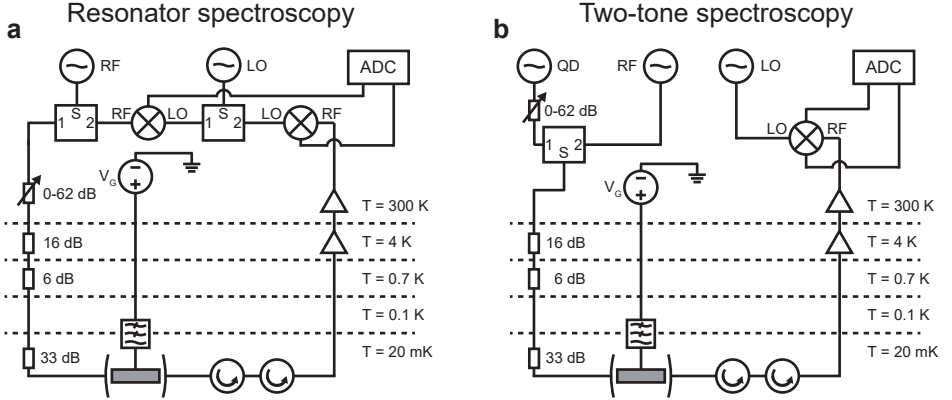
Figure 5.2: Circuit schematic of the measurement set up used to perform microwave measurements for resonator spectroscopy **a** and two tone spectroscopy **b**.

crowave frequency devices [25, 26]. Resistive losses from Abrikosov vortices at microwave frequencies are mitigated by expelling the vortices via geometric constriction [19, 27] and using artificial pinning sites to trap the vortices that cannot be excluded [20, 21]. To fabricate the devices 20 nm of NbTiN is sputtered onto intrinsic Si wafers in an Ar/N atmosphere. The resonators, feedline and transmon are reactive ion etched in an SF_6/O_2 atmosphere (Fig. 5.1a,b). In this etching step, an array of artificial pinning sites is also defined. Monolayer graphene is encapsulated between two hBN flakes ($t \simeq 15$ nm each), then deposited between pre-fabricated capacitors using a PMMA based van der Waals pickup method [7]. Contact to the graphene stack is made by etching in a CHF_3/O_2 environment, followed by sputtering MoRe ($t = 80$ nm). Device A was contacted to give a junction length of 300 nm (Fig 5.1c,e). A Ti/Au top gate is then sputtered on top of the stack. The device is then shaped in a CHF_3/O_2 plasma to be 1000 x 300 nm^2 in size. Device B was contacted to provide a junction length of 500 nm (Fig 5.1d,f). The long thin leads were geometrically restricted in two dimensions, making it less favourable for vortices to form, protecting the superconductivity of the contacts proximitising the junction. The junction is then shaped in a CHF_3/O_2 plasma to be 500 x 500 nm^2. A SiN_x/Ti/Au top gate stack is then sputtered to give full junction coverage, giving greater control of μ in the junction. A probe station was used to perform two probe resistance R measurements of the graphene junction and contact resistances at room temperature. Device A (Fig 5.1g) and device B (Fig 5.1h) both show charge neutrality points in the R vs V_G dependences, consistent with graphene junctions.

5.1.2. Characterisation

All measurements were performed in a dilution refrigerator with a base temperature of 15 mK. The samples were enclosed in a light tight copper box, and thermally anchored to the mixing chamber. The two measurement configurations used are

depicted in Fig 5.2. Two coaxial lines and one DC line were used to control the sample. The sample was connected to the DC voltage source by a line that was thermally anchored at each stage and heavily filtered at the mixing chamber by low RC, π and copper powder filters. The line used to drive the feedline input was heavily attenuated to reduce noise and thermal excitation of the cavity, allowing the single photon cavity occupancy to be reached. The output line of the feedline was connected to an isolator (Quinstar QCI-080090XM00) and circulator (Quinstar QCY-060400CM00) in series to shield the sample from thermal radiation from the HEMT amplifier (Low Noise Factory LNF-LNC4-8_C) on the 4K stage. Resonator spectroscopy of device A was performed using circuit **a** to measure the amplitude and phase response of the complex transmission S_{21} as the frequency was varied. Resonator and two-tone spectroscopy of device B was performed using circuit **b**, with a splitter used to combine the readout and excitation tones. This allows the complex S_{21} to be measured, but only at fixed resonator readout frequency otherwise only $|S_{21}|$ can be recorded.

5.2. Results

5.2.1. Dispersive Fabry-Perot oscillations

We begin by performing spectroscopy of the resonator in device A as a function of the input power P_{in} (Fig. 5.3a). Varying the resonator's photon occupation from $\langle n_{ph} \rangle \simeq 1000$ to $\langle n_{ph} \rangle = 1$ we observe a dispersive shift $\chi = f_r - f_{bare}$ in the resonator frequency f_r from the high power value f_{bare}. This occurs due to a Jaynes-Cummings type interaction between the harmonic readout resonator and the anharmonic transmon spectrum, with the anharmonicity provided by the Josephson junction [28]. The magnitude of the shift $\chi = g^2/\Delta$ depends on the transmon-resonator coupling g, and the difference $\Delta = f_r - f_t$ between f_r and the ground state to first excited state transition frequency $f_t = E_t/h \simeq \sqrt{8E_J E_C}/h$, allowing us to infer E_J from χ [1]. Studying χ as a function of gate voltage V_G reveals the characteristic band dispersion of graphene (Fig. 5.3b) and allows the voltage at the charge neutrality point (CNP) V_{CNP} to be identified. At negative $V_G - V_{CNP}$, the chemical potential μ is below the CNP and the graphene is in the p-regime where holes are the dominant charge carrier. Deep into the p-regime, the high carrier density (n_C) gives a large E_J, placing f_t above the resonator and giving χ a small negative value (Fig. 5.3b). As V_G approaches the CNP, the Dirac dispersion minimises the density of states reducing E_J and f_t to a minimum. Since $\chi = g^2/\Delta$, as Δ approaches zero, χ diverges. Once on resonance, the resonator acquires some characteristic of the qubit, significantly broadening the lineshape. Simultaneously, the critical photon number $n_{Crit} = \Delta^2/4g^2$ collapses [29], moving the measurement into the 'transitionary' regime between high and low photon number as in Fig. 5.3a, causing the anomalous lineshapes visible in Fig. 5.3c near CNP. As V_G is increased past the CNP, n_{Crit} and the lineshapes recover, with electrons becoming the dominant charge carrier and E_J increasing to a maximum as expected from removal of the n-p-n junction formed by the contacts [7]. The p-regime also experiences periodic fluctuations in E_J as a function of V_G due to coherent electron interference
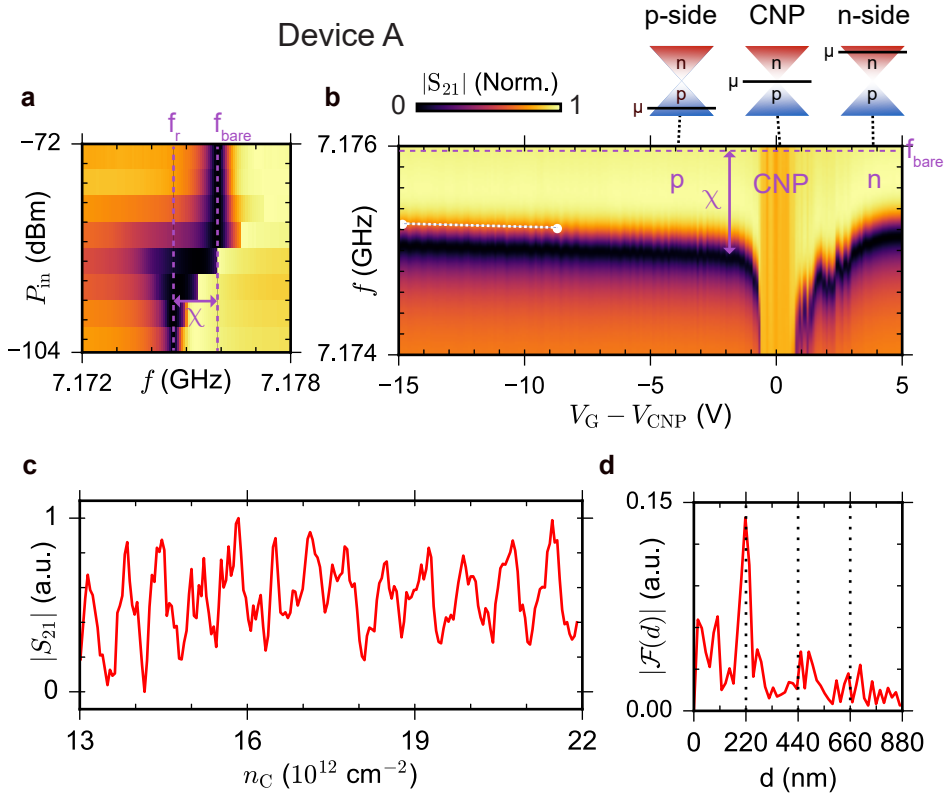
5

Figure 5.3: Resonator spectroscopy as a function of P_{in} and V_{G} **a** $|S_{21}|$ (Norm.) as a function of input frequency f and input power P_{in}. At single photon occupancy the resonator experiences a frequency shift χ due to repulsion from an energy level above the resonator (device A). **b** At single photon occupancy, $|S_{21}|$ (Norm.) is measured as f and V_{G} are varied, with the voltage at CNP ($V_{\mathrm{CNP}} = 7.8\,\mathrm{V}$) subtracted. Changing V_{G} to tune μ allows the dominant charge carriers to be varied between hole, charge neutral and electron-like regimes. In the p-regime, χ oscillates as V_{G} is varied. We extract the charge carrier density n_{c} **c** from the white linecut to generate a Fourier transform **d** that is consistent with Fabry-Perot oscillations in a cavity of $d = 220\,\mathrm{nm}$.
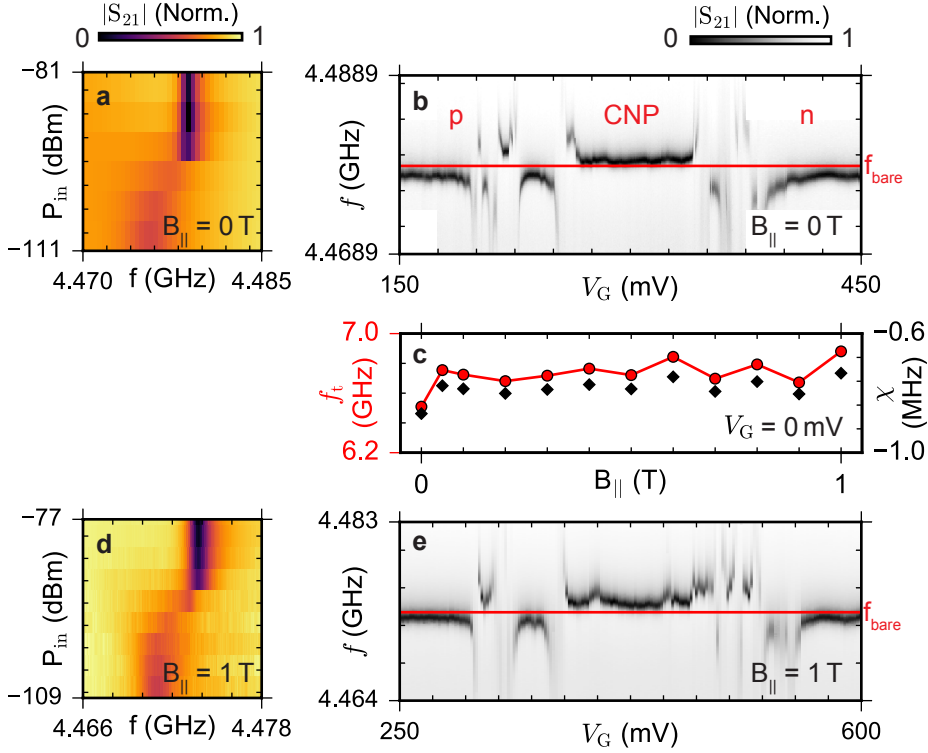
Figure 5.4: Dispersive shift as a function of V_G and $B_\parallel$ **b** At $B_\parallel = 0\,T$, $|S_{21}|$ (Norm.) versus f again shows a χ indicating the resonator is coupled to the transmon. **b** At $B_\parallel = 0\,T$, $|S_{21}|$ (Norm.) versus f and V_G shows the symmetric band dispersion of graphene with additional fluctuations we attribute to UCF. **c** f_t (red circles) extracted from χ (black diamonds) versus $B_\parallel$ at $V_G = 0\,V$, showing f_t is not significantly affected. **e** Repeating **a** and **b** at $B_\parallel = 1\,T$ confirms the graphene JJ behaves equivalently to $B_\parallel = 0\,T$. The variation observable in b and shift in V_{CNP} between a and c we attribute to slow gate drift.

effects in a Fabry-Perot cavity formed by n-p interfaces at the MoRe contacts [7]. Extracting a line trace (white line Fig. 5.3b) to study the modulation in $|S_{21}|$ with n_C (Fig. 5.3c), and performing a Fourier transform (Fig. 5.3d) gives a cavity length of 220 nm in agreement with the device dimensions. The observation of a Dirac dispersion relation in combination with coherent electron interference effects confirm the successful integration of ballistic graphene JJs into a superconducting circuit.

5.2.2. Insensitivity to applied parallel magnetic field

In device B we repeat measurements of S_{21} as a function of f and P_{In} to again reveal a power shift of the resonator coupling to the transmon (Fig. 5.4a). As we move from the p to the CNP regime, χ is seen to diverge repeatedly as f_t anti-crosses multiple times with f_r (Fig. 5.4b), most likely due to additional coherent electronic interference effects in the form of universal conductance fluctuations (UCF) [14, 30].
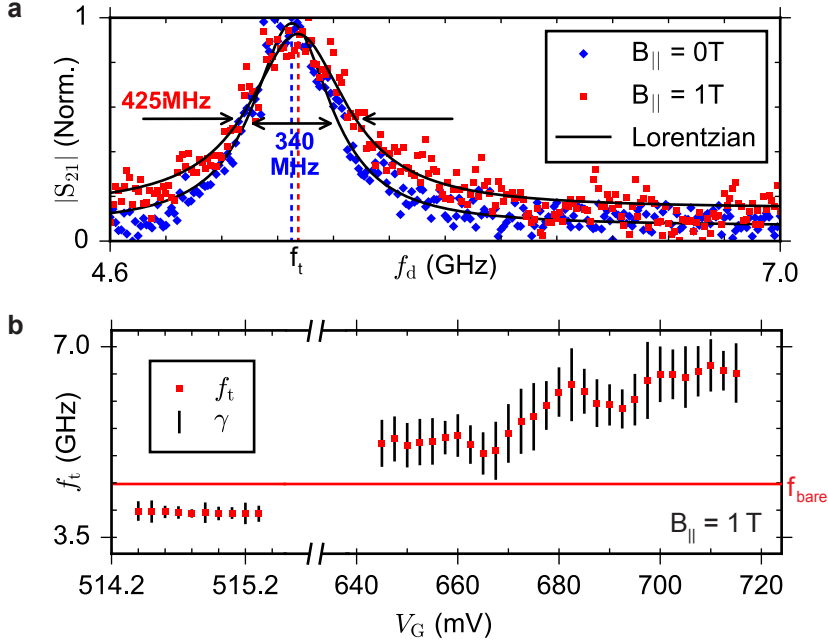
Figure 5.5: Two tone spectroscopy **a** Normalised $|S_{21}|$ at f_r as f_d is varied can be fitted to extract f_t and γ at $V_G = 0$ V. At $B_{||} = 1$ T, γ shows a 25% increase compared to $B_{||} = 0$ T. **b** At $B_{||} = 1$ T, f_t and γ are extracted as V_G is varied, demonstrating f_t can be swept over a wide frequency range. Lines bisecting each f_t are not error bars, but represent the extracted γ at each f_t.

This behaviour is repeated moving from the CNP to the n-regime, where E_J is again maximised. We demonstrate the field compatibility of the junction by applying a magnetic field $B_{||}$ along the length of the junction contacts, parallel to the plane of the film, using the resonator as a sensor for field alignment (see Sec. 4.8.1). Monitoring χ as $B_{||}$ is varied between 0 and 1 T (Fig. 5.4c) and calculating f_t (using $g = 43$ MHz, extracted from measurements in Fig. 5.5), demonstrates that χ and thus E_J are not significantly affected by the applied $B_{||}$. The small amount of variation observed is attributed to charge noise induced gate drift which was observed throughout the duration of the experiment. The presence of χ at $B_{||} = 1$ T (Fig. 5.4d) and it's dependence as a function of V_G (Fig. 5.4e) again reveals the characteristic Dirac dispersion as seen in Fig. 5.4b, with modified UCF and shifted V_{CNP} due to slow gate drift. The insensitivity of f_t to applied field and similarity of device operation at $B_{||} = 0$ T and 1 T confirm the field resilience of both the graphene JJ and superconducting circuit.

5.2.3. Two tone spectroscopy in high parallel magnetic fields

In order to better understand the microwave excitation spectra of our system we proceed to measure it directly via two-tone spectroscopy [1]. The readout tone is set to f_r whilst a second tone f_d is used to drive the circuit. Excitation of the system

results in a state dependent shift of the resonator frequency, and is detected by measuring the change in the complex transmission S_{21} at f_r. At $V_G = 0$ V (p-regime), two-tone spectroscopy at $B_\parallel = 0$ and 1 T (Fig. 5.5a) can be fitted with a Lorentzian to extract the transmon transition $f_t \simeq 5.2$ GHz and transition linewidth $\gamma \simeq 400$ MHz. At $B_\parallel = 1$ T, f_t and thus E_J differ only slightly with γ increasing slightly from 350 MHz to 425 MHz. The transmon resonator coupling $g = \sqrt{\chi\Delta} = 43$ MHz is extracted from the observed dispersive shift χ and detuning Δ, and used in the calculation of f_t in Fig. 5.4. We attribute the change in f_t from Fig. 5.4b and the large γ to the dielectric induced charge noise mentioned previously. An estimate of $E_J = 40.2\,\mu\text{eV} = 9.72$ GHz can be provided using the relation $E_t = hf_t \simeq \sqrt{8E_JE_C}$. Performing two-tone spectroscopy in the n-regime while tuning V_G reveals a gate-tunable energy level that is visible above and below the resonator (Fig. 5.5b, V_{CNP} not specified due to gate drift during measurement) that can be fitted to extract f_t and γ, giving a minimum linewidth of 166 MHz (see Fig. 5.6 for the raw data).

5.3. Discussion

The observation of a transition and the inferred high value of E_J in the n and p-regimes (Fig. 5.5a) provides additional confirmation of the electron-hole symmetry expected in graphene. Additional measurement of the higher order two-photon f_{02} transition would allow for exact measurements of E_J and E_C via diagonalisation of the Hamiltonian, enabling investigations into mesoscopic effects of interest in graphene JJs [31, 32]. Importantly, the transition and thus E_J can be varied over a wide frequency range, satisfying a key requirement for implementation into topological QC proposals [3]. If graphene based transmons are to be successfully implemented into these proposals however, the large linewidths that currently prevent measurements of relaxation and coherence lifetimes (T_1, T_2^*) must be reduced. We believe that material improvements to the dielectric materials can achieve this.

In conclusion, we have integrated a graphene JJ into a superconducting circuit to make a graphene based transmon. Additionally, we have achieved operation at $B_\parallel = 1$ T, a magnetic field more than an order of magnitude higher than previous studies [16, 33]. While the broad linewidths prevented the demonstration of coherent qubit control, these results establish graphene based microwave circuits as a promising tool for topological and hybrid QC schemes, and for probing mesoscopic phenomena of interest at high magnetic fields.

Data availability
The data used to support this study, and the code used to generate the figures are available from a public data repository here https://doi.org/10.4121/uuid:b7340d11-e47e-44eb-a60d-679d758c7160.
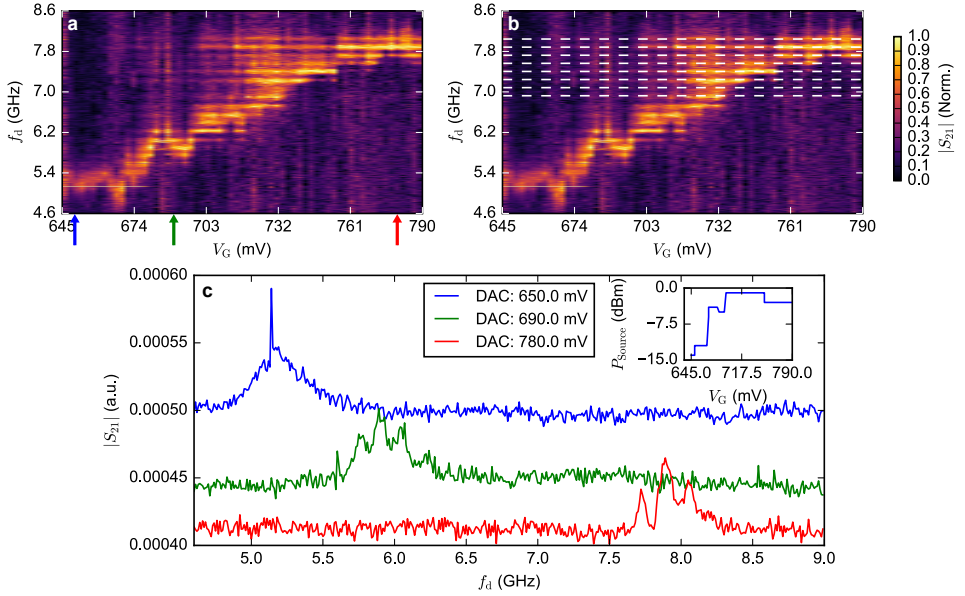
Figure 5.6: Readout circuit resonance **a** Normalised heat map of S_{21} during two-tone spectroscopy as the gate voltage V_G and drive tone f_d is varied. **b** The response of f_t is modulated by background resonances due to a standing wave in the readout circuit, as evidenced by the white lines. **c** Line traces showing $|S_{21}|$ at several V_G values (corresponding to linecuts at coloured arrows in **a**. The sharp resonance at 5.143 GHz is due to interference effects from an additional $\lambda/4$ resonator multiplexed to the common feedline. The inset demonstrates that above ~ 670 mV the higher power required to drive the transition excites additional modes in the circuit, giving the modulation in response as seen in **a**. Above 720 mV the resonances become so extreme that it is difficult to analyse the data reliably, so they are excluded from the main text.

Author contributions
K.W. and T.T. grew the hBN crystals, J.G.K. and W.U. fabricated the devices, J.G.K., K.L.v.d.E. and D.d.J performed the measurements and J.G.K. and K.L.v.d.E. analysed the measurements. The manuscript was prepared by J.G.K. with K.L.v.d.E., S.G., M.C. and L. P. K. providing input. S.G., M.C. and L.P.K. supervised the project.

5.4. Supplementary material
5.4.1. Readout circuit resonance
Normalised heatmap of $|S_{21}|$ during two-tone spectroscopy of the transmon energy level f_t as the gate voltage V_G is varied (Figure 5.6a). A sharp peak (dip) at 5.143 GHz (5.640 GHz) is visible due to resonant driving of additional $\lambda/4$ resonators multiplexed to the same feedline. The drive is provided to the transmon
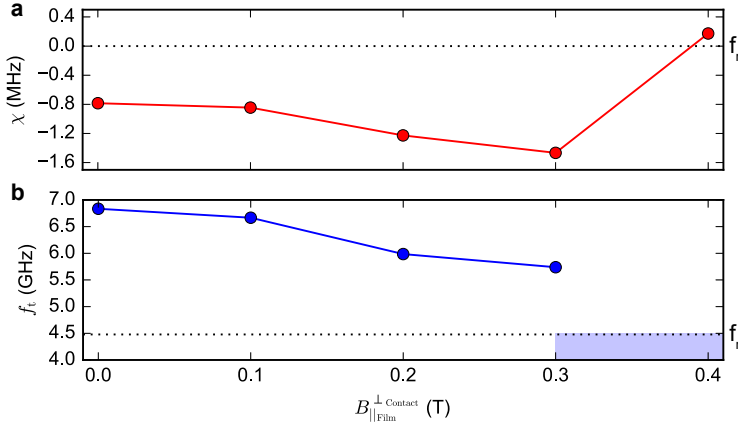
Figure 5.7: Lead alignment **a** Dependence of dispersive shift χ with respect to field $B_{\parallel\mathrm{Film}}^{\perp\mathrm{Contact}}$ applied perpendicular to the length of the junction contacts, but parallel to the film. **b** Extracting f_t from χ shows that as $B_{\parallel\mathrm{Film}}^{\perp\mathrm{Contact}}$ is applied the E_J reduces significantly. As f_t approaches f_r, χ increases until f_t passes through f_r resulting in the sign change of χ. Above $B_{\parallel\mathrm{Film}}^{\perp\mathrm{Contact}} = 0.4$ T the dispersive regime is no longer valid, meaning f_t cannot be accurately estimated. These results imply that the E_J of the junction is only protected if B is applied along the length of the junction contacts.

indirectly, through the coupled resonator. As the detuning $\Delta = f_t - f_r$ is increased, the amount of drive power required to excite the transition at f_t also increases due to the filtering effect of the resonator (Figure 5.6c inset) and low relaxation time T_1. Above 5.7 GHz the drive power becomes so high that an additional resonant mode in the circuit is excited, modulating the two-tone response of S_{21}. We attribute these oscillations to a standing wave ($\Delta f = 160$ MHz, $\lambda = 1.25$ m) in the coaxial cables caused by an impedance mismatch at the device (Figure 5.6b). The resonance was only observable whilst near f_t and at very high power, making a simple background subtraction difficult. Above $\sim$720 mV the very high power required to drive the transition causes many resonances, complicating the analysis. Due to this, data above this point was excluded from the analysis in the main text.

5.4.2. Lead orientation

$\perp$ During measurement it was found that the orientation of the field with respect to the leads was of key importance. Initially the field was applied along the main axis of the 6-1-1 T vector magnet; parallel to the film and perpendicular to the junction contacts ($B_{\parallel\mathrm{Film}}^{\perp\mathrm{Contact}}$). Despite careful alignment as described in Sec. 4.8.1 the Josephson energy (E_J) was found to significantly reduce at only $\sim$ 400 mT. In Fig. 5.7b as $B_{\parallel\mathrm{Film}}^{\perp\mathrm{Contact}}$) is increased, E_J reduces, causing the transmon transition to also reduce (as $f_t \simeq \sqrt{8E_J E_C}$). As f_t approaches the resonator the dispersive shift χ increases in magnitude, eventually switching sign as f_t passes through f_r (Fig. 5.7a). In contrast, applying the field parallel to the film and along the long
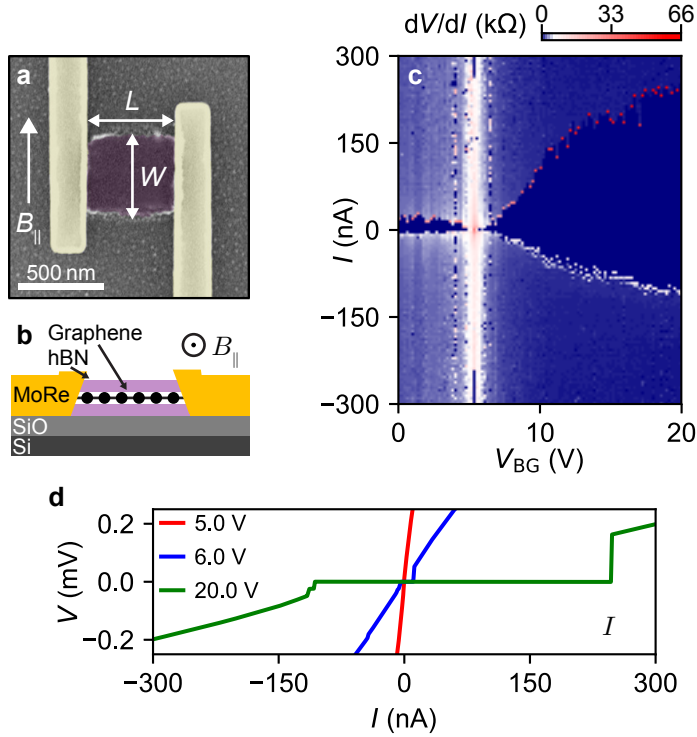
Figure 5.8: DC characterisation of graphene JJs - **a** Scanning electron microscope image and **b** schematic cross-section of a ballistic edge-contacted graphene Josephson junction encapsulated in a hexagonal boron nitride (hBN) stack. Device areas are defined for fixed length $L = 500$ nm, while the width W is varied from 100 nm - 700 nm. The external magnetic field $B_\parallel$ is applied parallel to the junctions plane and leads. The lead area is kept narrow to minimize vortex penetration into the junction. **c** Measured dV/dI versus I and V_{BG} in a 500x500 nm junction. **d** V versus I traces at different V_{BG} showing the asymmetric I_R and I_S and rapid decay of R_N from CNP.

axis of the leads (see Fig. 5.1c) the junction is able to retain a stable E_J up to $B^{\parallel\text{Contacts}}_{\parallel\text{Film}} = 1$ T (Fig. 5.4c).

5.4.3. DC characterisation of graphene JJs

To characterise the performance of graphene JJs in magnetic field and better understand how the junction width W affects E_J, multiple JJs of varying width W between 100 nm and 700 nm were fabricated on doped Si substrates with a thermal oxide dielectric layer. Fig. 5.8a shows a false coloured SEM of a typical graphene junction, with Fig. 5.8b showing a diagram of the cross section. Figure 5.8c shows the numerically calculated differential resistance, dV/dI, for a typical junction ($W = 500$ nm) as a function of applied DC current as the carrier density in the graphene is tuned using the global back gate. For each trace, the DC current is swept from negative to positive applied current. The dark blue regions show the regions where
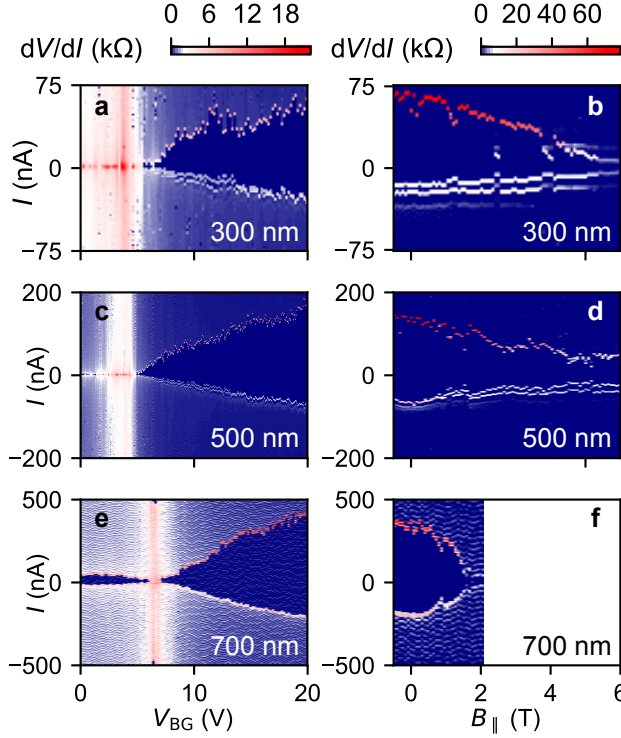
Figure 5.9: Differential resistance as a function of applied current for increasing back gate voltage for junction widths of **a** 300 nm **b** 500 nm and **c** 700 nm measured at $B_\parallel = 0$ T. Both I_S and I_R increase with V_{BG} as the carrier density is increased. **d-f** Differential resistance as a function of applied current for increasing parallel magnetic field $B_\parallel$ at $V_{BG} = 20$ V.

the junction is superconducting, i.e. $\mathrm{d}V/\mathrm{d}I = 0\,\Omega$. At positive values of applied current, the junction switches from the superconducting to the normal state at a switching current I_S, while at negative values of the bias current, the device transitions from the normal to superconducting state at a retrapping current I_R. As I_S tends to occur near but slightly below I_C we can then use this to estimate the E_J of the junction using the relation $E_J = I_C \Phi_0/2\pi \simeq I_S \Phi_0/2\pi$. We note that I_S is always larger than I_R, although the junctions appear to be in the intermediate damping regime. This hysteretic behavior could therefore be explained by heating effects. To emphasise the difference in normal resistance at different backgate voltages line cuts at charge neutrality and maximum backgate voltage are shown in Figure 5.8d.

In total 11 junctions were measured, with the junctions fabricated on 3 different graphene flakes to check for consistency and reproducibility. Fig. 5.9 shows the differential resistance for junctions of widths W = 300 nm, 500 nm, and 700 nm taken with respect to gate and parallel magnetic field. Smaller junctions of W < 300 nm did not show a notable supercurrent, most probably due to disorder at the
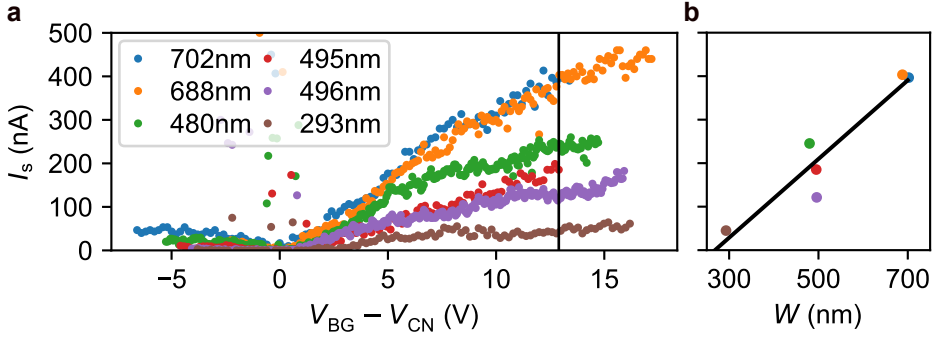
Figure 5.10: **a** Extracted I_S versus $V_{BG} - V_{DP}$ for different W. **b** Width dependence of switching current at relative backgate voltage of $V_{BG} - V_{DP} = 14.3$ V. A linear fit shows a cutoff for W of 260 nm below which no supercurrent can be sustained due to edge scattering.

5

edge of the graphene flake. All devices showed the Dirac point occurring between V_{BG} = 2 - 5 V, indicating positive (n-type) doping. Magnetic field scans were taken at back gate voltage of V_{BG} = 20 V and show that the junctions were able to retain high I_C up to high $B_∥$. In particular, the 300 nm and 500 nm junctions retain up to $\sim 2/3$ of their E_J up to 2 T with a monotonic reduction, making them very effective as field resilient JJs.

As targeting a specific E_J can be very important depending on the application, a study of I_S versus V_{BG} for different W is presented in Fig. 5.10a. In Fig. 5.10b I_S of each junction is measured at the same V_{BG} after compensating for the Dirac point V_{DP}. Assuming each 2DEG has equal coupling to the backgate, an equivalent voltage should correspond to an equivalent carrier density. Assuming a linear dependence on W, I_S can be seen to reach 0 nA at $W \sim 260$ nm, implying that edge scattering effects in graphene JJs becomes so extreme that supercurrents can no longer be sustained.

References

[1] Koch, J. *et al.* Charge-insensitive qubit design derived from the Cooper pair box. *Physical Review A* **76**, 042319 (2007).

[2] Hassler, F., Akhmerov, A. R. & Beenakker, C. W. J. The top-transmon: a hybrid superconducting qubit for parity-protected quantum computation. *New Journal of Physics* **13**, 095004 (2011).

[3] Hyart, T. *et al.* Flux-controlled quantum computation with Majorana fermions. *Physical Review B* **88**, 035121 (2013).

[4] Aasen, D. *et al.* Milestones toward Majorana-based quantum computing. *Physical Review X* **6** (2016).

[5] Kubo, Y. *et al.* Hybrid quantum circuit with a superconducting qubit coupled to a spin ensemble. *Physical Review Letters* **107**, 220501 (2011).

[6] Ranjan, V. *et al.* Probing dynamics of an electron-spin ensemble via a super-conducting resonator. *Physical Review Letters* **110**, 067004 (2013).

[7] Calado, V. E. *et al.* Ballistic Josephson junctions in edge-contacted graphene. *Nature Nanotechnology* **10**, 761–764 (2015).

[8] Van Woerkom, D. J., Geresdi, A. & Kouwenhoven, L. P. One minute parity life-time of a NbTiN Cooper-pair transistor: Supplementary Information. *Nature Physics* **11**, 547–550 (2015).

[9] Kurizki, G. *et al.* Quantum technologies with hybrid systems. *Proceedings of the National Academy of Sciences* **112**, 3866–3873 (2015).

[10] Ristè, D. *et al.* Millisecond charge-parity fluctuations and induced decoher-ence in a superconducting transmon qubit. *Nature Communications* **4**, 1913 (2013).

[11] Doh, Y. *et al.* Applied physics: Tunable supercurrent through semiconductor nanowires. *Science* **309**, 272–275 (2005).

[12] Van Woerkom, D. J. *et al.* Microwave spectroscopy of spinful Andreev bound states in ballistic semiconductor Josephson junctions. *Nature Physics* **13**, 876–881 (2017).

[13] Hays, M. *et al.* Direct Microwave Measurement of Andreev-Bound-State Dy-namics in a Semiconductor-Nanowire Josephson Junction. *Physical Review Letters* **121**, 047001 (2018).

[14] De Lange, G. *et al.* Realization of microwave quantum circuits using hybrid superconducting-semiconducting nanowire Josephson elements. *Physical Review Letters* **115**, 127002 (2015).

[15] Larsen, T. W. *et al.* Semiconductor-nanowire-based superconducting qubit. *Physical Review Letters* **115**, 127001 (2015).

[16] Luthi, F. *et al.* Evolution of nanowire transmon qubits and their coherence in a magnetic field. *Physical Review Letters* **120** (2018).

[17] Allen, M. T. *et al.* Observation of electron coherence and Fabry-Perot standing waves at a graphene edge. *Nano Letters* **17**, 7380–7386 (2017).

[18] Chtchelkatchev, N. M. & Burmistrov, I. S. Conductance oscillations with mag-netic field of a two-dimensional electron gas superconductor junction. *Physical Review B* **75**, 214510 (2007).

[19] Stan, G., Field, S. B. & Martinis, J. M. Critical field for complete vortex expul-sion from narrow superconducting strips. *Phys. Rev. Lett.* **92**, 97003–97004 (2004).

5

[20] Bothner, D., Gaber, T., Kemmler, M., Koelle, D. & Kleiner, R. Improving the performance of superconducting microwave resonators in magnetic fields. *Applied Physics Letters* **98**, 102504 (2011).

[21] Kroll, J. G. *et al.* Magnetic field resilient superconducting coplanar waveguide resonators for hybrid cQED experiments (2018). `1809.03932`.

[22] Deng, M. T. *et al.* Majorana bound state in a coupled quantum-dot hybrid-nanowire system. *Science* **354**, 1557–1562 (2016).

[23] Suominen, H. J. *et al.* Zero-Energy Modes from Coalescing Andreev States in a Two-Dimensional Semiconductor-Superconductor Hybrid Platform. *Physical Review Letters* **119**, 176805 (2017).

[24] Zhang, H. *et al.* Quantized Majorana conductance. *Nature* **556**, 74–79 (2018).

[25] Megrant, A. *et al.* Planar superconducting resonators with internal quality factors above one million. *Applied Physics Letters* **100**, 113510 (2012).

[26] Singh, V., Schneider, B. H., Bosman, S. J., Merkx, E. P. J. & Steele, G. A. Molybdenum-rhenium alloy based high- Q superconducting microwave resonators. *Applied Physics Letters* **105**, 222601 (2014).

[27] Samkharadze, N. *et al.* High-Kinetic-Inductance Superconducting Nanowire Resonators for Circuit QED in a Magnetic Field. *Physical Review Applied* **5**, 044004 (2016).

[28] Reed, M. D. *et al.* High-fidelity readout in circuit quantum electrodynamics using the jaynes-cummings nonlinearity. *Physical Review Letters* **105** (2010).

[29] Schuster, D. I. *Circuit Quantum Electrodynamics*. Ph.D. thesis, Yale University (2007).

[30] Lee, P. A. & Stone, A. D. Universal conductance fluctuations in metals. *Physical Review Letters* **55**, 1622–1625 (1985).

[31] Nanda, G. *et al.* Current-phase relation of ballistic graphene Josephson junctions. *Nano Letters* **17**, 3396–3401 (2017).

[32] Kringhøj, A. *et al.* Anharmonicity of a superconducting qubit with a few-mode Josephson junction. *Physical Review B* **97**, 060508 (2018).

[33] Ku, J., Yoscovits, Z., Levchenko, A., Eckstein, J. & Bezryadin, A. Decoherence and radiation-free relaxation in Meissner transmon qubit coupled to Abrikosov vortices. *Physical Review B* **94**, 165128 (2016).

6

A semiconductor nanowire Josephson junction laser

M. C. Cassidy*, W. Uilhoorn*, **J. G. Kroll**, D. de Jong, D. J. van Woerkom, J. Nygård, P. Krogstrup, L. P. Kouwenhoven

We demonstrate a microwave laser made from a proximitised semiconducting nanowire strongly coupled to a multi-mode superconducting coplanar waveguide cavity. A small DC voltage bias applied to the nanowire Josephson junction results in photon emission when the voltage bias is equal to a multiple of the fundamental cavity frequency, via the ac Josephson effect. Analysis of the real time emission statistics shows > 0.3 ms coherence time, at a photon occupancy of ∼1000 photons. The electrical tuneability of the photon emission provided by the proximitised semiconducting nanowire allows for fast control of the laser emission, paving the way for on-chip control and readout of quantum devices.

*Equal contribution

6.1. Introduction

Engineered superconducting circuits have made rapid progress in simulating atomic systems at microwave frequencies [1–3] and form a promising platform for a scaleable system for quantum information processing [4, 5]. The compact size of these circuits compared to the relatively large size of the artificial atoms allows for strong coupling rates to be achieved, and makes them easy to integrate into complex device architectures. One of the simplest artificial atoms that can be considered is a single Josephson junction (JJ), a weak link connecting two bulk superconducting electrodes. The Josephson coupling energy of this weak link is $E_J = \frac{\hbar I_c}{2e}$, where I_c is the critical current and $2e$ the Cooper pair charge. For a single superconductor-insulator-superconductor (SIS) junction, E_J is fixed in device fabrication, but can be tuneable if two SIS JJs are arranged side by side in a SQUID geometry. Recently, it has been shown that a highly efficient microwave laser, or maser can be made by strongly coupling a JJ to a high Q superconducting cavity [6, 7]. In this work, a split JJ structure was used, and the Josephson coupling was tuned by an external magnetic flux. Although this allowed for the investigation of the device performance under a broad range of Josephson couplings, ultimately the coherence time of the laser was limited by flux noise. Lasing from other nanoscale systems in the microwave regime has relied on tunnelling via superconducting[8, 9] and semiconducting islands [10], where the finite charging energy has led to linewidth broadening and emission blinking due to charge noise.

Superconductor-normal-superconductor (SNS) Josephson junctions formed in proximitised semiconductors are key materials for a range of emerging technologies. Recent advances in materials have allowed the epitaxial growth of a superconductor on the semiconductor [11, 12] which has resulted in strongly proximitised devices that display a hard induced superconducting gap and significant supercurrents that can be tuned by an external electrostatic gate [13]. These devices have been incorporated into microwave circuits to form hybrid transmon qubits [14, 15] where the Josephson coupling, and so qubit frequency is controlled by a local gate, and form the basis for many topological quantum computing schemes [16–18].

In this Letter we demonstrate a microwave laser made from a proximitised Al/InAs nanowire strongly coupled to a multi-mode superconducting coplanar waveguide cavity. A small DC voltage bias applied to the nanowire JJ results in photon emission when the voltage bias is equal to a multiple of the fundamental cavity frequency, via the ac Josephson effect. Using an external gate, we can control the Cooper pair tunnelling rate through the junction, and hence tune the emission intensity of the laser. Analysis of the real time emission statistics shows coherence times exceeding 300 μs, representing more than an order of magnitude improvement over the SIS JJ laser [6].

6.2. Device design

Fig. 6.1a shows an optical image of the device. The laser is made from a proximitised semiconducting nanowire Josephson junction embedded into a half-wave
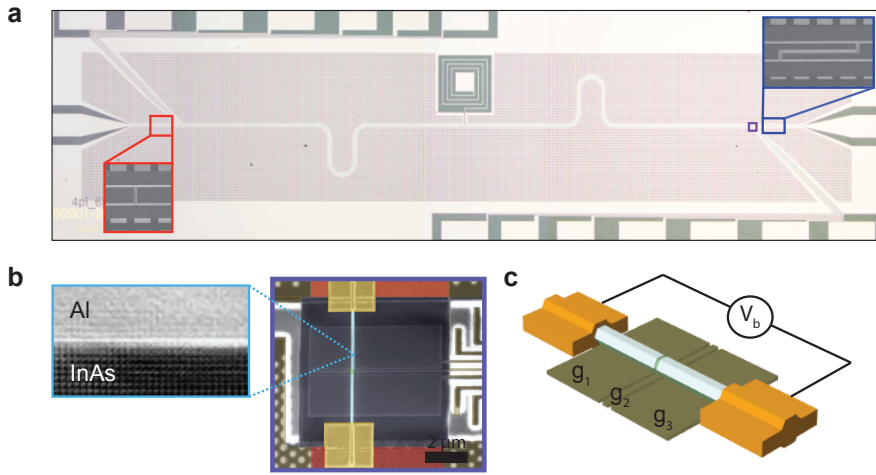
Figure 6.1: Nanowire Josephson junction laser **a** Optical microscope image of the nanowire JJ laser. The device consists of a NbTiN CPW half-wave resonator with fundamental frequency $f_0 = 5.4818\,\text{GHz}$, together with an InAs-Al nanowire JJ located at the electric field anti-node of the cavity. A DC bias is applied directly across the nanowire JJ via a spiral inductor located at the electric field node of the resonator. Insets: Asymmetric coupling capacitances ensure that the microwave photons leave predominantly via the output port of the cavity. **b** Transmission and scanning electron micrograph image and **c** Schematic of the InAs-Al nanowire Josephson junction. Metallic gates g_1 and g_3 control the electrochemical potential in the nanowire, while the Josephson coupling is tuned by g_2.

superconducting coplanar waveguide (CPW) resonant cavity ($f_r = 5.4818\,\text{GHz}$). The CPW resonator is defined by reactive ion etching a thin ($d = 20\,\text{nm}$) NbTiN film sputtered on a cleaned sapphire wafer. In the same lithography step, we define a series of electrostatic gates for tuning the electrochemical potential in the nanowire, and a spiral inductor for applying a voltage bias across the nanowire JJ. Two outer gates, g_1 and g_3, control the chemical potential in the nanowire underneath the superconductor, while a central gate g_2 tunes the Josephson coupling. The cavity is made strongly asymmetric, with the rate of photon emission out of the input port ($k_i = 1.5\,\text{MHz}$) roughly an order of magnitude less than the rate of photon emission out the output port ($k_o = 15\,\text{MHz}$). A single InAs/Al nanowire is then deposited perpendicular to the cavity using a deterministic deposition technique (Fig 6.1b). A thin ($\sim 30\,\text{nm}$) layer of PECVD SiN provides insulation between the nanowire and the gates underneath. The Josephson junction is defined by wet etching the aluminum shell of the nanowire using Transene D solution. Contact to the nanowire is made by Ar etching the native oxide from the Al shell, then sputtering NbTi/NbTiN followed by evaporation of a Au cap that acts as a quasiparticle trap. The device is then packaged in a light-tight enclosure that suppresses unwanted free-space cavity modes, and measured in a dilution refrigerator with a base temperature of $\sim 15\,\text{mK}$. We apply a voltage bias to the nanowire using an on-board voltage divider circuit that reduces the associated frequency noise of the emitted photons below that of the cavity linewidth, and measure the emission spectrum at the output of the cavity with a spectrum analyser.

6.3. Emission spectra and characteristics

The device is tuned into the tunnelling regime by pinching off gate g_2, while keeping g_1 and g_3 fixed at a small positive voltage. We measure the current flowing through the device, I_D (Fig. 6.2a) and simultaneously record the power spectral density $S(f)$ of the emitted radiation (Fig. 6.2b) around the fundamental resonant frequency of the cavity. At voltage biases equal to a multiple of the fundamental cavity frequency, we observe a burst of microwave radiation from the cavity accompanied by an increase in the Cooper pair tunneling rate across the junction. The emission intensifies with increased voltage bias, when photons emitted into higher-order cavity modes are down-converted to multiple photons at the fundamental frequency of the cavity. The mixing required for this down-conversion process arises from the non-linearity of the Josephson junction, similar to the recently demonstrated SIS JJ laser[6], and shows chaotic behavior expected by a driven non-linear coupled oscillator system [7]. Unlike the SIS JJ laser, where the emission intensity increases all the way up to the superconducting gap Δ, here the emission intensity is quenched after $n = 5$. This quenching coupled with an increase in the subgap tunneling current observed in the DC transport through the device, a result of the excitation of quasiparticles across the junction.

A zoom-in of the emission at $n = 4$, where the emitted power is the strongest, is shown in Fig. 6.3a. Analysis of the emission spectrum at $V_b = -44.55\,\mu\text{V}$ (Fig. 6.3b) shows a time-averaged Lorentzian spectrum with a full width half max $\sim 6.1\,\text{kHz}$, corresponding to a phase coherence time of $\tau_c = 1/\pi\Delta f_0 = 52\,\mu\text{s}$. By applying a
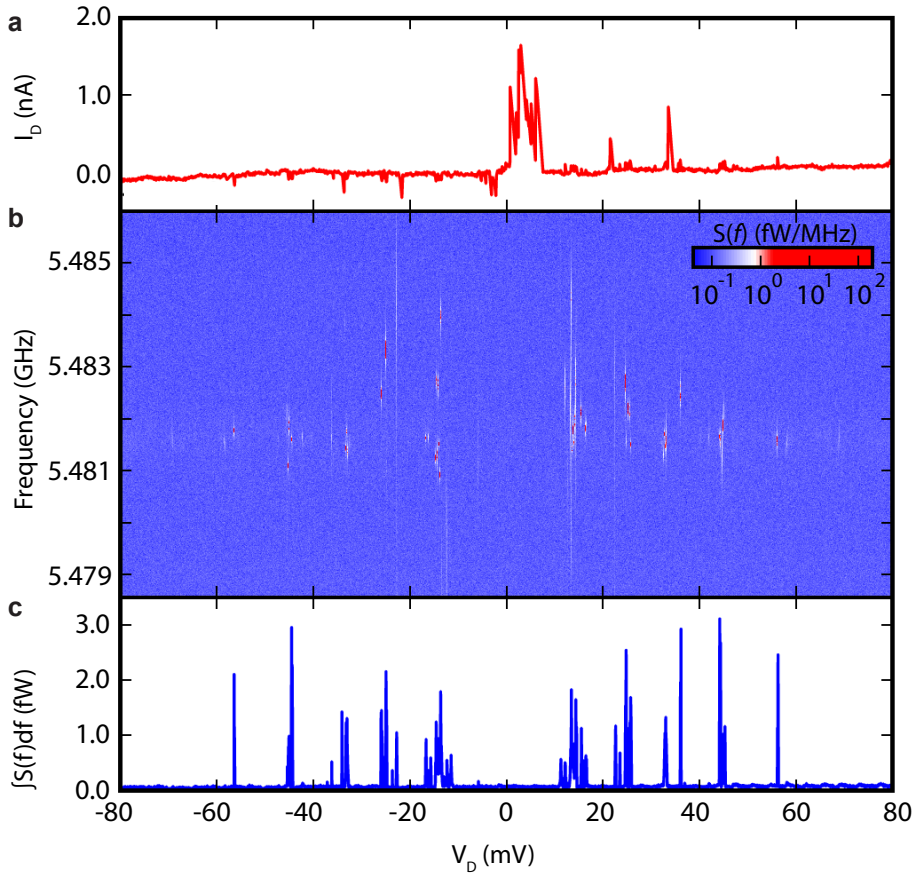
Figure 6.2: Emission and lasing **a** Current flowing through the nanowire JJ I_D as a function of voltage bias V_b when g_2 is close to pinch off. **b** Power spectral density of the emitted signal measured at the cavity output. **c** Integrated power spectral density across the frequency span in b.
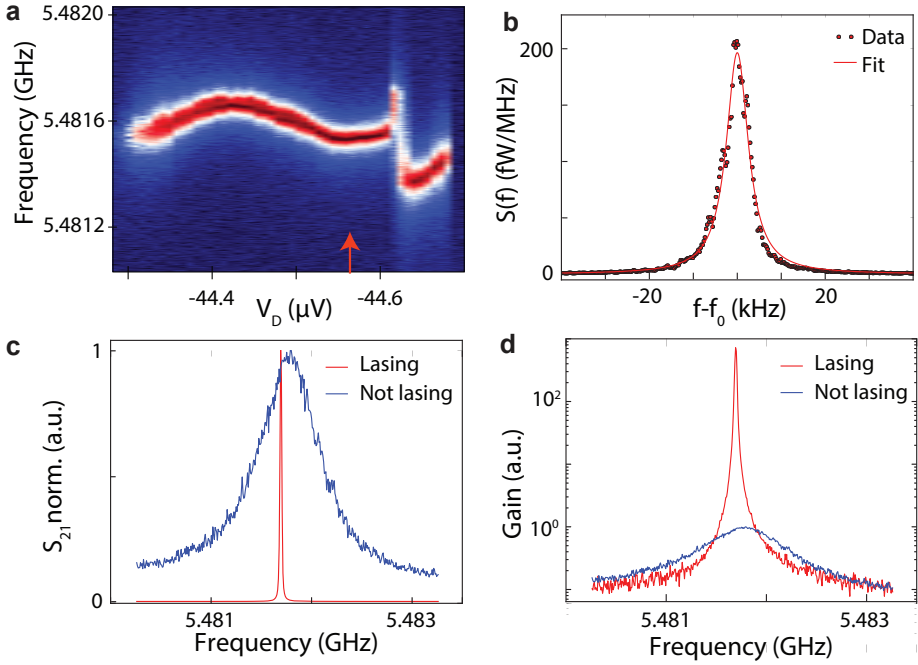
Figure 6.3: Linewidth and Gain **a** Zoom in of S(f) vs V_b around the n=4 emission peak. **b** Line cut at $V_b = -44.57\,\mu V$ with Lorentzian fit. **c** Emission linewidth narrowing and **d** Gain for the device when lasing and not lasing.

small input signal to the cavity, we measure almost 3 orders of magnitude linewidth narrowing (Fig. 6.3c) and almost three orders of magnitude gain (Fig. 6.3d) when the device is lasing compared to when it is biased at an off-resonant point.

6.4. Laser coherence

To gain a further insight into the emission properties of the SNS JJ laser, we study the emission statistics in real time. For each of the emission peaks, we sample the in-phase and quadrature components of the output field at a rate of 12.5 MHz using a heterodyne demodulation setup. IQ histograms for each of the emission peaks are shown in Fig. 6.4a. From this we extract the average coherent amplitude A (Fig. 6.4b), and fluctuations δA (error bars, Fig. 6.4b) of the output field. Higher voltage bias results in stronger emission amplitude, as they allow for the transfer of more Cooper pairs across the JJ for a given amount of time. A clear even-odd structure is evident in the emission amplitude, with the emission peaks corresponding to even emission, due to the enhanced parametric down conversion from photons of frequency $2f$ to two photons of frequency f. While the first four emission peaks show a clear donut structure indicating coherent emission, the IQ histogram of the 5th emission peak shows an additional peak around $(I, Q) = (0,0)$,
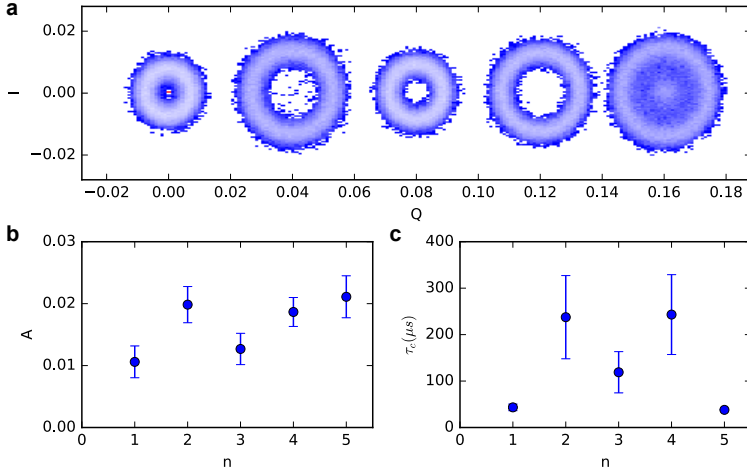
Figure 6.4: Laser Coherence **a** IQ histograms of the nanowire laser output emission at voltage bias points corresponding to $1 \leq n \leq 5$. Each histogram is offset by $Q = 0.04$ for clarity. **b** Extracted emission amplitudes A from fitting the 2D histogram to a gaussian function described in the text. **c** Average phase coherence times extracted from performing an autocorrelation of the raw time domain data at each emission point.

corresponding to thermal, rather than coherent emission. Analysis of the raw time series data for each of the emission peaks allows us to directly extract the average phase coherence time τ_c (Fig. 6.4c) by performing an autocorrelation on the time domain data (see Supplementary Information). We see that the laser coherence time increases with emission amplitude, to almost 0.3 ms at the $n = 4$ peak, and then rapidly drops as the laser emission is quenched by quasiparticle tunneling. Nevertheless, the coherence measured at the $n = 4$ peak far exceeds the coherence time of state of the art superconducting qubits, thus demonstrating this laser as a practical source of coherent radiation for on-chip qubit control and readout.

6.5. Quasiparticle dynamics

The emission blinking seen at the $n = 5$ emission peak provides a unique opportunity for studying quasiparticle poisoning dynamics in an open SNS JJ system where charging energy has been almost completely quenched. Quasiparticle poisoning in such a system is relevant for topological quantum computing schemes that rely on turning charging energy on and off, where parity is destroyed by the tunnelling of a quasiparticle across an SNS JJ. Quasiparticle tunnelling across the junction absorbs microwave photons from the cavity, but does not generate photons as the energy is dissipated into the continuum. In the SIS JJ laser, this excitation and resultant damping process only occurred at $V_b > \Delta$, a measure of the hardness of the superconducting gap. In an SNS junction, however, the finite density of states within the gap allows for this excitation to occur with quasiparticles of much lower energy than Δ. We are able to directly monitor the quasiparticle poisoning of the
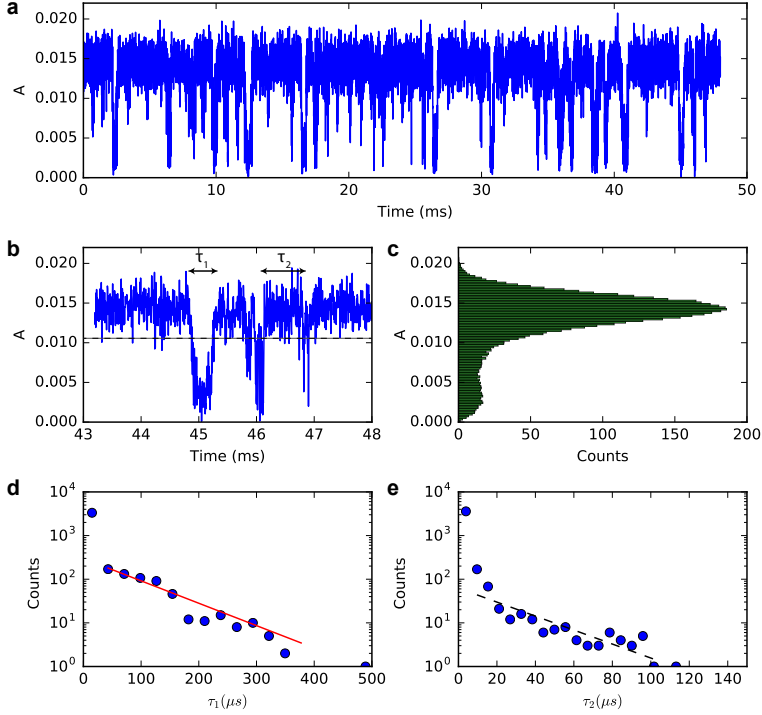
Figure 6.5: Quasiparticle poisoning **a,b** Laser emission amplitude as a function of time at the $n =$ 5 emission peak. τ_1 is the time the laser spends on, and τ_2 the time the laser spends turned off. Each point represents an integration of the demodulated emission amplitude amplitude for 100 ns. **c** Histogram of the time trace of length 500 ms. From fitting the areas of the histogram, we estimate that the laser spends 91% lasing. The threshold is set at 0.0105. **d** Histograms of times spent in the lasing state, and **e** off state allow us to extract characteristic timescales for the quasiparticle poisoning and unpoisoning process.

device in real time, by studying the dynamics of the laser emission around the n = 5 emission peak. Fig. 6.5a shows a representative time trace of the amplitude of the laser emission when biased at $V_{\rm b} = 54\,\mu$V, with each point representing an integration time of 1 µs sampled at acquired at $1\,{\rm GS\,s^{-1}}$. Time traces of 10^6 data points are analysed. A histogram of the emission amplitudes shows two overlapping gaussians (Fig. 6.5c), centred at A = 0.0135 and A = 0.0025. By applying a threshold at A = 0.0105, we see the laser emits $\sim 91\%$ of the time. The emission switching times between on-off (τ_1) and off-on (τ_2) extracted from the time series data is shown in Fig. 6.5d-e. An exponential fit to this defines the characteristic lifetimes of the lasing process to be ($\tau_{\rm unpoisoned} = 120\,\mu$s) and $\tau_{\rm poisoned} = 20\,\mu$s). Similar quasiparticle poisoning times have recently been measured in an Andreev qubit device [19]. It should be noted that blinking events (on-off-on) with time scales faster than the integration time are not captured by this analysis.

    In conclusion, we have demonstrated coherent emission from a gate tunable

SNS JJ strongly coupled to a microwave cavity. Coherence times exceeding 0.3 ms are seen at the $n = 4$ emission peak, which exceeds the coherence time of state of the art superconducting qubits, making our laser a practical source of coherent radiation for on-chip qubit control and readout. Future work will concentrate on integrating this nanowire with hybrid superconducting systems, and study of their pulsed characteristics. Recently, a DQD nanowire laser has been able to read out the charge state of another nanowire double quantum dot at the other end of the superconducting cavity [20], demonstrating the immediate applicability of on-chip microwave sources in the readout and control of circuit QED devices.

6.6. Acknowledgements

6.7. Supplementary material

A NbTiN film ($d = 20$ nm) is first reactively sputtered on a C plane sapphire substrate (Kyocera). The resonator and gate structure are defined via electron beam lithography using CSAR 6200.09 resist, followed by dry etching in a SF_6/O_2 environment. A global SiN dielectric ($d = 30$ nm) is deposited using PECVD, and then selectively etched away from the device, excluding the region directly above the gates, using a buffered HF solution. A single InAs/Al nanowire is then deposited above the gates using a deterministic deposition technique. The Al shell was then wet etched (Transene D) in the region directly above gate g_2, forming a gate tunable tunnel barrier. The source and drain contacts to the nanowire were formed by sputtered NbTiN. A short Ar ion mill before metal deposition removes the surface oxide of the nanowire to ensure good electrical connection. A thin layer ($d = 30$ nm) of Au is evaporated over the NbTiN contacts to act as a local quasiparticle trap.
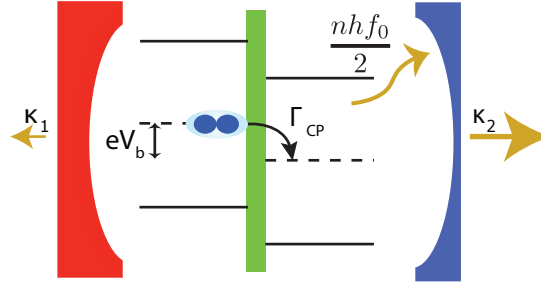
6

Figure 6.6: Illustration of the lasing process. A DC voltage bias applied across the Josephson junction will result in photon emission when the excess energy provided by the Cooper pairs can be absorbed by the cavity, $eV_b = nhf_0/2$. Photon emission out of the cavity is controlled by coupling capacitors, which are made heavily asymmetric so that the emission rate out the output port $\kappa_2 = 10\kappa_1$
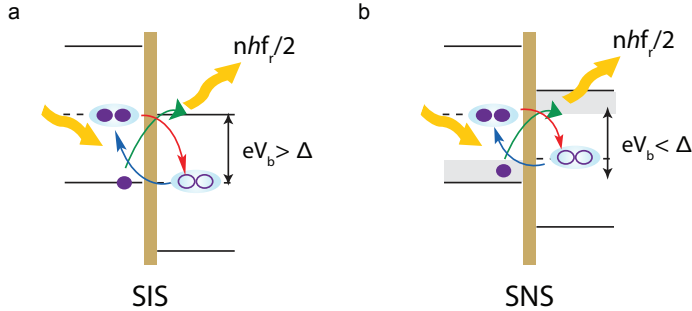
Figure 6.7: Comparison between SIS and SNS lasing **a** In a SIS junction made with Al, the hard superconducting gap allows for lasing at voltage biases all the way up to the superconducting gap $eV_{cutoff} = \Delta$. Once the voltage bias exceeds Δ, absorption of radiation at $hf = \Delta$ excites quasiparticles across the junction, preventing further stimulated emission **b** In a proximitized nanowire, there is a significant density of states that can host quasiparticles within the superconducting gap. This results in a much lower V_{cutoff} than as seen in the SNS junction.
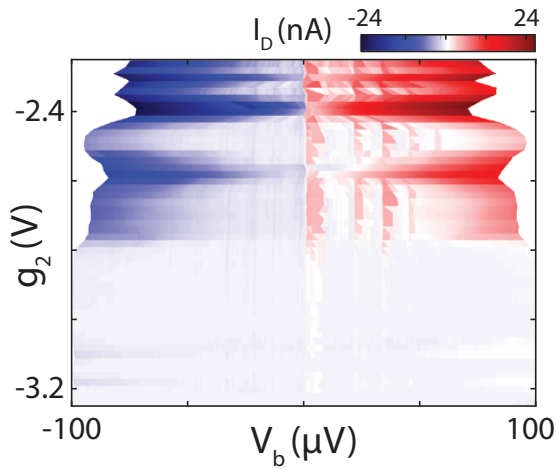
Figure 6.8: DC response. Current flowing through the nanowire as a function of voltage bias as gate g_2 is tuned close to pinch off. The bias voltage is swept from negative to positive voltages.

6
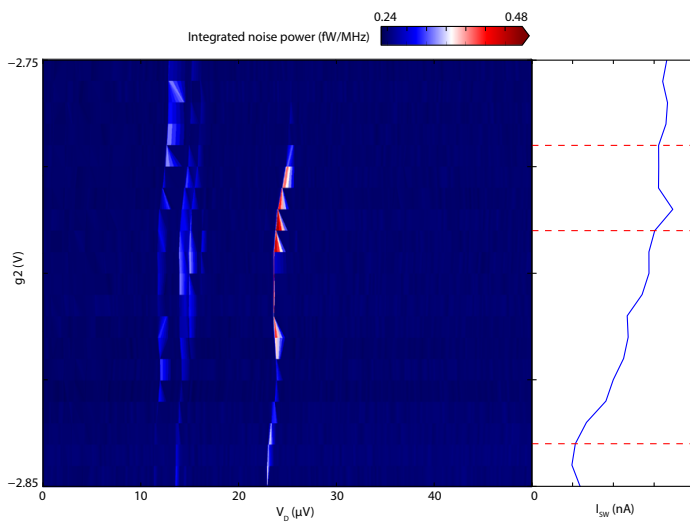
Figure 6.9: Gate tunable emission **a** Power spectra density as a function of voltage bias and **b** current flowing through the device as gate g_2 is tuned.
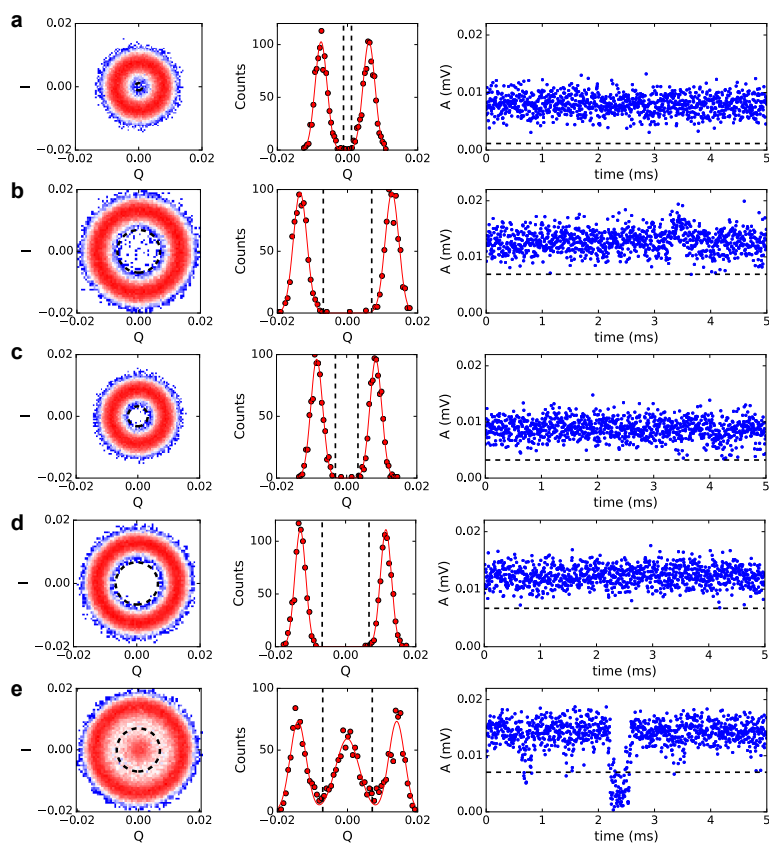
Figure 6.10: IQ Histograms **a-e** IQ Histograms, horizontal cuts at I=0, and example time trace for the first five emission peaks.

References

[1] O'Malley, P. J. J. *et al.* Scalable Quantum Simulation of Molecular Energies. *Phys. Rev. X* **6**, 31007 (2016).

[2] Salathé, Y. *et al.* Digital Quantum Simulation of Spin Models with Circuit Quantum Electrodynamics. *Phys. Rev. X* **5**, 21027 (2015).

[3] Kou, A. *et al.* Fluxonium-Based Artificial Molecule with a Tunable Magnetic Moment. *Phys. Rev. X* **7**, 31037 (2017).

[4] Dicarlo, L. *et al.* Demonstration of two-qubit algorithms with a superconducting quantum processor. *Nature* **460** (2009).

[5] Barends, R. *et al.* Coherent Josephson Qubit Suitable for Scalable Quantum Integrated Circuits. *Phys. Rev. Lett.* **111**, 80502 (2013).

[6] Cassidy, M. C. *et al.* Demonstration of an ac Josephson junction laser. *Science* **355**, 939–942 (2017).

[7] Simon, S. H. & Cooper, N. R. Theory of the Josephson Junction Laser. *Physical Review Letters* **121**, 027004 (2018).

[8] Astafiev, O. *et al.* Single artificial-atom lasing. *Nature* **449**, 588–590 (2007).

[9] Chen, F. *et al.* Realization of a single-Cooper-pair Josephson laser. *Phys. Rev. B* **90**, 20506 (2014).

[10] Liu, Y.-Y. *et al.* Semiconductor double quantum dot micromaser. *Science* **347**, 285–287 (2015).

[11] Krogstrup, P. *et al.* Epitaxy of semiconductor–superconductor nanowires. *Nature Materials* **14**, 400 (2015).

[12] Gazibegovic, S. *et al.* Epitaxy of advanced nanowire quantum devices. *Nature* **548**, 434 (2017).

[13] Chang, W. *et al.* Hard gap in epitaxial semiconductor–superconductor nanowires. *Nature Nanotechnology* **10**, 232–236 (2015).

[14] Larsen, T. W. *et al.* Semiconductor-nanowire-based superconducting qubit. *Physical Review Letters* **115**, 127001 (2015).

[15] De Lange, G. *et al.* Realization of microwave quantum circuits using hybrid superconducting-semiconducting nanowire Josephson elements. *Physical Review Letters* **115**, 127002 (2015).

[16] Hyart, T. *et al.* Flux-controlled quantum computation with Majorana fermions. *Physical Review B* **88**, 1–17 (2013).

6

[17] Karzig, T. *et al.* Scalable designs for quasiparticle-poisoning-protected topo-
     logical quantum computation with Majorana zero modes. *Physical Review B*
     95, 235305 (2017).

[18] Plugge, S., Rasmussen, A., Egger, R. & Flensberg, K.   Majorana box qubits.
     New Journal of Physics **19**, 012001 (2017).

[19] Hays, M. *et al.* Direct Microwave Measurement of Andreev-Bound-State Dy-
     namics in a Semiconductor-Nanowire Josephson Junction. *Physical Review
     Letters* **121**, 047001 (2018).

[20] Liu, Y.-Y. *et al.* On-Chip Quantum-Dot Light Source for Quantum-Device Read-
     out. *Physical Review Applied* **9**, 014030 (2018).

6

7

Superconducting qubits for coherently probing Majorana bound states

J. G. Kroll, W. Uilhoorn, A. Kringhøj, L. Casparis, T. Larsen, B. van Heck, A. Bargerbos, T. Stegwee, R. McNeil, M. Hesselberg, O. Erlandsson, J. Nygard, P. Krogstrup, G. de Lange, K. Petersson, A. Kou, C. M. Marcus, L. P. Kouwenhoven

This chapter discusses the development, fabrication and measurement of superconducting qubits that are capable of probing unique signatures of Majorana bound states (MZMs).

7.1. Introduction

Since the initial detection of Majorana bound states (MBSs) in hybrid super semi-conductor nanowire devices [1–3], rapid improvements in fabrication and materials synthesis [4–8] have only intensified research into how the properties of these topologically protected states can be used for quantum computation. Initial efforts focussed principally on braiding, the exchange of MBS that allows their non-Abelian statistics to be exploited for topologically protected quantum information processing. In the simplest case, three MBSs would be hosted on a T shaped semiconducting nanowire network coupled to superconducting islands. Braiding of the MBSs would be performed by physically exchanging them via electrostatic gates [9] or by tuning long range Coulomb interactions to perform an effective braiding operation [10]. After computation was completed, the information stored in the parity of the MBSs is converted from parity to charge, with a coupled superconducting transmon qubit then used to perform state readout. The majority of this thesis focussed on creating a transmon qubit compatible with the strong magnetic fields required to generate topological states (Chapt. 4 and 5).

Traditional transmon qubits consist of a superconducting island connected to ground by an AlO_x tunnel junction. This superconductor-insulator-superconductor (SIS) junction forms a Josephson junction (JJ) where tunnelling of Cooper pairs between the two superconducting condensates provides a Josephson coupling E_J between the island and the ground. The large capacitive coupling C between the island and the ground shunts the JJ and sets the charging energy E_C of the island. The spectrum of the device is then that of an LC oscillator, with the exception that the non-linearity of the JJ separates the energy levels allowing them to be individually addressed [11], with a high ratio of $E_J/E_C \sim 50 - 100$ suppressing the charge dispersion of the spectrum, drastically improving coherence.

At the same time as access to high quality semiconducting nanowires drove progress in the topological quantum computing (TQC) community, the superconducting quantum computing (SQC) community utilised them to produce a new class of hybrid superconductor-semiconductor qubits based on the transmon qubit [11]. Here the SIS junction is replaced with a proximitised semiconducting nanowire (InAs or InSb) where a superconductor-normal-superconductor (SNS) junction is created [12, 13]. Cooper-pairs are then no longer transferred by tunnelling processes but instead coherent Andreev reflection at the interfaces of the SNS region. The aforementioned progress in materials synthesis and fabrication rapidly enabled high yields and performance comparable to their traditional SIS JJ counterparts [14], inspiring experiments where complex mesoscopic effects important to TQC could be sensitively studied using microwave frequency superconducting circuits [15–17]. As these nanowires are naturally capable of hosting MBSs under the right conditions it is only natural to consider what effects if any a topological phase transition would have on the behaviour of a transmon qubit.

Early work principally focussed on the coupling that would occur between adjacent MBSs hosted on either side of a Josephson junction (JJ) [18–20], with particular interest placed on the resulting energy spectrum of such a device. Fig. 7.1a shows the circuit diagram of a nanowire transmon qubit where in addition to E_C
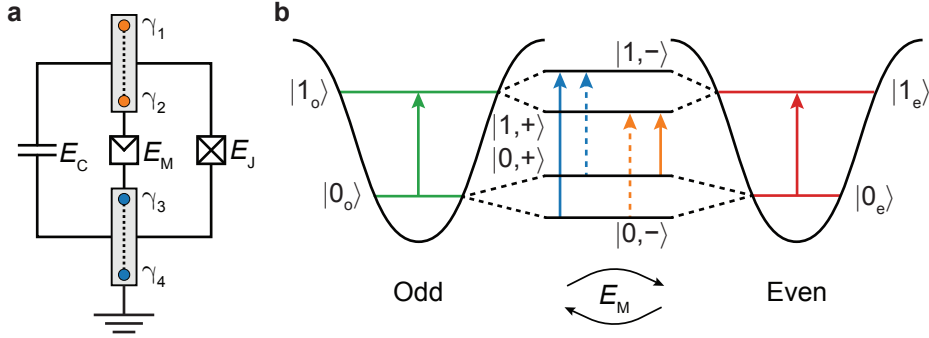
Figure 7.1: Majorana transmon qubits **a** Circuit diagram of a nanowire transmon qubit with E_C set by C, E_J by the SNS JJ and E_M by the coupling of γ_2 and γ_3. **b** Energy level diagram showing how the coherent coupling between the eigenstates of a transmon qubit and Majorana parity qubit create four separate transitions. Parity conserving transitions are denoted with solid lines. Adapted from [18].

and the E_J provided by the SNS junction, two regions of the nanowire have entered a topological phase creating four MBSs in total at each end of a topological region. The effective Hamiltonian of such a system can be defined as:

$$\hat{H} = 4E_C(\hat{n} - n_g)^2 - E_J\cos(\hat{\phi}) + 2E_M\imath\hat{\gamma}_2\hat{\gamma}_3\cos(\hat{\phi}/2) \tag{7.1}$$

where E_C and E_J are as defined previously, n is the Cooper pair occupancy of the island, n_g is the offset charge, ϕ is the phase difference between the island and ground, E_M is the coupling strength between the MBSs $\hat{\gamma}_2$ and $\hat{\gamma}_3$ and $\mathcal{P} = \imath\hat{\gamma}_2\hat{\gamma}_3$ serves as the parity operator for the local fermion that forms from the coupled MBS states. The coherent single electron coupling across the JJ provided by E_M modifies the anharmonic oscillator spectrum, allowing transitions between eigenstate branches of different parity that were previously decoupled. This coherent mixing of the transmon eigenstates with those of the Majorana parity operator creates four separate transitions instead of the previous two (Fig. 7.1b). Although E_C and E_J are well understood quantities that can be set by material and design considerations, comparatively little is known about the magnitude and control of E_M. Using numerical simulations, we can investigate multiple regimes to observe the effect this would have on the spectroscopic features and design a transmon qubit accordingly. Fig. 7.2a shows the energy spectrum expected during two-tone spectroscopy of a transmon qubit with no topological states and $E_C = 0.8\,\text{GHz}$, $E_J = 4\,\text{GHz}$ and $E_M = 0\,\text{GHz}$. Entering the topological regime and taking $E_M = 0.01\,\text{GHz}$ (Fig. 7.2b), two additional transitions are observed to split off from the normal transmon eigenstates. The low value of E_M means that the matrix elements of these transitions is suppressed and parity conserving transitions are favoured. Further increasing $E_M = 0.2\,\text{GHz}$ (Fig. 7.2c) allows for enough coherent parity mixing that all four transitions are clearly visible. It should be noted that observation of these transitions does not serve as a 'smoking gun' for the observation of MBSs however, as if a pair of Andreev bound states on each side of
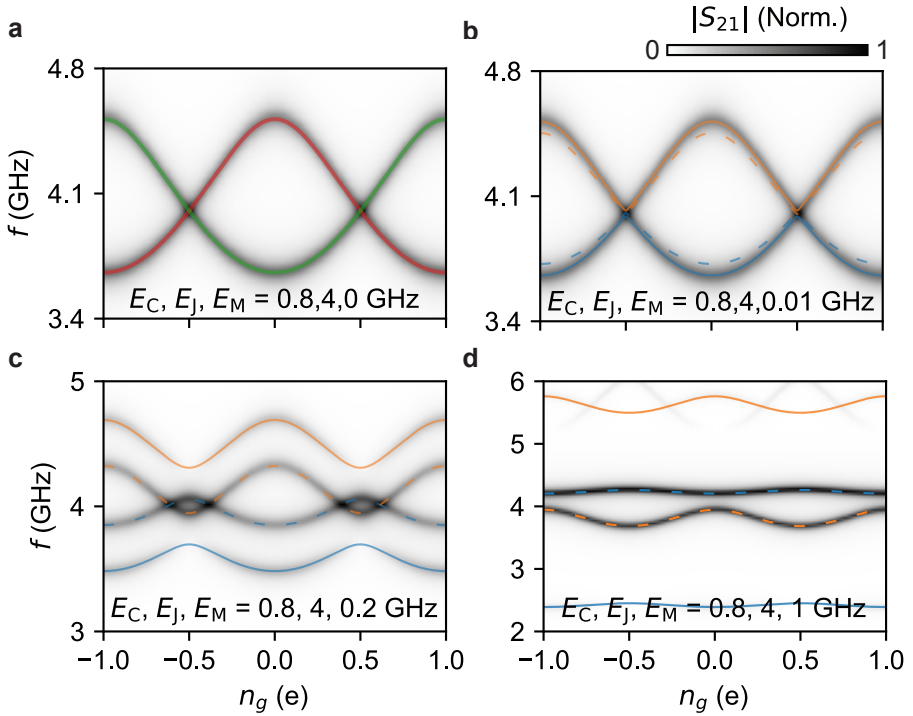
Figure 7.2: Spectroscopy of a Majorana transmon **a** In the trivial state with $E_M = 0\,\text{GHz}$, numerical simulations of the energy spectrum show a charge dispersion consistent with a transmon qubit of low E_J/E_C value, with only transitions that conserve parity visible (solid lines). **b** $E_M = 0.01\,\text{GHz}$ splits the spectrum giving two additional transitions, although the matrix elements of these transitions that do not conserve parity are suppressed (dashed lines). **c** Increasing to $E_M = 0.2\,\text{GHz}$ reveals four distinct transitions, transmon transitions that now do and do not conserve parity. **d** In the case where $E_M = 1\,\text{GHz}$ the parity mixing is so strong that transitions that conserve parity are suppressed. As E_M and E_J are now comparable in magnitude the charge dispersion of the ground state is strongly suppressed.

the JJ were to become energetically aligned similar spectroscopic features would be produced. In this case it would be necessary to perform a series of checks that study the behaviour of these features as a function of magnetic field and gate configuration, as has become standard practice in other studies. For a more detailed theoretical summary please see Sec. 2.6.3.

With numerical simulations suggesting that robust features of a topological phase would be observable over a broad range of E_M, designing and fabricating a transmon qubit with the required parameters, field compatibility and control of the nanowires electrostatic environment became the next challenge. Due to the high coherence times and comparably mature fabrication techniques, InAs nanowires were chosen as the preferred materials system for the development of this detector. Creating a transmon qubit able to survive the magnetic fields where topological states are typically observed ($B_\parallel > 1\,\mathrm{T}$ in InAs nanowires [4]) is no small task however, with previous attempts being limited to below $B_\parallel = 0.1\,\mathrm{T}$ [14]. In an attempt to remedy this, the resonators developed in Chap. 4 were integrated into a transmon circuits with single islands, and fabrication recipes and gate structures developed that allowed for the chemical potential μ inside the wire to be tuned over a large range. The performance of the device was then characterised, first at zero magnetic field where the importance of sufficient radiative shielding is emphasised. A parallel magnetic field is then applied and the device studied at a series of gate configurations where topological phase transitions may be expected to occur. Although no features consistent with MBSs were observed, anomalous spectroscopic measurements of the resonator and qubit were measured and their implications discussed.

7.2. Device overview

7.2.1. Fabrication

To fabricate the devices, the native oxide on 100 mm Si wafers is stripped using HF and a 100 nm layer of low stress SiN_x deposited by LPCVD to prevent leakage between adjacent gates without significantly increasing the losses at microwave frequencies (see supplementary material). The wafer is then cleaned using HNO_3 and a thin 20 nm layer of NbTiN is sputtered in an Ar/N atmosphere. The readout circuit and shunt capacitor that forms the transmon is then patterned using e-beam lithography and etched using reactive ion etching in an SF_6 atmosphere (Fig. 7.3a,b). An InAs/Al nanowire is placed on top of the electrostatic gates using a deterministic deposition technique, and insulated from them using a small window of HfO_x (10 nm) deposited beforehand using ALD (Fig. 7.3c). The JJ is defined above the middle cutter gate via a wet etch (Fig. 7.3c inset) using Transene D to remove the Al shell of the InAs nanowire in a region of length $d \approx 150\,\mathrm{nm}$, shorter than the coherence length of the superconductor, placing the JJ in the short junction limit. A short Ar etch removes the native oxide from the InAs shell, with NbTi/NbTiN sputtered to form the contacts. The device is enclosed inside a light tight copper enclosure, and measured in a dilution refrigerator with a base temperature $T \simeq 20\,\mathrm{mK}$.
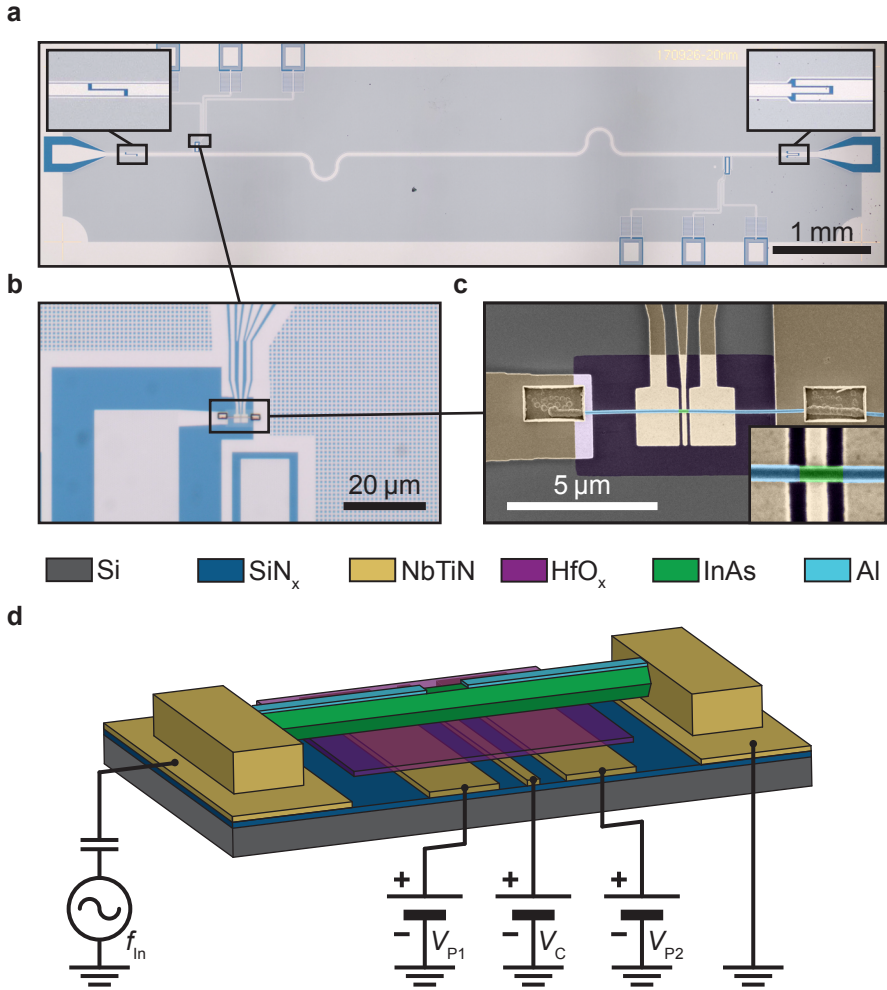
Figure 7.3: Device layout **a** Optical image showing a $\lambda/2$ SC CPW resonator coupled to an input (inset, left) and output port (inset, right). The coupler on the output port has a higher capacitance than the input port, maximising the SNR on the output port. **b** Cropped optical image showing the superconducting island that forms the transmon, and the InAs nanowire that forms a Josephson junction between the island and the ground plane. **c** False colour SEM image of the InAs nanowire. NbTiN contacts connect the Al shell of the nanowire to the SC island and ground. The epitaxial Al shell is etched to form a Josephson junction of $\sim 150\,\text{nm}$ in length (inset). **d** Schematic diagram showing the device layout. The InAs-Al nanowire sits atop ALD HfO_x dielectric that covers the plunger gates that tune the chemical potential and the central finger gate that tunes the transparency of the junction. Each of the gates is connected to an on-chip LC filter that filters out high frequency noise.

7.2.2. Design and measurement

Fig. 7.3a shows an optical microscope image of the $\lambda/2$ SC-CPW resonator that serves as the readout resonator for the transmon qubits. The coupling of the input and output ports (Fig. 7.3a insets) are made strongly asymmetric, such that the rate of photon emission k_i out of the input port (left) is much than the rate of emission out of the k_o output port (right), increasing the SNR. The left and right shunt capacitors ($E_C \simeq 1.2$ GHz and 0.6 GHz respectively) are placed at the electric field anti-nodes of the fundamental resonator mode (Fig. 7.3c), between finger capacitors that maximise coupling to the readout resonator ($g \simeq 100$ MHz). Voltages ($V_{P/C}$) applied to the gates via on-chip low pass filters tune the chemical potential μ and E_J of the wire. The DC voltages are applied using low noise voltage sources and the complex microwave transmission S_{21} measured using standard heterodyne microwave techniques as described in Sec. 5.2.

7.3. Zero field characterisation

7.3.1. Device characterisation

The response of the device is first characterised at base temperature and zero magnetic field. The readout resonator is driven with a continuous wave tone at the bare resonator frequency $f_{Bare} = 5.517$ GHz with an input power P_{in} sufficient to occupy the readout resonator with a single photon ($\langle n_{ph} \rangle \simeq 1$), and $V_{P_{1,2}}$ varied until a change in S_{21} is measured. Once this occurs, the readout tone f can be varied as a function of P_{in} to vary $\langle n_{ph} \rangle$ of the resonator from 1 to $\sim$1000, where a shift in the resonator frequency f_r of magnitude χ from the f_{Bare} is observed (see Fig. 7.12a for a representative measurement). This occurs due to the Jaynes-Cummings interaction between the harmonic readout resonator and a non-linear element in the circuit, in this case the Josephson junction (JJ) in the transmon. Monitoring S_{21} with $\langle n_{ph} \rangle \simeq 1$ as f and $V_{P_{1,2}}$ is varied (Fig. 7.4b) shows $V_{P_{1,2}}$ can tune the Josephson energy E_J of the JJ as expected. Several other anomalous states are observed to couple to the resonator, coming in and out of resonance and adding additional modes with their own χ values. These unwanted anomalous features were significantly more present in previous measurements where the device was not appropriately shielded (see supplementary material), reinforcing the importance of appropriate shielding for cQED devices.

Performing two-tone spectroscopy as a function of $V_{P_{1,2}}$ (Fig. 7.4c,d) shows two clear peaks corresponding to the f_{01} and $f_{02}/2$ transitions. The repeatable, non-monotonic dependence on $V_{P_{1,2}}$ is consistent with universal conductance fluctuations that have been observed in similar devices with SNS JJs [12, 13, 21]. In addition, the measured anharmonicity $\alpha = h(f_{12} - f_{01}) \sim 400$ MHz is moderately suppressed from the expected value of $\alpha \simeq -E_C \simeq -600$ MHz, suggesting that the JJ is in the few mode high transparency limit [22] which can reduce α to as little as $E_C/4$.
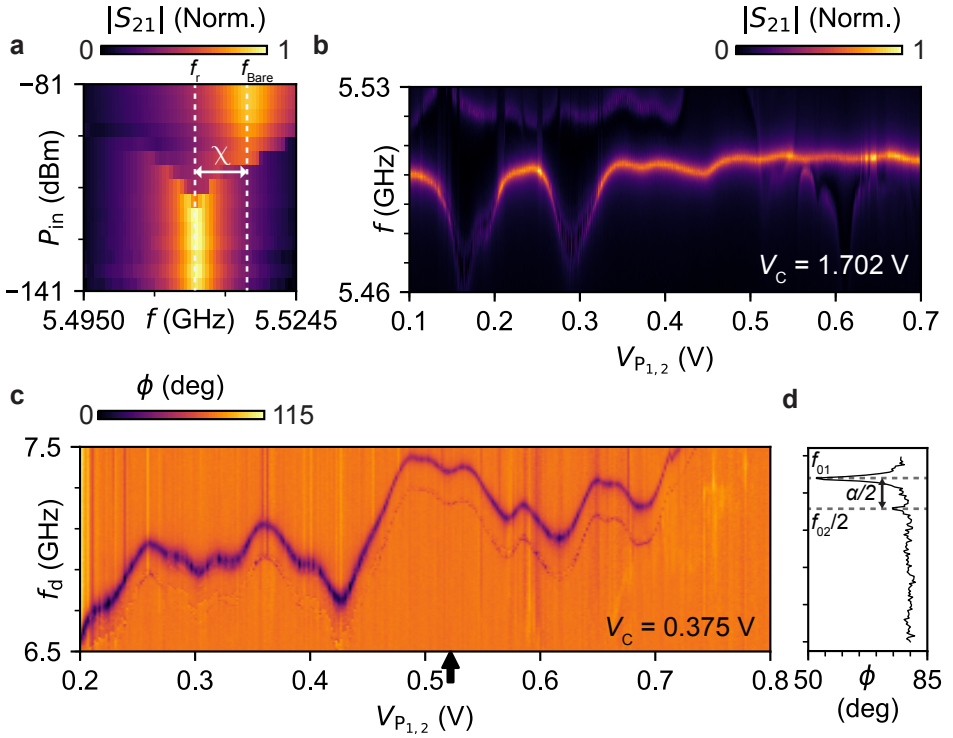
Figure 7.4: Device characterisation **a** Monitoring $|S_{21}|$ (Norm.) as a function of f versus P_{in}. As P_{in} is reduced, at single photon occupancy the f_r experiences a dispersive shift χ from f_0 due to coupling to a transmon transition above the resonator. **b** Monitoring $|S_{21}|$ (Norm.) as f and V_C is varied demonstrates χ is tuneable, with additional features moving in and out of resonance with f_r. **c** Monitoring ϕ of S_{21} at f_r as f_d and V_C are varied in a reduced range reveals the fundamental f_{01}, and two photon $f_{02}/2$ transitions, as well as the additional anomalous features that can be seen crossing f_r in b. **d** Line trace at black arrow in c of ϕ of S_{21} vs f_d shows two sharp peaks corresponding to the f_{01} and $f_{02}/2$ transitions.

7.3.2. Time domain response

To determine the time domain response of this device, three separate quantities were characterised using the pulse sequences detailed in Fig. 7.5: the relaxation time T_1, the coherence time T_2^* and the echoed coherence time T_2^E both before and after the additional shielding was put in place. Fig. 7.5a shows T_1 and T_2^*, with T_1 being extended significantly and T_2^* showing a small increase, although it should be noted that the measurement of T_2^* required an order of magnitude more averaging when unshielded. Measurements of T_2^E that were not possible in the unshielded case show an enhancement of the coherence time by the echo process, indicating that the coherence is limited by low frequency noise.

7.4. Magnetic field dependence

To determine the suitability of the system as a sensor for probing MBSs, the response of the device was monitored as the applied parallel magnetic field $B_\parallel$ was gradually increased.

7.4.1. Qubit frequency, relaxation and coherence

Fig. 7.6a shows the response of f_{01} as a function of $B_\parallel$ at two different gate configurations. As in previous studies, f_{01} is seen to drop parabolically in $B_\parallel$ suggesting that the reduction in f_{01} is due to a reduction in the superconducting gap Δ. We fit the trend with the formula $f_{01}(B_\parallel) \approx f_{01}(B_\parallel = 0\,\text{T})(1 - (\frac{B_\parallel}{B_C})^2)^{\frac{1}{4}}$ that uses BCS theory to relate the reduction in E_J to a suppression of Δ by $B_\parallel$ [14]. The B_Cs extracted is significantly higher than previous measurements [14], presumably due to the Al covering only two facets of the wire, although these values are known to fluctuate from sample to sample. In contrast T_1 appears to increase as a function of $B_\parallel$ (Fig. 7.6b). This is unusual, given that suppression of Δ is usually associated with a softening of the gap. That, in combination with the increased generation of quasiparticles would be expected to reduce T_1 as a function of $B_\parallel$. However, if T_1 is instead plotted as a function of f_{01} (Fig. 7.6c) it can be seen that it is relatively independent of f_{01}, although at higher frequencies T_1 becomes limited by another, undiagnosed process. As f_{01} is still far from the second harmonic of f_r, enhancement of the relaxation time via the Purcell effect seems unlikely [11]. Instead, the most likely candidate is dielectric induced losses which start to dominate above $f \sim 6.5\,\text{GHz}$ and increase with f [14]. Further experiments would be required to confirm this and identify whether the losses occur due to the HfO_x or SiN_x layer.
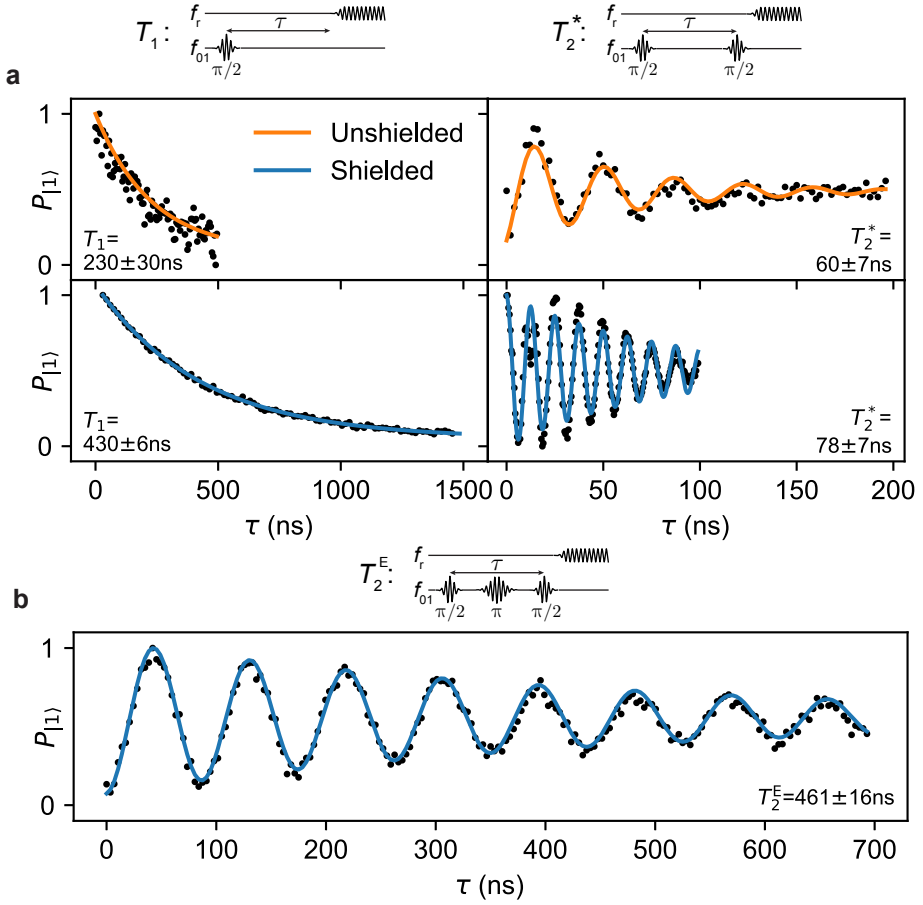
Figure 7.5: Time domain measurements **a** T_1 measurements of the qubit show that the relaxation time is extended by appropriate shielding, although T_2^* measurements of the coherence are not significantly affected. **b** T_2^E suggest that the coherence of the device is mostly limited by slow noise.

Figure 7.6: Qubit properties in a parallel magnetic field **a** Extracted f_{01} versus $B_\parallel$ at two different V_C, V_P settings. Black lines correspond to fits that estimate B_C of the superconductor from the reduction in f_{01} using BCS theory. **b** Measured T_1 versus $B_\parallel$. **c** Measured T_1 versus extracted f_{01}.

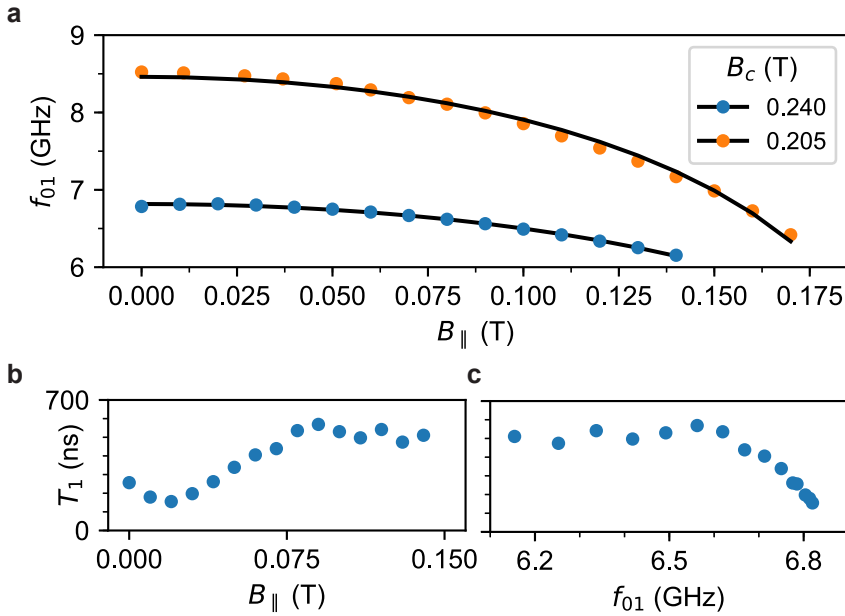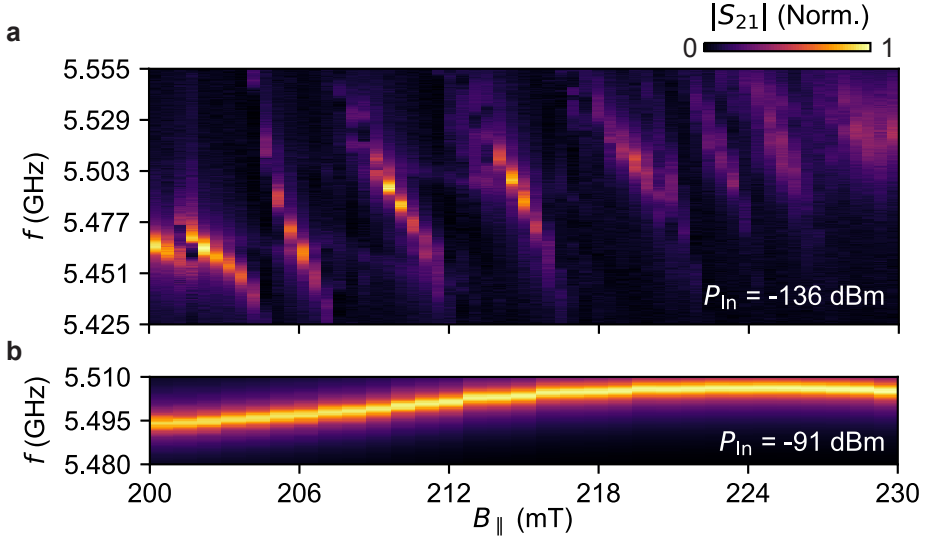Figure 7.7: Anomalous low power transitions **a** $|S_{21}|$ (Norm.) as a function of f versus $B_{\parallel}$ at $\langle n_{\mathrm{ph}}\rangle \simeq 1$ reveals multiple anomalous level crossings, possibly indicative of hyperfine splitting of a free electron spin resonance. **b** $|S_{21}|$ (Norm.) as a function of f versus $B_{\parallel}$ at $\langle n_{\mathrm{ph}}\rangle \simeq 1000$ shows that these additional level splittings are not present in the resonator, indicating it is a unique feature of the transmon circuit.

7.4.2. Anomalous low-power anticrossings

Above $B_{\parallel} \geq 175\,\mathrm{mT}$, the reduction in f_{01} results in an anti-crossing with f_r which is accompanied by significant broadening of the the qubit linewidth, preventing further investigation of the time domain properties of the qubit and in some cases preventing identification of the qubit transition entirely. Monitoring $|S_{21}|$ (Norm.) in the single photon regime ($\langle n_{\mathrm{ph}}\rangle \simeq 1$) as $B_{\parallel}$ was increased from 200 mT to 230 mT reveals multiple anti-crossings with f_r where one would normally be expected (Fig. 7.7a). A similar measurement of $|S_{21}|$ (Norm.) at high power (Fig. 7.7b) shows no such effect, suggesting that the observed behaviour occurs only due to interactions with the transmon circuit itself and not the resonator. The fact that each anti-crossing is well resolved also indicates that the resonator is strongly coupled to each transition as it passes through the resonator ($g_c > \kappa, \gamma$). The origin of these transitions is puzzling; it could be due to a finite population of the higher modes of the resonator, but this would require a huge population in > 8 modes and thanks to the shielding improvements discussed in Sec. 7.7.3 we know this population inversion cannot be due to thermal excitation. The data is also strongly reminiscent of results where superconducting resonators are coupled to spin ensembles [23–25]. In these experiments, the Zeeman transition is split by hyperfine interactions with the nuclear spin into several levels, resulting in multiple anticrossings with the resonator. In these cases, the extremely low coupling of single spins to the cavity mode ($g_c/2\pi \sim 10\,\mathrm{Hz}$ in [23, 24]) mean that strong coupling can only achieved by coupling to large ensembles of N spins ($g_{\mathrm{ens}} \propto \sqrt{N}g$). Considering this possibil-
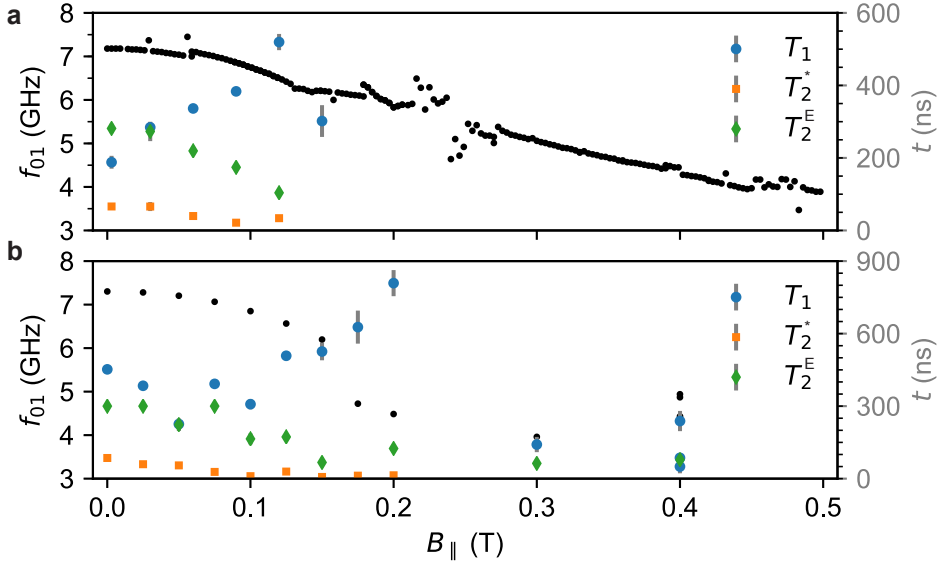
Figure 7.8: Qubit response at high magnetic fields **a** Double axis plot of f_{01} and T_1, T_2^* and T_2^E versus $B_\parallel$ at $V_C = 0.375$ V, $V_P = 0.3$ V. **b** Same as in a, but with $V_C = 1.8$ V, $V_P = 0.4$ V.

ity, we note that the large number of split levels necessitates an atom with a high nuclear spin, with the naturally abundant isotope used in the nanowires ^{115}In providing a possible candidate (9/2). It is possible that these nuclear states couple to paramagnetic impurities adsorbed on the nanowire surface, splitting the electron spin resonance into multiple levels [26, 27]. To confirm this, the full level structure should be modelled and resolved, requiring measurements of multiple cavity modes over a much broader magnetic field than we have access to here (as in [23]).

7.4.3. Time domain response

On two separate cooldowns with two different gate configurations, f_{01}, T_1, T_2^* and T_2^E were tracked as function of $B_\parallel$. In Fig. 7.8a the gate configuration is held at $V_C = 0.375$ V, $V_P = 0.3$ V and $B_\parallel$ reduced from $B_\parallel = 0.5$ T to 0 T. f_{01} versus $B_\parallel$ shows a parabolic lineshape below $B_\parallel \sim 0.12$ T, after which it decreases linearly until $B_\parallel = 500$ mT. T_1 was found to maximise at $B_\parallel \sim 0.12$ T, whereas T_2^* and T_2^E were maximised at $B_\parallel \sim 0$ T, decreasing with increasing $B_\parallel$. Above $B_\parallel \sim 0.15$ T, T_1 and T_2^* became too short to measure. Fig. 7.8b shows a second measurement with a gate configuration of $V_C = 1.8$ V, $V_P = 0.4$ V where a qubit revival was observed after $B_\parallel \sim 0.3$ T. The presence of gate dependent minima in f_{01} versus $B_\parallel$ can be understood as a result of $B_\parallel$ and the strong spin orbit interaction present in InAs wires modifying the interference conditions of the few highly transmitting channels [28] typical of these InAs JJs [29].

Although these lifetimes are not long when compared to modern superconducting qubits, the fact that the qubit is measurable and can be coherently ma-
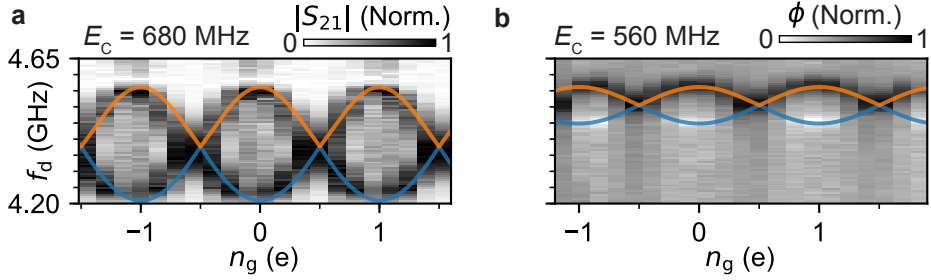
Figure 7.9: Charging energy suppression in charge dispersions **a** Two-tone spectroscopy of f_{01} as a function of n_g at $V_C = 0.16\,V$. Theoretical modelling can reproduce the observed data by taking $E_C = 680\,MHz$. **b** Repeating the measurement at $V_C = 0.133\,V$ shows a charge dispersion that can only by modelled by taking a significantly suppressed $E_C = 560\,MHz$.

nipulated up to $B_\parallel \sim 0.4\,T$ is almost an order of magnitude improvement over previous experiments that used 'full-shell' Al-InAs nanowires with lower field compatibility. Subsequent results from our collaborators in nominally identical devices [30] demonstrate narrow linewidths and qubit coherence at $B_\parallel = 1\,T$, suggesting the platform is well suited to probe for signatures of MBSs using spectroscopic techniques (see Fig. 7.15).

7.5. Charge dispersion suppression at high T

As described in Sec. 7.1, inducing a topological state in the wire by tuning μ and B should result in a set of unique signatures in the charge dispersions measured via two-tone spectroscopy due to coherent single electron coupling between adjacent MBSs. With this aim in mind, the charge dispersion of the transmon energy levels were measured over a large range of V_C, V_G and $B_\parallel$ as possible in multiple devices by this collaboration. Unfortunately to date, no signatures of MBSs have been observed in the measured charge dispersions.

Interestingly however, charge dispersion measurements in high magnetic fields were regularly found to be anomalous. Small changes in V_C could produce large changes in the observed anharmonicity $\alpha = f_{12} - f_{01}$ as well as significantly change the width of the charge dispersions at nominally identical qubit frequencies, an effect not predicted in SIS transmons. A recent experiment observed significant suppression of α when E_J is defined by a small number of channels with transmission $T \to 1$. This results in a modification of the Josephson potential, suppressing the anharmonicity of the levels and suppressing α as [22]:

$$\alpha \approx -E_C \left(1 - \frac{3 \sum T_i^2}{4 \sum T_i} \right) \tag{7.2}$$

An effect related to this, predicted in 1999 but to date not yet observed is that in the single channel limit as $T \to 1$ Coulomb blockade on the island and thus the charge dispersion of the level structure should become completely suppressed. In the single channel limit, when $T = 1$ for the Andreev bound state (ABS) that

carries the JJs supercurrent, the reflection that couples separate charge states and allows the junction to relax to the ground state when the n_g is varied is completely suppressed. This takes the junction out of the adiabatic limit, effectively resulting in Landau-Zener like transitions as $T \to 1$, suppressing the charge dispersion of the level structure [31] (for a more detailed theoretical summary see Sec. 2.6.1).

Fig 7.9a shows a measured charge dispersion of the f_{01} transition at $V_C = 0.16\,V$. To correctly model this dispersion it is necessary to diagonalise the CPB Hamiltonian taking an $E_C = 680\,MHz$ which matches the value predicted by electrostatic simulations. In contrast, reducing the cutter voltage a few mV to $V_C = 0.133\,V$ reveals an f_{01} transition at roughly the same frequency but with a significantly suppressed charge dispersion. In this case correctly modelling the charge dispersion requires an $E_C = 560\,MHz$, a moderate reduction in α.

To ascertain whether this process could be due to effective Landau-Zener tunnelling from the Averin model, a large number of charge dispersions were taken over a range of gate configurations and f_{01} values. As the measurements were performed above the resonator, the charge dispersion of the f_{01} transition was generally smaller than the qubit linewidth. Instead, the dispersion of the level structure is extracted from the $f_{02}/2$ transition. For each f_{01} transition, the charge dispersion of the $f_{02}/2$ transition was extracted using a peak finding and binning procedure (Fig 7.10a inset) and plotted as a black point on Fig 7.10a. For a given superconducting gap Δ, f_{01} and the dispersion of $f_{02}/2$ was calculated and plotted using an ABS model with two channels of transmission T_1, T_2 varying from 0 to 1 (Fig 7.10a, red points, colour scale represents highest T). An extension of the Averin theoretical model [31] to the two channel limit was then used to calculate the expected $f_{02}/2$ dispersion for a given f_{01} allowing for suppression of the charge dispersion by Landau-Zener transitions (Fig 7.10a, blue points).

Zooming in on the region with the measured dispersions (Fig 7.10b) shows that the dispersion in some of the transitions appears so suppressed that they cannot be modelled without Landau-Zener transitions. The sensitivity of the model to the assumed Δ sheds doubt on this conclusion however, as setting Δ to 45 GHz (Fig 7.10c) or 45 GHz (Fig 7.10d) changes the allowed solution space considerably. Without leads to perform tunnelling spectroscopy on the device, an accurate determination of Δ is not possible in this geometry, and is significantly complicated by the fact that Δ is known to vary considerably as a function of magnetic field [4, 32] and gate [33]. In addition, although the number of channels and their transmissions can be roughly estimated by fitting the level structure with the Andreev Hamiltonian [22], a more accurate method would involve embedding the nanowire JJ into a DC SQUID with an SIS junction of high E_J value, allowing the device to be phase biased and the number of channels and their transmissions to be extracted from the current phase relations [29].

7.6. Conclusion

Although no signatures of MBSs were observed, the results in this chapter paint a promising picture for the integration and detection of MBSs in microwave superconducting devices. The fabrication techniques developed allow for InAs nanowire
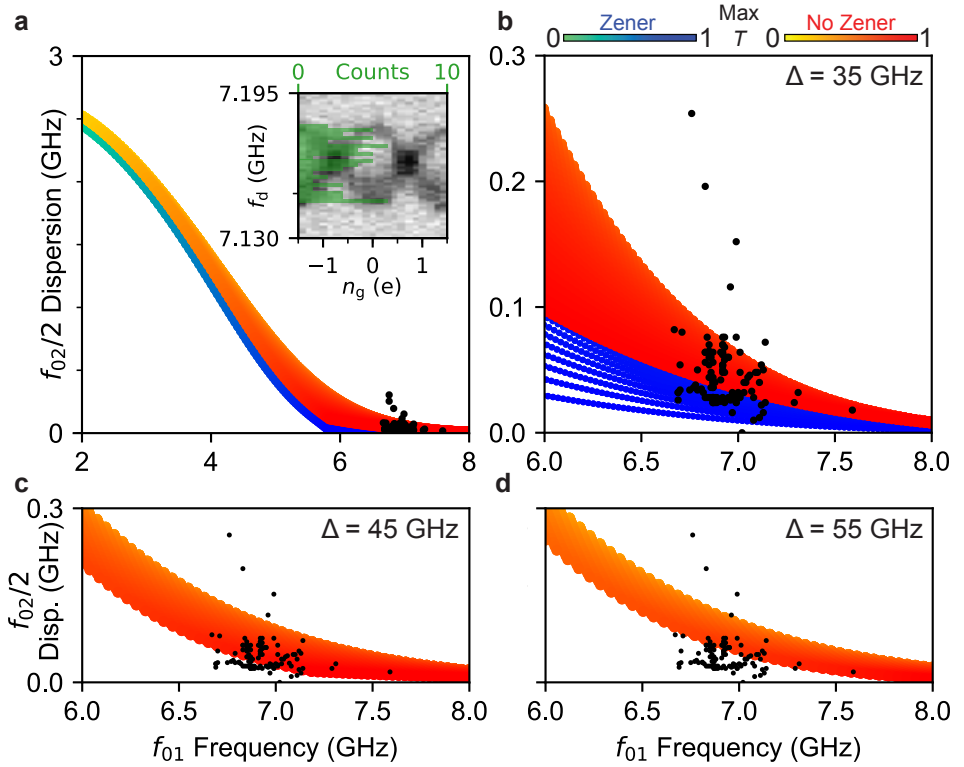
Figure 7.10: Charge dispersion suppression **a** Solutions to a two channel Averin model places bounds on the allowed charge dispersion in the f_{02} transition at a given f_{01}, with the maximum T of the two channels represented by the colour. Red and blue points correspond to possible solutions with and without Landau-Zener tunnelling respectively. Inset is an example charge dispersion, where a peak finding and binning routine is used to extract the dispersion from the $f_{02}/2$ transition. **b** Zooming in to view the extracted dispersions shows that numerous points fall outside the red region, suggesting that Landau-Zener tunnelling into excited branches of the ABS may be responsible for some of the observed charge dispersion suppression. **c,d** Performing the same calculation with different values for Δ without Landau-Zener tunnelling shows that the bounds of allowed dispersions can be shifted significantly depending on the value of Δ taken.

transmons with gates that extend over the length of the wire, allowing for n_{g} and μ to be varied over a large range while maintaining qubit coherence. The qubit was characterised in a magnetic field, and found to survive up to 400 mT (1 T in the device of our collaborators), an order of magnitude higher than previous experiments. Anomalous resonator spectroscopy and charge dispersion measurements are suggestive of interesting, previously unmeasured mesoscopic effects that may be of importance for future cQED devices based on InAs JJs, warranting further investigations so that future devices that attempt to observe topological effects behave predictably.
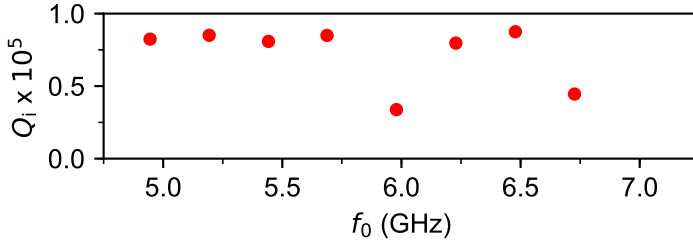
7

Figure 7.11: Intrinsic quality factors of 8 $\lambda/4$ resonators fabricated on intrinsic Si substrates with 100 nm of SiN$_x$ dielectric below the NbTiN film. Although quality factors are not as high as in the other chapters of this thesis, they are sufficient to meet the requirements of this experiment.

7.7. Supplementary material

7.7.1. Radiative excitation

Initial measurements on this device suggested that the qubit was subject to significant radiative excitation. Monitoring S_{21} with $\langle n_{\text{ph}} \rangle \simeq 1$ as f and V_C is varied (Fig. 7.12b) shows that although V_C can tune the Josephson energy E_J of the JJ as expected, many additional states appear to couple to the resonator, coming in and out of resonance and adding additional modes with their own χ values. In two-tone spectroscopy three peaks (Fig. 7.12d) were observed, most likely corresponding to the f_{01}, f_{12} and $f_{02}/2$ transitions, as well as other states that appear to approach and then move away from the transmon transitions. The broad line-shapes, multiple extra states and residual excitation of the f_{01} strongly suggest that the sample is not in thermal equilibrium with the base temperature of the fridge.

7.7.2. Three-tone measurements

To investigate this further, three-tone spectroscopy was performed where in addition to the readout (f) and drive (f_{d_1}) tones, a third tone (f_{d_2}) is used to coherently drive between multiple energy levels. Fig. 7.13 shows how the amplitude (a) and phase (b) of S_{21} varies at f_r as f_{d_1} and f_{d_2} are swept. Taking the linecut in Fig. 7.13a,b at $f_{d_2} = 7.4$ GHz corresponds to the case where f_{d_2} is detuned from a transition, making the process effectively equivalent to the two-tone case. Here the f_{01} and f_{12} transitions are driven by single photon processes and marked with black lines. Green lines denote two photon processes, whereby the f_{02} (or f_{13}) transitions can be driven by photons that are themselves off-resonant with the individual transitions via a virtual state. Measuring at higher power over a broader range of f_d (Fig. 7.13c,d) allows two photon transitions to be driven via single tone, with the $f_{02}/2$ and $f_{13}/2$ transitions denoted as vertical green lines. Noticeably the $E_J/E_C \simeq 13$ is sufficiently low that the charge dispersion can be resolved as a parity dependent splitting in the $f_{02}/2$ transitions.

Driving of the f_{12} and $f_{12}+f_{23}$ transitions may only occur with a significant population in first excited state. This is unusual, as at $T = 20$ mK, a thermal distribution would provide a residual excitation into the first excited state of $p_1 = e^{hf_{01}/k_B T} \simeq$
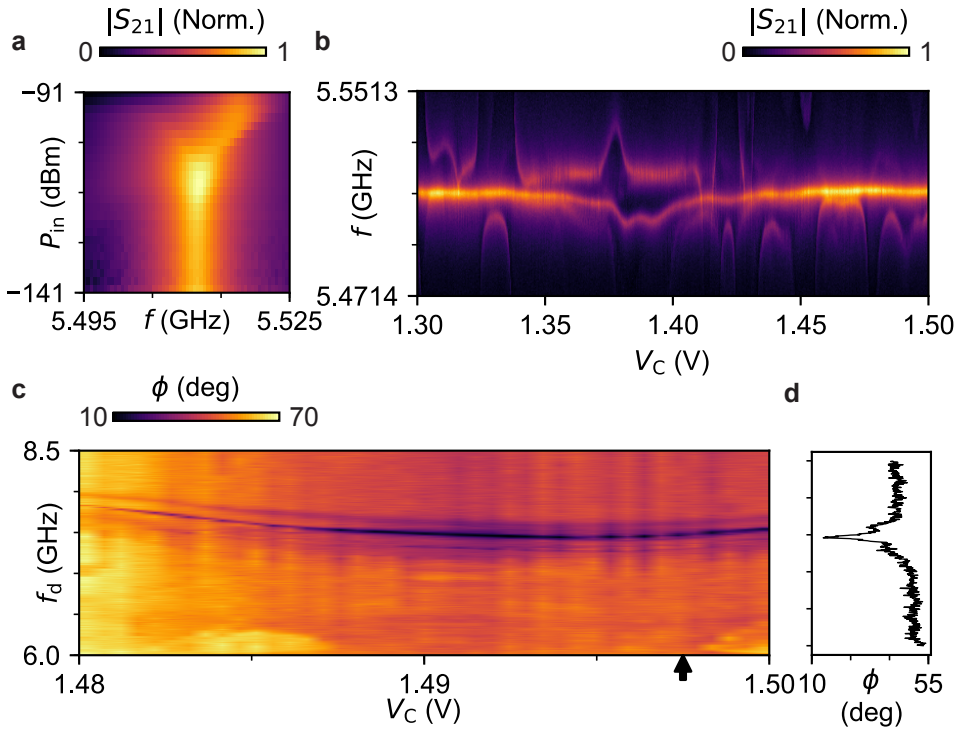
Figure 7.12: Device characterisation **a** Monitoring $|S_{21}|$ (Norm.) as a function of f versus P_{in}. As P_{in} is reduced, at single photon occupancy the f_r experiences a dispersive shift χ from f_0 due to coupling to a transmon transition above the resonator. **b** Monitoring $|S_{21}|$ (Norm.) as f and V_C is varied demonstrates χ is tuneable, with additional features moving in and out of resonance with f_r. **c** Monitoring ϕ of S_{21} at f_r as f_d and V_C are varied in a reduced range reveals a broad spectrum of transitions, most likely corresponding to the f_{01}, f_{12} and $f_{02}/2$ processes. The additional anomalous features seen in b also appear to move in and out of resonance. **d** Line trace at black arrow in c of ϕ of S_{21} vs f_d showing the 3 sharp peaks that correspond to f_{01}, f_{12} and $f_{02}/2$ processes.
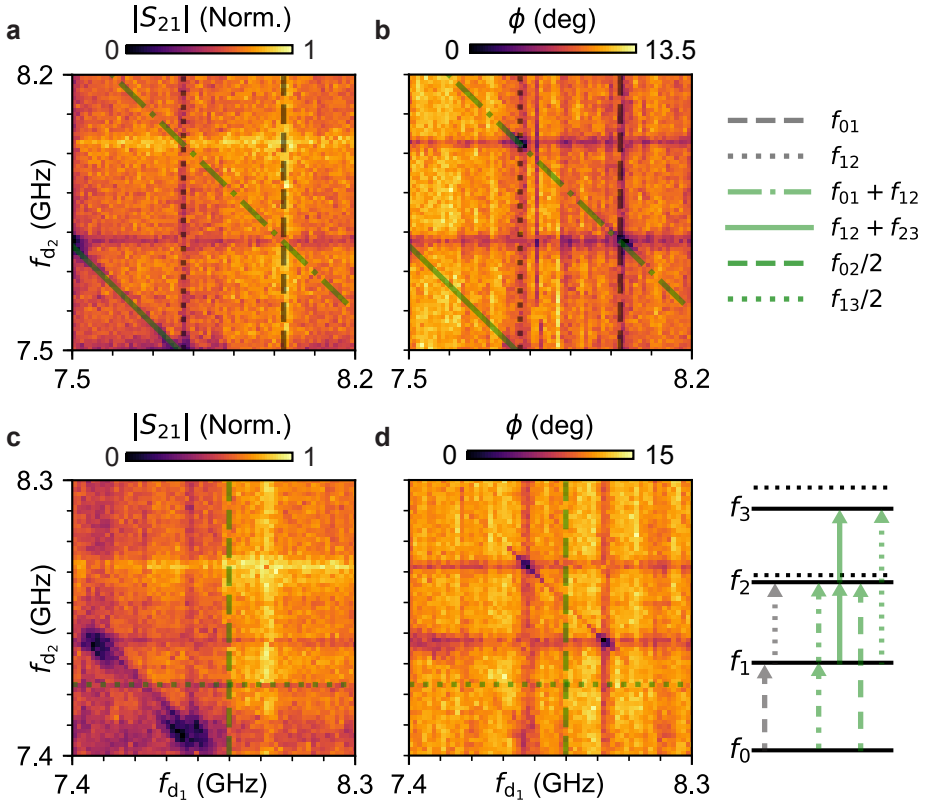
Figure 7.13: Three-tone measurements **a,b** Monitoring $|S_{21}|$ (Norm.) and ϕ as f_{d_1} and f_{d_2} are varied reveals the level structure expected of a transmon qubit. Black lines correspond to a single photon process, whereas green lines correspond to a two photon process. The visibility of f_{12} and $f_{12} + f_{23}$ implies a significant residual excitation. **c,d** Measuring at higher drive power over a broader frequency range shows additional two-photon processes such as $f_{02}/2$ and $f_{13}/2$ that are typically suppressed.

10^{-9}. The presence of non-equilibrium quasiparticles has been studied for some time [34, 35], with efforts to reduce them principally focussing on improved thermalisation and radiative shielding [36].

7.7.3. Radiative shielding

In an effort to reduce radiative excitation, we first consider the current shielding setup in the Oxford Triton 400 dilution refrigerator in Fig. 7.14a. When comparing this setup to other groups that perform similar measurements on superconducting qubits [13, 37] it can be immediately noticed that in our schematic we are missing both copper and Al shields that would protect our sample from thermal radiation emitted by the 700 mK and 100 mK plates. This is due to the fact that our setup has a fast sample exchange system, consisting of a 'puck' that can be exchanged while the fridge is cold using a loading lock and loading arm. This system significantly reduces the downtime during sample exchange, but at the cost that some internal shields were removed by the manufacturer and the brass 'puck' and loading flaps between the stages are not entirely light tight, potentially allowing thermal radiation from the upper stages to radiatively excite our qubit.

To compensate for this, we envelope the sample inside the puck in multiple layers of shielding to reduce IR and microwave frequency thermal radiation (see Fig. 7.14b). The sample is first enclosed inside a milled copper box, then wrapped in microwave absorbing foam (non magnetic Eccosorb, see Fig. 7.14c), then a layer of copper film then another layer of foam. The inside of the puck and sample holder is also coated with microwave absorbing foam to suppress any microwave resonances that might occur in the brass cavity created by the puck (Fig. 7.14d).

7
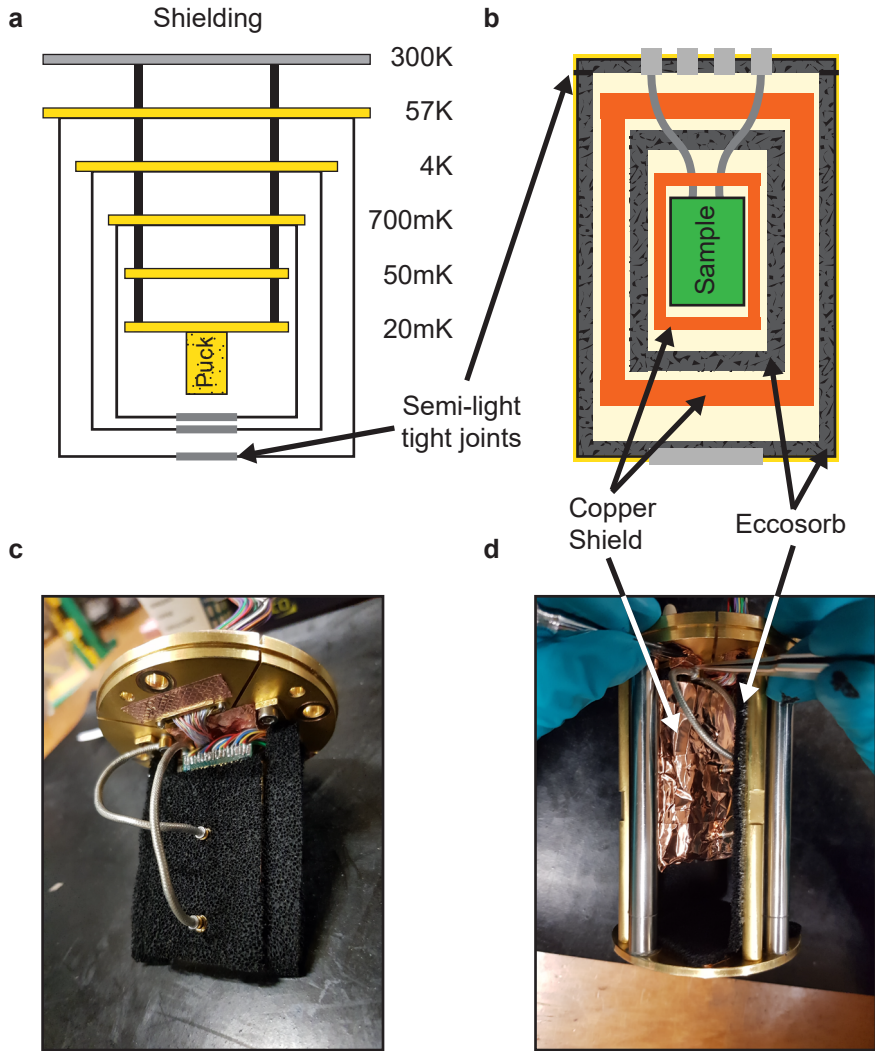
Figure 7.14: Device shielding **a** Schematic of the different cold plates in an Oxford Triton 400 dilution refrigerator. The coldest radiative shield that the sample puck sees is at 700 mK and is not light tight. **b** In order to reduce radiative excitation, the pucks are rendered as light tight as possible and our samples are enclosed in successive layers of copper and Eccosorb shielding to absorb the infrared and microwave radiation from warmer cooling stages. **c,d** Optical image of sample board attached to the top plate of the puck, enclosed in the layers of copper and Eccosorb shielding.
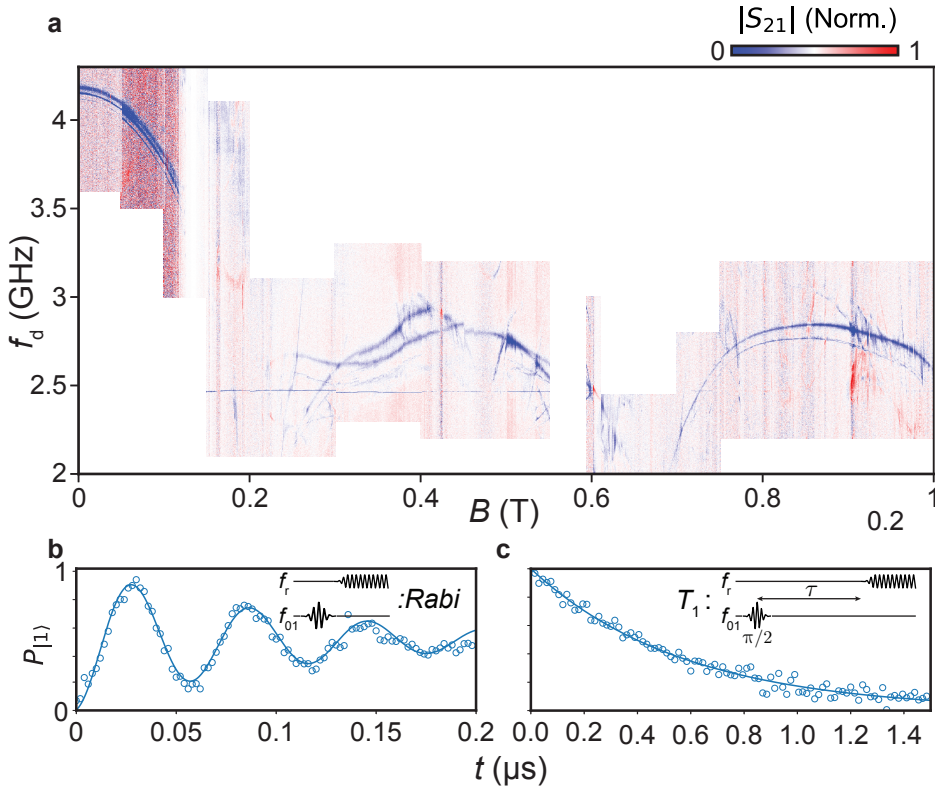
Figure 7.15: Field dependence and high field coherence in a second device **a** Two tone-spectroscopy as a function of $B_\parallel$ shows the the f_{01} and $f_{02}/2$ transitions reducing parabolically at small fields. The qubit revives above 0.2 T with multiple transitions oscillating together producing a rich level structure. Initial analysis suggests that this is due to qubit interactions with two Andreev bound states, with one of them strongly dispersing, but further experiments are needed to confirm this. The qubit then drops in frequency, before reviving again above 0.2 T in a distinct 'lobe' like structure where f_{01} and $f_{02}/2$ can again be resolved up to 1 T. **b** At $B_\parallel = 1$ T, the qubit is still coherent, with Rabi and T_1 measurements **c** still possible. Adapted from [30].

References

[1] Mourik, V. *et al.* Signatures of majorana fermions in hybrid superconductor-semiconductor nanowire devices. *Science* **336**, 1003–1007 (2012).

[2] Deng, M. T. *et al.* Observation of Majorana Fermions in a Nb-InSb Nanowire-Nb Hybrid Quantum Device. *Nano Letters* **12**, 6414–6419 (2012).

[3] Das, A. *et al.* Zero-bias peaks and splitting in an Al–InAs nanowire topological superconductor as a signature of Majorana fermions. *Nature Physics* **8**, 887–895 (2012).

[4] Chang, W. *et al.* Hard gap in epitaxial semiconductor–superconductor nanowires. *Nature Nanotechnology* **10**, 232–236 (2015).

[5] Krogstrup, P. *et al.* Epitaxy of semiconductor–superconductor nanowires. *Nature Materials* **14**, 400–406 (2015).

[6] Gazibegovic, S. *et al.* Epitaxy of advanced nanowire quantum devices. *Nature* **548**, 434–438 (2017).

[7] Gül, Ö. *et al.* Ballistic Majorana nanowire devices. *Nature Nanotechnology* **13**, 192–197 (2018).

[8] Zhang, H. *et al.* Quantized Majorana conductance. *Nature* **556**, 74–79 (2018).

[9] Alicea, J., Oreg, Y., Refael, G., von Oppen, F. & Fisher, M. P. A. Non-Abelian statistics and topological quantum information processing in 1D wire networks. *Nature Physics* **7**, 412–417 (2011).

[10] Hyart, T. *et al.* Flux-controlled quantum computation with Majorana fermions. *Physical Review B* **88**, 1–17 (2013).

[11] Koch, J. *et al.* Charge-insensitive qubit design derived from the Cooper pair box. *Physical Review A* **76**, 042319 (2007).

[12] De Lange, G. *et al.* Realization of microwave quantum circuits using hybrid superconducting-semiconducting nanowire Josephson elements. *Physical Review Letters* **115**, 127002 (2015).

[13] Larsen, T. W. *et al.* Semiconductor-nanowire-based superconducting qubit. *Physical Review Letters* **115**, 127001 (2015).

[14] Luthi, F. *et al.* Evolution of nanowire transmon qubits and their coherence in a magnetic field. *Physical Review Letters* **120** (2018).

[15] Van Woerkom, D. J. *et al.* Microwave spectroscopy of spinful Andreev bound states in ballistic semiconductor Josephson junctions. *Nature Physics* **13**, 876–881 (2017).

[16] Hays, M. *et al.* Direct Microwave Measurement of Andreev-Bound-State Dynamics in a Semiconductor-Nanowire Josephson Junction. *Physical Review Letters* **121**, 047001 (2018).

[17] Tosi, L. *et al.* Spin-orbit splitting of Andreev states revealed by microwave spectroscopy (2018). 1810.02591.

[18] Ginossar, E. & Grosfeld, E. Microwave transitions as a signature of coherent parity mixing effects in the Majorana-transmon qubit. *Nature Communications* **5**, 4772 (2014).

[19] Hassler, F., Akhmerov, A. R. & Beenakker, C. W. J. The top-transmon: a hybrid superconducting qubit for parity-protected quantum computation. *New Journal of Physics* **13**, 095004 (2011).

[20] Yavilberg, K., Ginossar, E. & Grosfeld, E. Fermion parity measurement and control in Majorana circuit quantum electrodynamics. *Physical Review B* **92**, 075143 (2015).

[21] Kroll, J. G. *et al.* Magnetic field compatible circuit quantum electrodynamics with graphene Josephson junctions. *Nature Communications* **9**, 4615 (2018).

[22] Kringhøj, A. *et al.* Anharmonicity of a superconducting qubit with a few-mode Josephson junction. *Physical Review B* **97**, 060508 (2018).

[23] Ranjan, V. *et al.* Probing dynamics of an electron-spin ensemble via a superconducting resonator. *Physical Review Letters* **110**, 067004 (2013).

[24] Bienfait, A. *et al.* Controlling spin relaxation with a cavity. *Nature* **531**, 74–77 (2016).

[25] de Graaf, S. E. *et al.* Direct Identification of Dilute Surface Spins on Al2O3: Origin of Flux Noise in Quantum Circuits. *Physical Review Letters* **118**, 057703 (2017).

[26] Samkharadze, N. *et al.* High-Kinetic-Inductance Superconducting Nanowire Resonators for Circuit QED in a Magnetic Field. *Physical Review Applied* **5**, 044004 (2016).

[27] Kroll, J. G. *et al.* Magnetic field resilient superconducting coplanar waveguide resonators for hybrid cQED experiments (2018). 1809.03932.

[28] Zuo, K. *et al.* Supercurrent Interference in Few-Mode Nanowire Josephson Junctions. *Physical Review Letters* **119**, 187704 (2017).

[29] Hart, S. *et al.* Current-phase relations of InAs nanowire Josephson junctions: from interacting to multi-mode regimes (2019). 1902.07804.

[30] Larsen, T. W. *Mesoscopic Superconductivity towards Protected Qubits.* Ph.D. thesis, University of Copenhagen (2018).

7

[31] Averin, D. V. Coulomb Blockade in Superconducting Quantum Point Contacts. *Physical Review Letters* **82**, 3685–3688 (1999).

[32] Gül, Ö. *et al.* Hard Superconducting Gap in InSb Nanowires. *Nano Letters* **17**, 2690–2696 (2017).

[33] de Moor, M. W. A. *et al.* Electric field tunable superconductor-semiconductor coupling in Majorana nanowires. *New Journal of Physics* **20**, 103049 (2018).

[34] Martinis, J. M., Ansmann, M. & Aumentado, J. Energy Decay in Superconducting Josephson-Junction Qubits from Nonequilibrium Quasiparticle Excitations. *Physical Review Letters* **103**, 097002 (2009).

[35] de Visser, P. J. *et al.* Number Fluctuations of Sparse Quasiparticles in a Superconductor. *Physical Review Letters* **106**, 167004 (2011).

[36] Barends, R. *et al.* Minimizing quasiparticle generation from stray infrared light in superconducting quantum circuits. *Applied Physics Letters* **99**, 113507 (2011).

[37] Bruno, A. *et al.* Reducing intrinsic loss in superconducting resonators by surface treatment and deep etching of silicon substrates. *Applied Physics Letters* **106**, 182601 (2015).

7

8

Conclusion

In this concluding section we summarise the important results from each chapter, discuss possible improvements that could be made to the experiment and suggest possible avenues for further research.

Chapter 4

In this chapter, constriction of the device geometry and artificial vortex pinning sites were investigated to control and mitigate the negative effects that Abrikosov vortices have on superconducting (SC) co-planar waveguide (CPW) resonators in magnetic fields. Through this, we were able to demonstrate internal quality factors as high as $Q_i \sim 10^5$ at $B_\parallel \simeq 6\,\text{T}$ and $B_\perp \simeq 20\,\text{mT}$. In addition to this, we demonstrated the importance of this technique for studies of mesoscopic devices in high magnetic fields by using the resonator to readout the charge state of double quantum dots that were electrostatically defined in InSb nanowires at $B_\parallel = 1\,\text{T}$.

Having successfully demonstrated a recipe for the reliable fabrication of low loss field resilient CPWs, these results broadly reduce the barriers for creating magnetic field compatible versions of commonly used superconducting circuits such as single photon detectors [1–3], parametric amplifiers [4, 5] or quantum memories [6–8]. They also serve as crucial circuit components in subsequent chapters, where they allowed us to use techniques more commonly used in superconducting circuits to sensitively probe mesoscopic physics of interest in strong magnetic fields.

In superconducting quantum computing (QC) CPW resonators are currently the only scaleable method to provide coherent connectivity between spatially separated qubits for high fidelity quantum gates and long distance quantum information transfer [9]. To transfer these techniques and achieve the same results in semiconducting [10–12] (see Fig. 8.1) and topological QC, the retention of high Qs in strong magnetic fields is paramount.

Chapter 5

Through the development of cleaner stack transfer techniques we were able to successfully demonstrate the first integration of a graphene JJ into a superconducting circuit to make a graphene based transmon. We were able to demonstrate device operation at $B_\parallel = 1\,\text{T}$, establishing the possibility of using cQED techniques to probe mesoscopic physics of interest in layered 2D materials at high magnetic fields.

A spate of recent results in van der Waals heterostructures have demonstrated how epitaxial control and clean interfaces can give rise to extraordinary unpredicted physics that to date is still not fully understood [13–15]. Integrating such materials into microwave frequency superconducting circuits could provide additional insight not accessible to DC transport techniques of the underlying physical processes, as well as studies of their time dynamics [16].
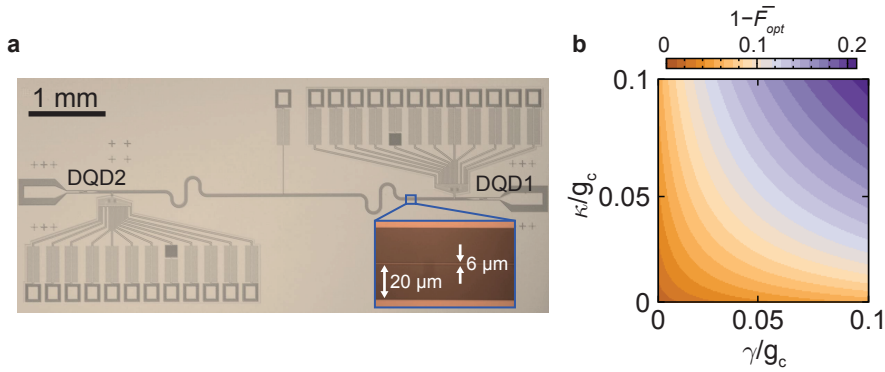
Figure 8.1: **a** Following the demonstration of strong coupling between a single spin and a photon, current work in semiconducting QC focusses on using a cavity to mediate long-range coherent coupling for high fidelity two-qubit gates and long range state transfer. Adapted from [10]. **b** Recent theoretical work reiterates the importance of retaining high Q_is in strong magnetic fields in order to minimise the infidelity of two-qubit gates. Adapted from [12].

Chapter 6

By strongly coupling an Al proximitised InAs nanowire to a high Q superconducting CPW cavity and voltage biasing the two condensates of the JJ to be a multiple of the fundamental cavity frequency ($2eV = hf_r$), we were able to demonstrate highly coherent microwave emission with coherence times in excess of 0.3 ms. As these coherence times significantly exceed the current coherence times of superconducting qubits, these devices could serve as low power, on chip coherent microwave sources, potentially replacing the bulky, expensive room temperature electronics currently being utilised in the efforts to produce a scaleable superconducting QC (SQC).

Future work should first focus on developing and testing control circuits that allow for rapid switching of the emission without affecting coherence. Similar devices using voltage biased double quantum dots as the photon emitters have demonstrated rapid switching of the emission and state readout of double quantum dots (Fig. 8.2a,b) [17, 18], although the coherence of devices based on DQDs appears to be a limiting factor for integration in current SQC experiments. In our experiments, the low temperature voltage biasing circuit should be modified to allow for rapid pulsing of the voltages on the JJ bias or the cutter (tuning E_J), with each investigated to determine which allows for the fastest switching of photon emission from the cavity without affecting the coherence. If neither can be shown to work satisfactorily, adding a secondary switching circuit in series with the lasing circuit (Fig. 8.2c) would work at the expense of additional circuit complexity, with rapid switching times of 6-8 ns already demonstrated [19].

In addition, as these devices use InAs-Al nanowires as their Josephson elements it may be possible to induce a topological state by applying a sufficiently strong magnetic field and tuning the chemical potential in the wire. The emergence of Majorana bound states (MBSs) at the edges of the topological state would result in
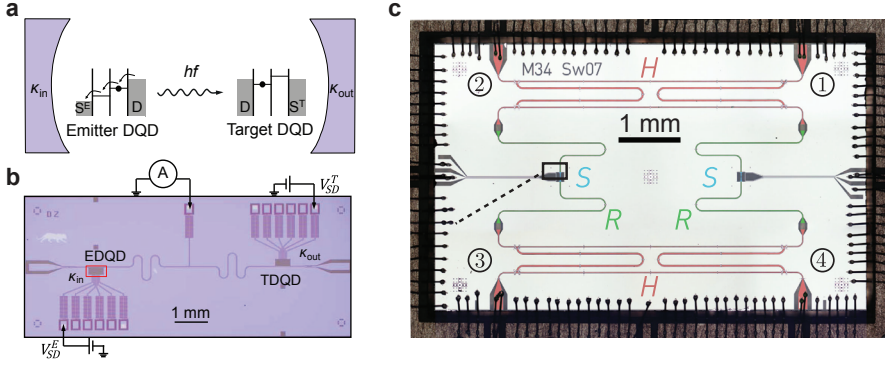
Figure 8.2: **a** Diagram of two DQDs embedded in a high Q cavity, with the emitter DQD used for state readout of the target DQD. **b** Optical microscope image of the device, with a voltage bias used to control the emission of the EDQD. Adapted from [18]. **b** A circuit formed from tuneable superconducting resonators and microwave beam splitters can produce rapid cryogenic switching, potentially allowing on-chip coherent microwave sources to be used for time-resolved qubit control and readout. Adapted from [19].

a topological Josephson effect with photon emission at half the frequency of the trivial state due to coherent tunnelling of single electrons [20, 21]. Examination of the photonic emission statistics in this device could then serve as additional evidence for the existence of MBSs. In order to accurately model and detect anomalous emission statistics from MBSs, it would be necessary to suppress the higher order tunnelling events that occur due to strong coupling between the junction and cavity [22], making the device an ineffective laser in the process.

Overcoming these experimental difficulties may even allow for signatures of more exotic topological Josephson effects to be measured, such as the fractional quantum Hall states with fractionally charged anyons such as the $e/3$ and $e/5$ states as their charge carriers [23].

Chapter 7

InAs-epi Al nanowires were integrated into transmon qubits that had been rendered field resilient using the techniques described in Chap. 4. By specifically designing them with a low E_J/E_C ratio, two-tone spectroscopy measurements as a function of gate charge n_g would reveal their level structure and charge dispersion, with unique spectroscopic features predicted to appear in a magnetic field due to coherent single electron tunnelling effects that would occur in the presence of MBSs in the wire.

The qubit coherence and Josephson coupling E_J were characterised as a function of parallel magnetic field $B_\parallel$, and found to survive up to $B_\parallel = 1\,\text{T}$, a magnetic field of sufficient strength to induce MBS signatures in nominally identical nanowires. Analysis of anomalous charge dispersions hint towards the suppression of Coulomb blockade by highly transmitting Andreev bound states in the JJ, although further investigation is required. No signatures of MBSs were observed,

although this could be due to a number of issues that will be addressed individually.

Material characteristics

The first issue relates to the inherent characteristics of InAs-epi Al nanowires. Although demonstration of qubit operation in $B_\parallel = 1\,\text{T}$ represents an order of magnitude improvement compared to previous results, this field sits at the lower end of where MBS signatures have been observed in this material system [24]. The lack of MBS signatures in our experiments does not therefore necessarily imply that our devices are not capable of hosting and measuring MBSs, but instead that we are not able to maintain device operation in the region where topological features occur.

One possible solution to this is to change materials systems to InSb semiconducting nanowires. Recent progress in material synthesis and growth techniques (see Fig. 8.3a,b) have produced high quality InSb nanowires with epitaxial Al shells on two facets, where adjacent wires are used as a shadow mask during evaporation to create SNS regions that can serve as JJs without etching [25], something that has been known to seriously damage the quality of the wires and suppress MBS signatures. These wires have produced the clearest signatures of MBSs to date [26], with the higher g factors significantly reducing the magnetic field range over which MBSs are observed into a region which our nanowire transmons can more comfortably operate in.

Optimised experimental throughput

The second issue relates to the difficulty of measuring devices with time consuming fabrication, inherently low yield and large parameter spaces. InAs and InSb nanowires grown via the VLS method are the favoured material platform, with their high mobilities and mature fabrication methodologies appearing to translate into the highest rate of MBS signatures. It appears that experimental topological physics is not yet an exact science however, as although yields of MBS signatures in devices can sometimes reach $\sim 10\%$ [26], extended periods of time can occur where no MBS signatures are measured. The exact cause of this is not clear, but variability of some unknown parameters during growth, fabrication or storage seem likely candidates. Until these parameters are identified by careful data logging and analysis, the only solution is to maximise the number of devices measured within a specific timeframe.

This can prove particularly problematic for cQED devices, as the lack of direct DC access to the wire for characterisation prevents many common diagnostics that would normally be used to quickly eliminate unpromising samples. Instead, only slow indirect measurements such as two-tone spectroscopy of the charge dispersion may be used to infer the presence of MBSs, making it take a prohibitively long time to search the large parameter spaces in field and gate of these devices using current techniques. One possible solution to this problem involves significant developments in both fabrication and measurement of devices.
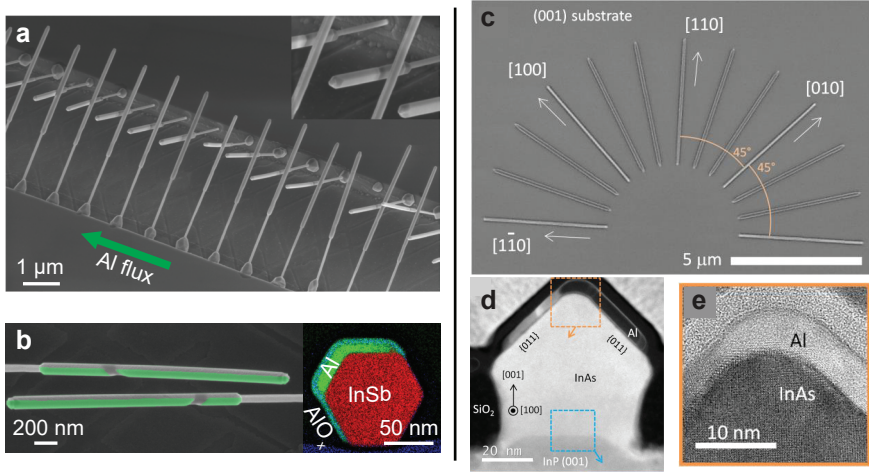
8

Figure 8.3: **a** A tilted SEM image of InSb wires grown via VLS in InP trenches. After wire growth, MBE creates a directional Al flux that causes an epitaxial Al layer to grow on two of the six facets. **b** The shadow of one wire onto another creates gaps in the epitaxial Al film (green) that allow for the creation of high quality SNS junctions without the need for etching of the Al shell. STEM/EDX images showing the Al growth on 2 facets, with the Al-InSb interface being free of AlO_x. Adapted from [25]. **c** InAs nanowires grown on an InP(001) substrate. The selective area growth allows for deterministic positioning of nanowires en masse, without deterministic placement. **d** STEM image a wire grown in the [100] direction. Subsequent MBE deposition of Al allows for an epitaxial Al layer on **e** two of the nanowire facets. Adapted from [27].

Optimised measurement techniques

A number of improvements to the measurement methodology can be taken to significantly increase the rate at which data can be taken, including but not limited to: optimised code for data transfer and analysis, equipment dedicated for fast broadband spectroscopy and fully automated measurement routines. The latter case in particular offers the possibility of greatest speed up, as to date we are principally limited by the manpower to properly characterise devices.

It should be noted that full automation of measurement routines is an incredibly challenging task, requiring input data that is consistent and easy to interpret. This is one case where cQED devices have an inherent advantage of their DC counterparts, as in contrast to most devices exhibiting topological signatures they are easily modelled by simple Hamiltonians with few free parameters, making it much easier for measurement routines to analyse the devices behaviour.

Device scaleability

Assuming that the measurement process can be significantly optimised to allow much faster (or even completely automated, parallel characterisation) the next bottleneck in this process flow is device fabrication. Although VLS nanowires are the most reliable system for MBS studies, their need for deterministic placement means that significant effort must be spent placing each wire and ensuring it is appropriately etched and contacted in subsequent steps. A scaleable solution for wire placement would significantly increase the rate of sample fabrication.

Recent work on selective area growth (SAG) shows promising results towards this, with high mobility InAs wires deterministically grown on InP substrates (see Fig. 8.3c) [27]. In-situ deposition allows for epitaxial layers of Al to be grown on the InAs nanowire facets (Fig. 8.3b,c), possibly even allowing the superconducting CPW resonators, transmon islands and couplers to be defined in the same step.

Taken together, these two improvements would greatly increase the rate at which devices could be fabricated and measurement, significantly increasing the likelihood of measuring signatures of topological states in cQED systems.

8

References

[1] Mazin, B. A., Day, P. K., LeDuc, H. G., Vayonakis, A. & Zmuidzinas, J. Superconducting kinetic inductance photon detectors. vol. 4849, 283 (International Society for Optics and Photonics, 2002).

[2] Day, P. K., LeDuc, H. G., Mazin, B. A., Vayonakis, A. & Zmuidzinas, J. A broadband superconducting detector suitable for use in large arrays. *Nature* **425**, 817–821 (2003).

[3] Vardulakis, G., Withington, S., Goldie, D. J. & Glowacka, D. M. Superconducting kinetic inductance detectors for astrophysics. *Measurement Science and Technology* **19**, 015509 (2008).

[4] Castellanos-Beltran, M. A. & Lehnert, K. W. Widely tunable parametric amplifier based on a superconducting quantum interference device array resonator. *Applied Physics Letters* **91**, 083509 (2007).

[5] Tholén, E. A. *et al.* Nonlinearities and parametric amplification in superconducting coplanar waveguide resonators. *Applied Physics Letters* **90**, 253509 (2007).

[6] Kubo, Y. *et al.* Strong coupling of a spin ensemble to a superconducting resonator. *Physical Review Letters* **105**, 140502 (2010).

[7] Amsüss, R. *et al.* Cavity QED with magnetically coupled collective spin states. *Physical Review Letters* **107**, 060502 (2011).

[8] Ranjan, V. *et al.* Probing dynamics of an electron-spin ensemble via a superconducting resonator. *Physical Review Letters* **110**, 067004 (2013).

[9] Dicarlo, L. *et al.* Demonstration of two-qubit algorithms with a superconducting quantum processor. *Nature* **460** (2009).

[10] Mi, X. *et al.* A coherent spin-photon interface in silicon. *Nature* **555**, 599–603 (2018).

[11] Harvey, S. P. *et al.* Coupling two spin qubits with a high-impedance resonator. *Physical Review B* **97**, 235409 (2018).

[12] Benito, M., Petta, J. R. & Burkard, G. Optimized cavity-mediated dispersive two-qubit gates between spin qubits (2019). `arXiv:1902.07649`.

[13] Cao, Y. *et al.* Correlated insulator behaviour at half-filling in magic-angle graphene superlattices. *Nature* **556**, 80–84 (2018).

[14] Cao, Y. *et al.* Unconventional superconductivity in magic-angle graphene superlattices. *Nature* **556**, 43–50 (2018).

[15] Fatemi, V. *et al.* Electrically tunable low-density superconductivity in a monolayer topological insulator. *Science* **362**, 926–929 (2018).

8

[16] Hays, M. *et al.* Direct Microwave Measurement of Andreev-Bound-State Dynamics in a Semiconductor-Nanowire Josephson Junction. *Physical Review Letters* **121**, 047001 (2018).

[17] Liu, Y.-Y. *et al.* Threshold Dynamics of a Semiconductor Single Atom Maser. *Physical Review Letters* **119**, 097702 (2017).

[18] Liu, Y.-Y. *et al.* On-Chip Quantum-Dot Light Source for Quantum-Device Read-out. *Physical Review Applied* **9**, 014030 (2018).

[19] Pechal, M. *et al.* Superconducting Switch for Fast On-Chip Routing of Quantum Microwave Fields. *Physical Review Applied* **6**, 024009 (2016).

[20] Fu, L. & Kane, C. L. Josephson current and noise at a superconductor-quantum-spin-Hall-insulator-superconductor junction. *Physical Review B* **79**, 161408 (2009).

[21] Badiane, D. M., Glazman, L. I., Houzet, M. & Meyer, J. S. Ac Josephson effect in topological Josephson junctions. *Comptes Rendus Physique* **14**, 840–856 (2013).

[22] Hofheinz, M. *et al.* Bright Side of the Coulomb Blockade. *Physical Review Letters* **106**, 217005 (2011).

[23] Kapfer, M. *et al.* A Josephson relation for fractionally charged anyons. Tech. Rep. (2019).

[24] Deng, M. T. *et al.* Majorana bound state in a coupled quantum-dot hybrid-nanowire system. *Science* **354**, 1557–1562 (2016).

[25] Gazibegovic, S. *et al.* Epitaxy of advanced nanowire quantum devices. *Nature* **548**, 434–438 (2017).

[26] Zhang, H. *et al.* Quantized Majorana conductance. *Nature* **556**, 74–79 (2018).

[27] Lee, J. S. *et al.* Selective-area chemical beam epitaxy of in-plane InAs one-dimensional channels grown on InP(001), InP(111)B, and InP(110) surfaces (2018). `arXiv:1808.04563`.

8

Acknowledgements

After graduating and taking some time to reflect on my life and what I wanted to achieve I became sure of two things: firstly, that I would leave the United Kingdom to live abroad, at least for a few years, and secondly that would I undertake a PhD working on fundamental physics that ostensibly lead to practical applications. After interviewing in several institutions without finding a good fit, I received an invitation to visit Delft to talk to Leo and his group. I instantly fell in love with the place, not only because of the impressive work and amazing facilities, but the motivated, fun, international atmosphere of the people here. I have had the pleasure of seeing QuTech grow since its inception, and I feel confident in saying there is probably nowhere I would have preferred to do my PhD. Although it has been hard at times, it has certainly been the most rewarding experience of my life.

I have to thank you, **Leo**, for giving me this opportunity. Your ambition, scientific skill and ability to create a productive yet open work environment have been an inspiration to me. **Maja**, thank you believing in me, teaching me the value of hard work, and how to *be* the honey badger, I hope you and your family are happy in Sydney and I hope to see you again soon. **Srijit**, I learned so much from you, and I have to thank you for your support in getting my first paper published. Congratulations on starting your own group, I am sure you will achieve much, giving us another excuse to celebrate together! **Angela**, it has been a pleasure to work with you for the remainder of my PhD, thank you for supporting me where you can, I can see that the future of cQED in the Topo team is in good hands. **Gijs**, thank you for all of your advice and help over the years, as well as the good conversations! I'll say it, you were right!

Willemijn, we went through it all together, the good times and the bad times. Working with you was very enjoyable, and I am happy to now count you as a close friend. And remember, no high fives! To my former students, **Damaz**, **Francesco**, **Kian**, the student teacher relationship is, like any other, a two way street. I think you would be surprised at how much I learned from each of you as we worked together and I got to know you all. It makes me happy to know that you will all go on to achieve much.

To the old guard: **Önder**, **Daniel**, **Vincent**, **Kun**, **Jakob**, **David**, **Arjan**, thanks for teaching me about the intricacies of academic life, looking out for me at the start and helping me survive my first couple of years. To my comrades in arms: **Fokko**, **Jasper**, **Nikolai**, **Amrita**, **Sebastian**, **Jie**, **Attila** thank you for making Topo such an easy and enjoyable team to work in. To the new guard: **Arno**, **Vukan**, **Marta**, **Lin**, **Christian**, **Ting**, **Qing**, **Daniel**, **Luca**, **Guan**, **Vanessa**, **Di** and **Jaap**, good luck with the rest of your PhDs, I hope you had as much fun and grow as much as I did.

In addition to the academic side, we are now lucky enough to have a corporate side provided by our good friends at Microsoft. Without the help and support from

Delft (**Marina**, **Kevin**, **Ivana**, **John**, **Bernard**, **CK**, **Simone**), Copenhagen (**Charlie**, **Karl**, **Lucas**, **Robert**, **Thorvald**, **Anders**) and Sydney (**David**, **John**) I could never have learned and achieved as much as I have.

A research group focussed principally on transport is nothing without its material growers, so I would like to thank **Erik** and **Sebastian** from Eindhoven, **Peter** and **Jesper** from Copenhagen and **Kenji** and **Takashi** from NIMS, Tsukuba.

With my PhD thesis sitting at the interface between two different fields, I benefited tremendously from interactions with the lab of Leo DiCarlo. **Leo**, I am sad that we were never able to work together, but I appreciate all the support you and your team gave me. One of the highlights of my PhD will always be playing AC/DC with you on stage! **Chris**, you started only shortly before me but I always looked up to you, not only as a scientist but as friend to learn from. I hope we stay in touch now that you are in Cologne. **Ramiro**, I still remember the first day you came when I asked you to join me for lunch. I have had a great time living with you, your positive energy is something I hope to emulate one day. **Florian**, we really should have worked together! Thanks for helping me so much in my PhD, and I wish you the best of luck in Portland. **Ale**, I love that you embrace the role of the mad scientist with glee, and better yet you make it work! Good luck to you and your new family. **Nathan**, thanks for teaching me so much about cQED when I was a young, slightly lost PhD student. **Adriaan**, and **Neils**, good luck with your start up adventures. **Nandini**, good luck with the rest of your research, I hope you get everything you wish for!

It says a lot about QuTech that my acknowledgements list is already so long while mentioning only a fraction of the roadmaps! **Anaïs**, **Suzanne**, **Max**, **Arian**, **Jelmer**, **Udi**, **Toivo**, **Anne-Marije**, **Will**, **Victoria**, **Filip**, **Kenneth**, thanks for making QuTech such an enjoyable experience, at work and and at play! **Jonas**, the QuTech blog was a hugely enjoyable experience. Thanks for taking the initiative to start it, and for all the pointless arguments we seem to enjoy so much.

As QuTech has grown, so has the number of support staff without which the entire operation would grind to a halt. **Marja**, **Yuki**, **Jenny**, **Chantal** thanks for helping me keep on top of all the administrative duties that we scientists seem to be so terrible at. No student could achieve as much as they do without the support of the technicians. **Jason**, **Olaf**, **Matt**, **Mark**, **Jelle**, **Remco**, **Nico**, **Siebe** thanks for keeping everything ticking, and putting in the extra mile to help us when we needed you. **Raymond**, **Raymond** and **Marijn**, it is a certainty that QuTech would not be what it is without your ever kind and helpful support, even when we come to you with stupid questions. Always vigilant, we all have a lot to thank for when it comes to the tireless work of the **Kavli nanolab** staff. Similarly the experiments we do would simply not be possible without the help of **DEMO**.

Of course, how could I forget the four musketeers? **Norbert**, you were a joy to live with and I learned so much from you, not only about science but also life. Good luck in Zurich and I'll see you soon. **Michiel**, thank you for never letting your encyclopaedic knowledge turn into a source of frustration for me. We were there for each other in the good times and the bad, and I'll always remember that. **Alex**, we started on the same day and have had so many adventures together. I hope

they, and an over-reliance on Proutski-logic, will continue in years to come. **Peter**, although our time together was short I value our friendship enough to consider you an honorary musketeer! Good luck in London and I will see you there.

I have been fortunate enough in my years here to meet so many interesting, kind people. **Mano**, it will be a sad day if you ever leave the Netherlands, but until that day I will always value our time spent together. **Maartje**, your positive energy and love of animals will always be as inspiration to me. To many more drunken evenings together! **Terri**, although technically I knew you previously I can now count you as one of my Dutch friends. I hope to spend more time with you and Dani now that I no longer have a thesis to write. **Marie-Claire**, I call you this purely to annoy you. You are a meme-queen of the highest degree, and I thank you for being such a good friend on the other side of the world, I look forward to seeing you again.

To some of you I have grown so close that I would consider you a second family. **Nodar**, you are my quasi-brother, and it is my pleasure to see you grow as a person, just as I have. I know I can always rely on you. **Stefan**, you are wise in this world, and I will always value your conversation and advice. I hope you can make your way back here one day. But remember, we'll always have Scotland. **Beatrice**, you are one of my oldest friends in the Netherlands and I have learned so much from you. One day I hope to find your source of infinite energy and steal some for myself. **Vidak** please never stop being weird. I am glad you are staying with us, and I look forward to hearing your music more and more! **Jouri**, after getting to know each other in San Sebastian we have been able to enjoy so many great experiences together. Let's keep them coming! **Markus** und **Diana** thank you for always making me feel at home with you. I look forward to your wedding and seeing you again in Munich!

I could not be where I am today without the unwavering support of **my family**. Although I try to be fiercely independent, I have always benefited from knowing that you will be there for me, whenever I need you.

And finally, **Deniz**, my guiding light. Love can come from the most unsuspecting places, and since we met I have enjoyed every second of our adventure. We seem to know each other better than we know ourselves, and I hope we can continue to grow together. I can't wait to see where our adventure takes us next. Aşkım seni seviyorum.

8

Curriculum Vitæ

James Grant Kroll

12-02-1990   Born in Reading, England.

Education

2002–2008   High School
             Portree High School, Scotland

2008–2013   Integrated Masters in Physics
             University of Edinburgh, Scotland
             Thesis: High Pressure X-Ray Diffraction of MgV_2O_4
             Promotor: Prof. M. McMahon

2014–2019   PhD. Physics
             Delft University of Technology, The Netherlands
             Thesis: Magnetic field compatible hybrid circuit quantum
                            electrodynamics
             Promotor: Prof. dr. ir. L. P. Kouwenhoven

List of Publications

3. M.C. Cassidy, W. Uilhoorn, **J.G. Kroll**, D. de Jong, D.J. van Woerkom, J. Nygård, P. Krogstrup, L.P. Kouwenhoven, *A semiconductor nanowire Josephson laser*, in preparation.

2. **J. G. Kroll**, F. Borsoi, K. L. van der Enden, W. Uilhoorn, D. de Jong, M. Quintero-Peréz, D. J. van Woerkom, A. Bruno, S. R. Plissard, D. Car, E. P. A. M. Bakkers, M. C. Cassidy, L. P. Kouwenhoven, *Magnetic field resilient superconducting coplanar waveguide resonators for hybrid cQED experiments* arXiv:1809.03932, accepted for publication in Physical Review Applied.

1. **J. G. Kroll**, W. Uilhoorn, K.L. van der Enden, D. de Jong, K. Watanabe, T. Taniguchi, S. Goswami, M.C. Cassidy, L.P. Kouwenhoven, *Magnetic field compatible circuit quantum electrodynamics with graphene Josephson junctions.* Nature Communications **9** 4615 (2018).